The hydrodynamics of rowing propulsion

An experimental study

Grift, E.J.

DOI
10.4233/uuid:defe4405-a1c1-4e18-af48-7a93fcd55152

Publication date
2020

Document Version
Final published version

Citation (APA)
Grift, E. J. (2020). *The hydrodynamics of rowing propulsion: An experimental study*. [Dissertation (TU Delft), Delft University of Technology]. https://doi.org/10.4233/uuid:defe4405-a1c1-4e18-af48-7a93fcd55152

Important note
To cite this publication, please use the final published version (if applicable).
Please check the document version above.

THE HYDRODYNAMICS OF ROWING PROPULSION

AN EXPERIMENTAL STUDY

THE HYDRODYNAMICS OF ROWING PROPULSION

AN EXPERIMENTAL STUDY

Proefschrift

ter verkrijging van de graad van doctor
aan de Technische Universiteit Delft,
op gezag van de Rector Magnificus prof.dr.ir. T.H.J.J. van der Hagen,
voorzitter van het College voor Promoties,
in het openbaar te verdedigen op
donderdag 24 september 2020 om 15:00 uur

door

Ernst Jan GRIFT

Werktuigbouwkundig Ingenieur,
Universiteit Twente, Nederland
geboren te Amersfoort, Nederland.

Dit proefschrift is goedgekeurd door de promotoren.

Samenstelling promotiecommissie bestaat uit:

Rector Magnificus	voorzitter
Prof.dr.ir. J. Westerweel	Technische Universiteit Delft, promotor
Dr.ir. M.J. Tummers	Technische Universiteit Delft, copromotor
Onafhankelijke leden:	
Prof. C. Clanet	Ecole Polytechnique, France
Dr. M.J. Hofmijster	Vrije Universteit Amsterdam/ Hogeschool van Amsterdam
Prof.dr.ir H.J.H. Clercx	Technische Universiteit Eindhoven
Prof.dr. F. Scarano	Technische Universiteit Delft
Prof.dr.ir. H.W.M. Hoeijmakers	Universiteit Twente
Prof.dr.ir. C. Poelma	Technische Universiteit Delft, reservelid

Dit onderzoek is deel van het onderzoeksprogramma 'Optimalisatie van voortstuwing door en over water' met projectnummer 12868, en is (deels) gefinancierd door de Nederlandse Organisatie voor Wetenschappelijk Onderzoek (NWO).

Cover: Snapshot of the vorticity field around an oar blade (Chapter 3)

Printed by: Ridderprint - Alblasserdam

ISBN 978-94-6416-068-0

An electronic version of this dissertation is available at
http://repository.tudelft.nl/.

CONTENTS

SUMMARY

The aim of this thesis is to analyse the hydrodynamics of rowing propulsion and to enhance this propulsion. This requires to have insight in both the flow phenomena and the generated hydrodynamic forces. In (competitive) rowing athletes generate a propulsive force by means of a rowing oar blade. During propulsion the oar blade is submerged close to the surface and the athlete exerts a force on the handle of the oar. This causes a reaction force from the water at the other end of the oar, the oar blade, which together with the force at the handle generates the propulsive force at the oar lock, the pivot point on the boat. For optimal performance it is essential to maximise the propulsion caused by this hydrodynamic reaction force at the blade. To achieve this, understanding of the flow field around the oar blade during this propulsive phase is vital.

In chapter 2 the results are presented on the drag on, and the flow field around, a submerged rectangular normal flat plate, which is uniformly accelerated to a constant target velocity along a straight path. The plate aspect ratio is chosen to be AR = 2 to resemble an oar blade in (competitive) rowing. The plate depth, i.e. the distance from the top of the plate to the air–water interface, the plate acceleration and the plate target velocity are varied, resulting in a plate width based Reynolds number of $4\times10^4 \leq Re \leq 8\times10^4$. In the analysis three phases are distinguished; (i) the acceleration phase during which the plate drag is increased, (ii) the transition phase during which the plate drag decreases to a constant steady value upon which (iii) the steady phase is reached. The plate drag force is measured as function of time which showed that the steady-phase plate drag at a depth of 1/5 plate height (20 mm depth for a plate height of 100 mm) increased by 45% compared to the plate top at the surface (0mm). Also, it is shown that the drag force during acceleration of the plate increases over time and is not captured by a single added mass coefficient for prolonged accelerations. Instead, an entrainment rate is defined that captures this behaviour. The formation of starting vortices and the wake development during the time of acceleration and transition towards a steady wake are studied using hydrogen bubble flow visualisations and particle image velocimetry. The formation time, as proposed by Gharib et al. (J. Fluid Mech., vol. 360, 1998, pp. 121–140), appears to be a universal time scale for the vortex formation during the transition phase. These findings serve as the basis for defining a best practice during the start of a rowing race as described in chapter 4.

In chapter 3 the results are presented of experiments in which the flow around a realistic rowing oar blade, in combination with realistic kinematics, was measured using concurrent force measurements and PIV measurements. The aim of these experiments is to identify which flow phenomena govern rowing propulsion and subsequently adjust the oar blade configuration to optimise rowing propulsion. The oar blade moves along a cycloidal path, and due to the large accelerations and decelerations replicating the oar blade path is all but trivial. The oar blade and kinematics are scaled by a factor of 0.5 due to limitations of the experimental set-up. The flow field around the oar blade during the drive phase is measured and several flow phenomena such as the generation of

leading and trailing edge vortices are linked to the generation of lift and drag, which both contribute to rowing propulsion. The oar blade performance is defined as the energetic and impulse efficiencies η_E and η_J, where the latter can be seen as the alignment of the generated impulse with the propulsive direction. It is found that when using a standard configuration of a rowing oar blade, the generated impulse is not aligned with the propulsive direction. This suggests that the propulsion is not optimal. By adjusting the angle at which the blade is attached to the oar an optimal oar blade angle was found ($\beta = 15°$) that aligns the generated impulse with the propulsive direction. At this angle the generation of leading and trailing edge vortices changes such that the overall hydrodynamic efficiency of the propulsion is optimised.

SAMENVATTING

Het doel van deze thesis is om de hydrodynamica van de voortstuwing in het roeien te analyseren en om de voortstuwing te verbeteren. Hiervoor is inzicht in zowel de stromingsverschijnselen als in de gegenereerde hydrodynamische krachten nodig. In (wedstrijd) roeien genereren atleten een voortstuwende kracht door middel van een roeiblad. Tijdens de voortstuwing is het blad dicht bij het oppervlak ondergedompeld en oefent de atleet een kracht uit op het handvat van de riem. Dit wekt een reactiekracht van het water op aan het andere uiteinde van de roeiriem, die tezamen met de kracht op het handvat een voortstuwende kracht op de dol (het draaipunt van de riem dat vastzit aan de boot) genereert. Voor een optimale prestatie is het van belang dat de voortstuwing veroorzaakt door de hydrodynamische reactiekracht op het blad wordt gemaximaliseerd. Om dit te bereiken is het essentieel het stromingsveld rond het roeiblad tijdens de voortstuwende fase te begrijpen. In hoofdstuk 2 worden de resultaten gepresenteerd met betrekking tot de weerstand op, en de stroming rond, een ondergedompelde rechthoekige plaat haaks op de stroming, die constant versneld naar een constante doelsnelheid langs een gestrekt pad. De vormverhouding van de plaat is gekozen op AR = 2, gelijkend de vormverhouding van een roeiblad in het (wedstrijd) roeien. De plaatdiepte, dat is de afstand van de bovenkant van de plaat tot de lucht-water overgang, de plaat versnelling en de plaat doelsnelheid worden gevarieerd wat resulteert in een plaat-breedte gebaseerd Reynolds getal van $4\times10^4 \leq Re \leq 8\times10^4$. In de analyse wordt onderscheid gemaakt in drie fases; (i) de versnelde fase tijdens welke de plaatweerstand verhoogd is, (ii) de transitiefase waarin de plaatweerstand afneemt tot een constante vaste waarde, waarna (iii) de constante fase is bereikt. The plaatweerstand wordt gemeten als functie van tijd en laat zien dat de plaatweerstand tijdens de constante fase 45% hoger is bij een plaatdiepte van 1/5 plaathoogte (20 mm diepte bij een plaathoogte van 100 mm) vergeleken bij een plaatdiepte waarbij de bovenkant van de plaat het wateroppervlakte raakt (0 mm). Ook is aangetoond dat de weerstand tijdens het versnellen van de plaat toeneemt in de tijd en in het geval van langere versnellingen niet kan worden uitgegaan van een enkele coëfficient om de toegevoegde massa te beschrijven. In plaats daarvan is een meesleep snelheid gedefinieerd dat dit gedrag wel goed beschrijft. De formatie van startwervels en de ontwikkeling van het zog tijdens de versnelde fase en de transitiefase zijn bestudeerd door middel van waterstofbellenvisualisatie en deeltjes beeld velocimetrie (PIV). De formatietijd, zoals voorgesteld door Gharib et al. (J. FluidMech., vol. 360, 1998, pp. 121–140), blijkt een universele tijdschaal voor wervelformatie tijdens de transitiefase. Deze bevindingen vormen de basis voor de gedefinieerde *best practice* om een race te starten, zoals is beschreven in hoofdstuk 4. In hoofdstuk 3 worden de resultaten gepresenteerd van experimenten waar de stroming rond een realistisch roeiblad in combinatie met realistische kinematica gelijktijdig is bepaald door middel van gelijktijdige krachtmetingen en PIV metingen. Het doel van deze experimenten is om te bepalen welke stromingsverschijnselen de voortstuwing in het roeien bepalen en daarnaast hoe het roeiblad moet worden aangepast voor

een optimale voortstuwing. Het roeiblad beweegt langs een cycloïde-achtig pad en door de hoge versnellingen en vertragingen is het nabootsen van het bladpad alles behalve triviaal. Zowel de kinematica als de geometrie van het bladpad worden geschaald met een factor 0.5 om tegemoet te komen aan de beperkingen van de experimentele opstelling. De stroming rond het bladpad wordt tijdens de voortstuwende fase gemeten en verschillende stromingsverschijnselen, zoals gegenereerde wervels aan de randen van het roeiblad, kunnen worden gekoppeld aan het ontstaan van lift en weerstand, die beide bijdragen aan de voortstuwing in het roeien. Het prestatievermogen van het roeiblad is gedefinieerd als een energetische en stoot efficiëntie η_E en η_J, waar de laatste kan worden gezien als de uitlijning van de gegenereerde stoot met de voortstuwingrichting. Er is aangetoond dat wanneer de standaard configuratie van een roeiblad wordt gebruikt, de gegenereerde stoot niet in lijn is met de voortstuwingsrichting. Dit suggereert dat de voortstuwing niet optimaal is. Door de hoek waarmee het roeiblad aan de steel vastzit aan te passen is een optimale bladhoek gevonden ($\beta = 15°$) die de gegenereerde stoot uitlijnt met de voortstuwingsrichting. Onder deze hoek wordt de generatie van wervels aan de randen van het roeiblad zo beïnvloed dat de algehele hydrodynamische efficiëntie van de voortstuwing wordt geoptimaliseerd.

1

INTRODUCTION

In this chapter a general introduction is given on the hydrodynamics of rowing. The rowing motion is explained and specific attention is paid to the oar blade path. Based on the oar blade kinematics several force decompositions such as lift and drag are defined. The effectiveness and efficiency of rowing propulsion are defined to quantify the performance of rowing propulsion. Finally, previous work, the challenges that arise in investigating the hydrodynamics of rowing, and the objectives of this research are presented.

Parts of this introduction are taken from chapter 2 and 3 to provide a cohesive general introduction to the work in this thesis. More detailed background information specific to each chapter is found in the chapters itself.

1

1.1. INTRODUCTION

The aim of this thesis is to analyse the hydrodynamics of rowing propulsion and to enhance this propulsion. This requires to have insight in both the flow phenomena and the generated hydrodynamic forces. In (competitive) rowing athletes generate a propulsive force by means of a rowing oar blade. During propulsion the oar blade is submerged close to the surface and the athlete exerts a force on the handle of the oar. This causes a reaction force from the water at the other end of the oar, the oar blade, which together with the force at the handle generates the propulsive force at the oar lock, the pivot point on the boat. For optimal performance it is essential to maximise the propulsion caused by this hydrodynamic reaction force at the blade. To achieve this, understanding of the flow field around the oar blade during this propulsive phase is vital. In figure 1.1 a full stroke cycle is shown, with the camera (drone) following the boat. The moment in time when the athlete submerges the oar blade in the water is called the *catch*, and marks the start of the *drive phase* during which the blade is submerged and the boat is propelled. The athlete ends the drive phase by extracting the blade from the water which is called the *release*, after which the athlete repositions himself during the *recovery phase* to start a new cycle of catch, drive, release, and recovery. In the figure a Men's coxless pair is shown, which uses one oar on each side of the boat. In other boat types multiple oars can be present at each side of the boat, e.g. in a men's eight four oars are used on each side. Note that oar blades enter the water where the water is not perturbed by previous strokes, i.e. during the recovery phase the boat has travelled a large enough distance, so that the boat has passed the water perturbed by the previous stroke(s).

The insights in the relation between acceleration and the generated forces presented this thesis are not only of interest for rowing propulsion, but can also be of interest for general objects in accelerating or decelerating motion or objects subject to accelerating or decelerating flow, either translational and/or rotational; examples are insect wings (flapping flight), wind turbines, drone flight, coastal structures, etc.

1.2. OAR BLADE KINEMATICS AND DEFINITION OF FORCES

Although it appears that a rowing oar blade moves along a circular path during the drive phase, its motion is all but trivial. The circular path is only observed when moving with the boat. When observed from an earth-bound reference frame, see figure 1.2, the oar blade moves along a complex cycloid path and is subject to large accelerations and decelerations [3]. This makes the flow around an oar blade highly dynamic and complex with the presence of a free surface possibly further complicating the flow dynamics. The oar blade motion during the drive phase is confined to a relatively small area of approximately 0.8 m × 0.8 m, see chapter 3 for a more detailed analysis. As a result of this, concurrent strokes, i.e. strokes made by different athletes at the same time, do not directly affect one another. Also, the motion of the oar blade during the propulsive phase is solely in the horizontal x,y-plane. Since the athletes do not exert any significant force perpendicular to that, i.e. in vertical z-direction, it is assumed that these forces can be neglected and therefore all force analyses are performed in the x,y-plane omitting forces in z-direction.

(i) The catch, where the athlete submerges the oar blade.

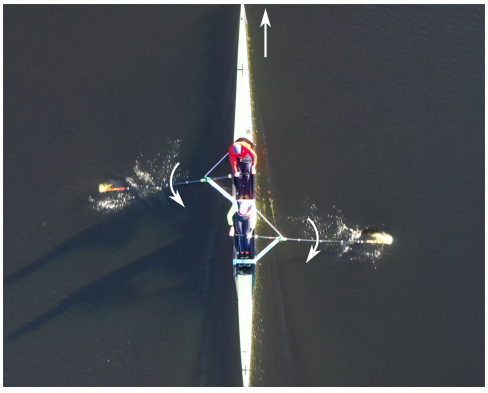

(ii) The drive phase, during which the oar blade is submerged and the boat is propelled.

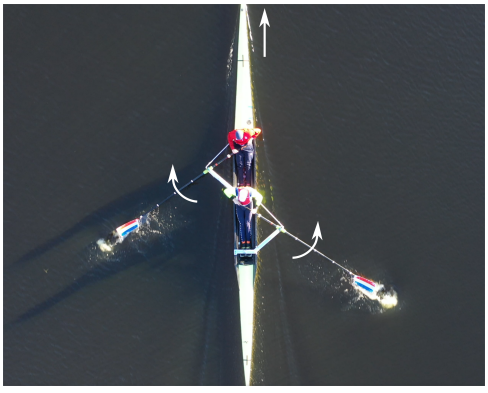

(iii) The release, where the athlete extracts the oar blade from the water.

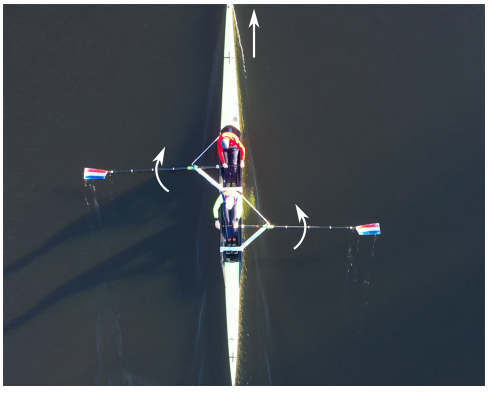

(iv) The recovery phase, during which the athlete repositions himself for the next catch.

Figure 1.1: The stroke cycle of a Men's coxless pair during the four different elements of the stroke (i) the catch, (ii) the drive phase, (iii) the release, and (iv) the recovery phase. The direction of travel of the boat is towards the top of the figure. The direction of the rotation of the oars is indicated by the curved arrows.

t = 0.00 s (catch) t = 0.15 s t = 0.32 s t = 0.48 s t = 0.64 s t = 0.81 s (release)

Figure 1.2: The path of the oar blade tip (solid blue line) during the drive of a men's coxless four (M4-) from catch to release at equidistant times. Images were acquired by filming from a bridge downward from a fixed position perpendicular to the water surface. Identical to figure 3.3

1.2.1. DEFINITION OF FORCES

Since along the oar blade path the oar blade motion is partly perpendicular to the direction of the boat motion, while apparently generating propulsion during the entire drive phase, it appears that both lift and drag contribute to propulsion in rowing; as is confirmed in chapter 3. The highly dynamic motion of the oar blade, includes acceleration, deceleration, both translating and rotating motion, and even motion leading to flow reversal. Consequently, the forces acting on the oar blade continuously vary in magnitude and direction. The 'ordinary' definition of lift and drag, i.e. perpendicular and opposed to the incoming flow, respectively, does not hold without selecting a single point on the oar blade such that a reference velocity is defined[1]. In figure 1.3 the definition of the reference point (the blade tip) and the definition of the various force decompositions is shown, which proof useful in analysing the hydrodynamics; see chapter 3. The normal and tangential force components F_n and F_t acting on the blade are measured using a force transducer. The force transducer is mounted between the robot head and the strut that holds the blade. The strut holds the blade at the same point as that the oar shaft holds the blade during actual on-water rowing.

The direction of the boat motion is defined as the positive x-direction such that force component F_x is the propulsive force. The force components F_x and F_y are bound to the frame of reference x,y, the normal and tangential force components F_n and F_t are bound to the oar blade, and the lift and drag force components F_L and F_D are based on the apparent velocity at the reference point, i.e. the blade tip. From the measured components F_n and F_t and the oar angle θ and angle of attack α it can be derived that:

$$\begin{aligned} F_x &= F_n\cos\theta - F_t\sin\theta \quad \text{and} \quad F_y = F_n\sin\theta + F_t\cos\theta \\ F_L &= F_n\cos\alpha - F_t\sin\alpha \quad \text{and} \quad F_n\sin\alpha + F_t\cos\alpha, \end{aligned} \tag{1.1}$$

The lift force component F_L and the drag force component F_D are, for (quasi-) steady

[1] Note that for the complex motion of the oar blade the definition of the lift and drag is based on the instantaneous motion of the oar blade, i.e. as if moving through stagnant water not taking into account the flow history.

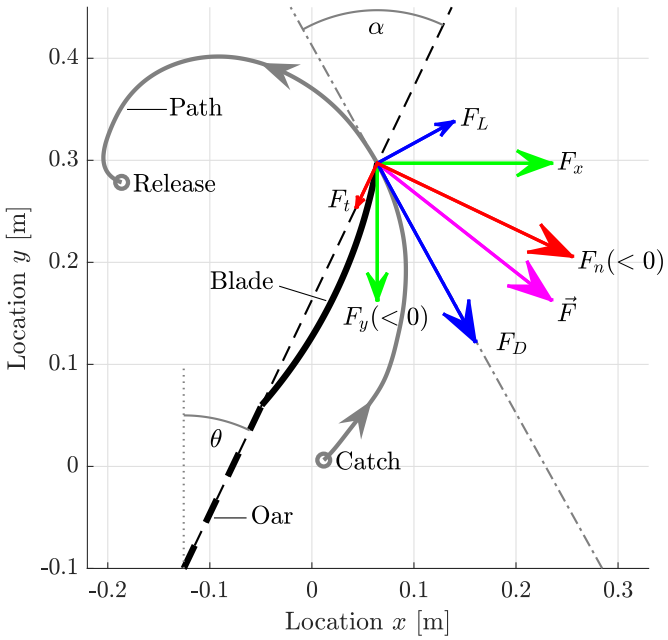

Figure 1.3: The blade (solid black line) moving along the path (solid grey line) from 'catch' towards the 'release' in the direction illustrated by the tangential line (dash-dotted grey) at an angle of attack α, i.e. the angle between the path tangent and the oar blade that is at an orientation θ. The measured force on the oar blade $\vec{F}$ (magenta) consists of a component tangential to the blade F_t and normal to the blade F_n (red). The measured force can also be decomposed in a propulsive component F_x and a non-propulsive component F_y perpendicular to that (green) that are defined parallel to the x-direction and y-direction, respectively. Alternatively, we can decompose the measured force in a lift component F_L and drag component F_D (blue), defined perpendicular and opposed to the direction of motion, respectively. The annotation '(< 0)' indicates that the respective vector component opposes the direction that is defined as positive. Figure identical to figure 3.2

flow, generally defined as:

$$F_D = \frac{1}{2}\rho|V|^2 C_D A \qquad \text{and} \qquad F_L = \frac{1}{2}\rho|V|^2 C_L A, \tag{1.2}$$

where ρ is the fluid density, $|V|$ is the velocity magnitude of the incoming flow, A is some representative surface of the object, and C_D and C_L are the drag and lift coefficients, respectively. The drag and lift coefficients describe the effect of the geometry of the object on the force generated by the flow. Under steady conditions the drag coefficient C_D can be considered constant for large enough Reynolds numbers, or for geometries with a well-defined separation point, as discussed by e.g. Williamson [17]. Both the lift and drag coefficients vary with the angle of attack, i.e. the angle at which the flow approaches the object, where the lift coefficient C_L increases with increasing angle of attack until it decreases again due to the occurrence of *stall* [1]. For an object accelerating in the flow the force on the object is larger then at constant velocity due to added mass which depends on the velocity profile. In chapter 2 we show that the increase in force due to added mass is dependent on both the acceleration and the duration of the acceleration, see Grift *et al.* [9]. In chapter 3 it was found that due to the combination of translational and rotational motion of the oar blade a large leading edge vortex (LEV) is created that remains attached to the oar blade which increases the generated force; a mechanism also described by e.g. Eldredge & Jones [8].

1.2.2. DEFINITION OF PERFORMANCE

Due to the complex oar blade path the resultant force $\vec{F}$ continuously varies in direction and magnitude. Therefore conventional approaches, e.g. optimising C_L/C_D, are less useful to determine the hydrodynamic performance. Instead, a generalisation is made using the impulse $\vec{J}$ generated during the drive phase of a single stroke. To assess the performance of a rowing motion two aspects are considered: *effectiveness* and *efficiency*. The athlete's aim of performing the rowing motion is to generate propulsion. The total propulsion that is generated during a single drive is the total change in momentum in x-direction, i.e. the impulse $\vec{J}$, defined as:

$$\vec{J} = \int_{t_{catch}}^{t_{release}} \vec{F}(t)\mathrm{d}t, \tag{1.3}$$

where t_{catch} and $t_{release}$ are the moments in time when the oar blade enters (catch) and leaves the water (release), respectively, and $\vec{F}$ is the force vector decomposed in a propulsive component F_x and a non-propulsive component F_y. We define the effectiveness of the drive phase as J_x, i.e. the component of the impulse in x-direction. Thus, the more impulse in x-direction is generated, the more *effective* the drive is, regardless of the amount of energy that is required for this.

The 'cost' of generating propulsion for athletes is the total energy spent, i.e. work performed, during the drive phase, as is reported by e.g. Hofmijster *et al.* [10]. Since athletes have a limit to the amount of work they can perform, it is interesting to define an efficiency in terms of propulsion per unit energy. Since both the kinematics of the oar blade (translation $\vec{V}$ and rotation $\vec{\omega}$) as well as the hydrodynamic force $\vec{F}$ and moment $\vec{M}$ are known,

we can define the instantaneous power P as:

$$P(t) = \vec{F}(t) \cdot \vec{V}(t) + \vec{M}(t) \cdot \vec{\omega}(t), \tag{1.4}$$

and the total energy E over a single drive then becomes:

$$E = \int_{t_{catch}}^{t_{release}} P(t) \mathrm{d}t. \tag{1.5}$$

By taking the ratio of the effectiveness J_x and the energy E we can define the energetic efficiency:

$$\eta_E = \frac{Jx}{E}. \tag{1.6}$$

We note that this quantity is not dimensionless and has the dimension of sm^{-1}, i.e. a reciprocal of velocity. Multiplication of η_E by a reference velocity would yield a dimensionless quantity. However, within the scope of this study we did not find a meaningful reference velocity that led to a dimensionless energetic efficiency that provides more insight than the dimensional energetic efficiency. Therefore, in this study we will use the dimensional energetic efficiency as defined in equation 1.6. Another approach to quantify the efficiency of rowing, is to determine the degree in which the generated impulse $\vec{J}$ is in the desired direction for propulsion, i.e. the x-direction. We define the impulse efficiency η_J as the alignment of the impulse vector with the x-direction:

$$\eta_J = \frac{J_x}{|\vec{J}|}, \tag{1.7}$$

with $0 < \eta_J < 1$, where $\eta_J = 1$ indicates that the impulse vector is directed fully in propulsive direction, and $\eta_J = 0$ that the impulse vector is directed perpendicular to that, i.e. not contributing to propulsion at all. Alternatively, one could use the angle ϕ_J between the impulse vector $\vec{J}$ and the propulsive direction x as a measure of efficiency[2]:

$$\phi_J = \arctan\left(\frac{J_y}{J_x}\right). \tag{1.8}$$

During actual rowing more effective rowing would result in a higher boat velocity, because more propulsion is generated. More efficient rowing would not lead to a higher boat velocity per se. When athletes row more efficient, it is possible that the boat velocity is the same, but the athletes become less tired from rowing. On the other hand, if the athletes spend the same amount of energy and row more efficiently, then they also row more effective. Both the effectiveness and efficiency of a rowing stroke are studied extensively in chapter 3.

1.3. PREVIOUS RESEARCH ON OAR BLADE HYDRODYNAMICS

Forces on the pivot point of the rowing oar were investigated in various studies such as by Hofmijster *et al.* [11] and Lintmeijer *et al.* [13]. However, these studies do not isolate

[2]Note that the impulse efficiency η_J and angle ϕ_J are directly related through $\eta_J = \sin\phi_J$.

the hydrodynamic forces since the force measured on the pivot point includes the force exerted by the athlete on the oar handle, and without additional information it is impossible to reconstruct the hydrodynamic forces from those measurements. Hofmijster *et al.* [10] isolated the oar blade forces by mounting a six-component force/torque transducer in the oar shaft between pivot point and oar blade. An accurate measurement of all components proved difficult due to technical limitations. Nonetheless their work shows that forces on the oar blade are quite complicated. Unfortunately it is very hard to perform a detailed investigation of the flow around an oar during on-water rowing, e.g. by means of particle image velocimetry of flow visualisations. The hydrodynamic forces in rowing, i.e. isolated from the forces exerted by the athlete, has been subject of both experimental and numerical research numerous times in the past as is shown in the review article by Caplan *et al.* [3]. The force due to a steady flow on various rowing oar blades was investigated experimentally by Caplan & Gardner [4] and Caplan & Gardner [5]. In their research a comparison was made between various rowing oar blades using a water flume. Some differences in force response of the various blades are observed due to a change in curvature. However, the flow field itself was not investigated. A numerical study of a steady uniform flow over rowing oar blades was performed by Coppel *et al.* [6] in which unfortunately the chosen turbulence model affected the obtained drag coefficients significantly and also the flow field itself was not investigated. In a later numerical study of steady uniform flow over an oar blade by Coppel *et al.* [7] separation of the flow over the blade at high angles of attack was identified by releasing path lines. Although these experiments and simulations at steady flow conditions are a first step in understanding oar blade hydrodynamics, they do not investigate the flow itself and do not account for a free surface or effect of acceleration of the oar blade.

Research on oar blade hydrodynamics that does account for a free surface and for accelerations of the oar blade was performed by Sliasas & Tullis [16]. They investigated both steady flow over an oar blade as well as unsteady flow, i.e. simulating the actual path of a rowing oar blade, including a free surface using commercially available software. In their research they found that the obtained lift and drag coefficients in the steady and unsteady simulations differed substantially, which is to be expected since the observed large accelerations during rowing will cause an increased force on the oar blade due to added mass. The deformation of the free surface obtained from the unsteady simulations was found to match qualitatively with real-life rowing but a detailed investigation of the flow field was not performed. Barré & Kobus [2] performed towing tank experiments in which a simplified oar blade model moved along a simplified path. Although the path was simplified, the motion was highly dynamic and near a free surface, like in real rowing. Although during these experiments only force data was acquired and no flow analysis was performed, in later research this force data was compared as a benchmark against numerical simulations by Leroyer *et al.* [12]. From those numerical simulations it was concluded that both free surface and unsteadiness effects are crucial features in the generation of propulsive forces, since the simulations incorporating both these features were the only ones to match reasonably well with the experimental data. In a more recent study by Robert *et al.* [15] a realistic oar blade path was simulated using the same software as in Leroyer *et al.* [12]. Again agreement between experiments and simulations was fair. Both Leroyer *et al.* [12] and Robert *et al.* [15] note that viscosity appeared to play a minor role in the obtained

drag and lift coefficients, and therefore an Euler method was used. Also in more advanced simulations by Robert *et al.* [14] that take into account realistic oar blade kinematics an (inviscid) Euler model is used, since the authors deem viscous effects negligible. Unfortunately, by using an Euler method it is very unlikely that the shedding of vortical structures was accurately captured[3], since this is a viscosity-driven phenomenon, while vortex shedding is clearly observed during on-water rowing and appears to be a dominant feature in the flow. The inability to properly predict these vortical structures may be an explanation why the numerical results only 'fit fairly well' when compared to the experiments.

It shows that despite the many attempts it proves difficult to determine the flow field around a rowing oar blade and the flow phenomena governing propulsion in rowing are still largely unknown. Reasons are the turbulent flow, i.e. a Reynolds number Re = $\mathcal{O}(10^5)$ to $\mathcal{O}(10^6)$, large accelerations ($\mathcal{O}$ (1 ms^{-2})), the presence of a free surface, and viscosity driven phenomena like vortex shedding, which all complicate both experiments and numerical simulations.

1.4. CHALLENGES AND RESEARCH OBJECTIVES

To analyse and optimise the rowing propulsion insight must be gained in the flow phenomena and the hydrodynamic forces that are generated by these phenomena. To obtain this insight two options are available: (i) numerical simulations and (ii) experimental measurements. During this research an attempt was made to do numerical simulations of a realistic oar blade following a realistic oar blade path, while accounting for fluid viscosity and resolving the boundary layer on the oar blade in order to simulate boundary layer roll-up and subsequent vortex shedding.

A two-dimensional simulation was carried out using a stylised oar blade while maintaining a realistic oar blade path. The oar blade motion was modelled using a dynamically rotating, stretching, and sliding multi-part grid in Ansys Fluent (Ansys, USA). In order to simulate boundary layer roll-up a wall $y^+ \approx 1$ was used, which required $\mathcal{O}(10^7$ - $10^8)$ cells and time steps of $\Delta t \approx 10^{-4}$ s pushing the readily available computing power to the limit (12 cores, 64 GB). Although the shed vortices in the simulation appeared similar to on-water rowing, the vortices died out quickly due to a very high turbulent viscosity that persists in the entire flow domain by default in Ansys Fluent. The resulting flow field was not comparable to the flow observed during on-water rowing and was deemed too much of a simplification of reality.

A three-dimensional simulation would require even more cells due to the extra dimension. In combination with the required small time steps due to the large accelerations and decelerations this was deemed not viable due to a lack of computational power; one would need access to a supercomputer to carry out such a simulation. Moreover, even if it would have been possible to simulate a realistic oar blade with realistic kinematics while incorporating viscous effects and the free surface, it would have been difficult to validate the results, since no experimental flow field data is available.

Since numerical simulations were not viable it was chosen to carry out an experimental study in a controlled environment, i.e. in a laboratory, such that advanced measure-

[3]Note that Euler methods are able to represent a vortical flow in case the location of flow separation is specified, or when the point of flow separation is clear, e.g. at sharp edges, due to 'numerical' dissipation.

ment techniques such as particle image velocimetry (PIV) can be used. By using a mechanical device to replicate the rowing motion in a controlled environment, it is ensured that the repeatability of the experiments is very good compared to on-water experiments; where both the athletes and outdoor conditions (the weather) are sources of variation. The rowing motion is replicated by an industrial gantry robot (the 'RowBot') with four degrees of freedom, translation over three Cartesian axes and rotation around the vertical axis. The experimental set-up facilitates simultaneous force measurements and PIV measurements such that flow phenomena can be related to distinct parts of the force profiles with relative ease. In addition, the position of the robot head, i.e. the part that holds the oar blade model, is continuously logged. The robot and the model are positioned over an open-top glass tank which measures 2 m × 2 m with a depth of 0.6 m. A more detailed description of the robot is found in appendix A. The experimental set-up that is used varies per chapter and is described in more detail in each chapter.

Due to the maximum velocities achievable by the robot given the limited space in the laboratory and in the tank, the dimensions of the oar blade and its kinematics were scaled by a factor of 0.5; this is discussed in more detail in chapter 3. The full rowing motion including the recovery phase requires a fifth degree of freedom; the rotation of the oar shaft around its axis. However, the drive phase only requires four degrees of freedom, which makes the robot suitable for this research.

1.4.1. RESEARCH OBJECTIVES

To optimise the rowing propulsion a method has to be developed that determines the (hydrodynamic) performance of rowing propulsion; only then can the effect of varying parameters be identified and quantified which is essential for optimisation. To know what parameters affect rowing performance it is required to identify which flow phenomena govern rowing propulsion. The rowing propulsion is then optimised by changing the oar blade geometry. Also, the effect of the depth at which the rowing oar blade is held below the water surface during the starting stroke is investigated; from personal experience, opinions on what oar blade depth results in the best start vary among coaches. The starting stroke is the first stroke in a race where the athletes are waiting for the start signal with their blades submerged in the catch position, similar to figure 1.1(i).

DETERMINE A BEST PRACTICE FOR THE STARTING STROKE

In chapter 2 the effect of different oar blade depths during the starting stroke is investigated. The oar blade model is a flat plate with an aspect ratio of $AR = 2$. Also the oar blade path during the starting stroke, approximately along an arc, is simplified to a straight path. These simplifications are chosen such that the results of the experiments can be compared to readily available experimental results for ordinary flat plates so that the experimental set-up and the applied measurement techniques can be validated.

DEVELOP A METHOD TO DETERMINE THE PERFORMANCE OF ROWING PROPULSION

In chapter 3 a method to determine the hydrodynamic efficiency and effectiveness of the rowing propulsion of a realistic rowing oar blade, in combination with realistic oar blade kinematics, is presented and applied. The efficiency and effectiveness are based on high-frequency force measurements that are integrated over the duration of the drive phase resulting in a robust quantification.

IDENTIFY THE FLOW PHENOMENA GOVERNING ROWING PROPULSION

Flow phenomena governing rowing propulsion are investigated for both the starting stroke (chapter 2) and a rowing stroke (chapter 3).

OPTIMISE THE OAR BLADE GEOMETRY FOR ROWING PROPULSION

Insight in the flow field around the oar blade obtained from PIV measurements on a realistic oar blade in combination with realistic kinematics led to the identification of a jet-like structure that appears to correlate with the impulse efficiency η_J or the angle ϕ_J; it appears that the impulse is not generated exclusively in propulsive direction. Consequently, the oar blade angle is varied in order to align the generated impulse with the propulsive direction in an attempt to find the optimal effectiveness and efficiency. Rowing oars used for on-water rowing can be adjusted in length and lever ratio, but the adjustment of the oar blade angle as proposed in chapter 3 is a novelty.

REFERENCES

[1] ANDERSON, J. D. 1991 *Fundamentals of Aerodynamics (McGraw-Hill Series in Aeronautical and Aerospace Engineering)*. McGraw-Hill College.

[2] BARRÉ, S. & KOBUS, J. M. 2010 Comparison between common models of forces on oar blades and forces measured by towing tank tests. *Proceedings of the Institution of Mechanical Engineers, Part P: Journal of Sports Engineering and Technology* **224** (1), 37–50.

[3] CAPLAN, N., COPPEL, A. & GARDNER, T. 2010 A review of propulsive mechanisms in rowing. *Proceedings of the Institution of Mechanical Engineers, Part P: Journal of Sports Engineering and Technology* **224** (1), 1–8.

[4] CAPLAN, N. & GARDNER, T. N. 2007 A fluid dynamic investigation of the Big Blade and Macon oar blade designs in rowing propulsion. *Journal of Sports Sciences* **25** (6), 643–650.

[5] CAPLAN, N. & GARDNER, T. N. 2007 Optimization of oar blade design for improved performance in rowing. *Journal of Sports Sciences* **25** (13), 1471–1478.

[6] COPPEL, A., GARDNER, T., CAPLAN, N. & HARGREAVES, D. 2008 Numerical Modelling of the Flow Around Rowing Oar Blades (P71). In *The Engineering of Sport 7*, pp. 353–361. Springer, Paris.

[7] COPPEL, A., GARDNER, T. N., CAPLAN, N. & HARGREAVES, D. M. 2010 Simulating the fluid dynamic behaviour of oar blades in competition rowing. *Proceedings of the Institution of Mechanical Engineers, Part P: Journal of Sports Engineering and Technology* **224** (1), 25–35.

[8] ELDREDGE, J. D. & JONES, A. R. 2019 Leading-edge vortices: mechanics and modeling. *Annual Review of Fluid Mechanics* **51**, 75–104.

[9] GRIFT, E. J., VIJAYARAGAVAN, N. B., TUMMERS, M. J. & WESTERWEEL, J. 2019 Drag force on an accelerating submerged plate. *Journal of Fluid Mechanics* **866** (369-398).

[10] HOFMIJSTER, M., KONING, J. DE & SOEST, A. J. VAN 2010 Estimation of the energy loss at the blades in rowing: Common assumptions revisited. *Journal of Sports Sciences* **28** (10), 1093–1102.

[11] HOFMIJSTER, M. J., LANDMAN, E. H. J., SMITH, R. M. & VAN SOEST, A. J. 2007 Effect of stroke rate on the distribution of net mechanical power in rowing. *Journal of Sports Sciences* **25** (4), 403–411.

[12] LEROYER, A., BARRÉ, S., KOBUS, J. M. & VISONNEAU, M. 2010 Influence of free surface, unsteadiness and viscous effects on oar blade hydrodynamic loads. *Journal of Sports Sciences* **28** (12), 1287–1298.

[13] LINTMEIJER, L. L., HOFMIJSTER, M. J., FISCHEDICK, G. A. SCHULTE, ZIJLSTRA, P. J. & SOEST, A. J. VAN 2018 Improved determination of mechanical power output in rowing: Experimental results. *Journal of Sports Sciences* **0** (0), 1–9.

[14] ROBERT, Y., LEROYER, A., BARRÉ, S., QUEUTEY, P. & VISONNEAU, M. 2018 Validation of cfd simulations of the flow around a full-scale rowing blade with realistic kinematics. *Journal of Marine Science and Technology* pp. 1–14.

[15] ROBERT, Y., LEROYER, A., BARRÉ, S., RONGÈRE, F., QUEUTEY, P. & VISONNEAU, M. 2014 Fluid Mechanics in Rowing: The Case of the Flow Around the Blades. *Procedia Engineering* **72**, 744–749.

[16] SLIASAS, A. & TULLIS, S. 2009 Numerical modelling of rowing blade hydrodynamics. *Sports Engineering* **12** (1), 31.

[17] WILLIAMSON, C. H. K. 1996 Vortex dynamics in the cylinder wake. *Annual review of fluid mechanics* **28** (1), 477–539.

2

DRAG FORCE ON AN ACCELERATING SUBMERGED PLATE

In this chapter we present results on the drag on, and the flow field around, a submerged rectangular normal flat plate, which is uniformly accelerated to a constant target velocity along a straight path. The plate aspect ratio is chosen to be $AR = 2$ to resemble an oar blade in (competitive) rowing, the sport which inspired this study. The plate depth, i.e. the distance from the top of the plate to the stagnant air–water interface, the plate acceleration and the plate target velocity are varied, resulting in a plate width based Reynolds number of $4 \times 10^4 \lesssim Re \lesssim 8 \times 10^4$. In our analysis we distinguish three phases; (i) the acceleration phase during which the plate drag is increased, (ii) the transition phase during which the plate drag decreases to a constant steady value upon which (iii) the steady phase is reached. The plate drag force is measured as function of time which showed that the steady-phase plate drag at a depth of $1/5$ plate height (20 mm depth for a plate height of 100 mm) increased by 45% compared to the plate top at the surface (0 mm). Also, it is shown that the drag force during acceleration of the plate increases over time and is not captured by a single added mass coefficient for prolonged accelerations. Instead, an entrainment rate is defined that captures this behaviour. The formation of starting vortices and the wake development during the time of acceleration and transition towards a steady wake are studied using hydrogen bubble flow visualisations and particle image velocimetry. The formation time, as proposed by Gharib et al. (J. Fluid Mech., vol. 360, 1998, pp. 121–140), appears to be a universal time scale for the vortex formation during the transition phase.

This chapter has been published in Journal of Fluid Mechanics **866**, pp 369-398, Grift *et al.* (2019). I thank N.B. Vijayaragavan for his great effort in performing the experiments that were part of his Master of Science research.

2.1. INTRODUCTION

In (competitive) rowing athletes generate a propulsive force by means of a rowing oar blade. During propulsion the oar blade is submerged close to the surface and the athlete exerts a force on the handle of the oar. This causes a reaction force from the water at the other end of the oar, the oar blade, which together with the force at the handle generates the propulsive force at the oar lock, the pivot point on the boat. For optimal performance it is essential to maximise the propulsion caused by this hydrodynamic reaction force at the blade. To achieve this, understanding of the flow field around the oar blade during this propulsive phase is vital. Although it appears that a rowing oar blade moves along a circular path during the drive phase, its motion is all but trivial. The circular path is only observed when moving with the boat. When observed from an earth-bound reference frame the blade moves along a complex cycloid path and is subject to large accelerations and decelerations [5]. This makes the flow around an oar blade highly dynamic and complex with the presence of a free surface possibly further complicating the flow dynamics.

2.1.1. PREVIOUS WORK ON HYDRODYNAMICS IN ROWING

The hydrodynamic forces in rowing, i.e. without the forces exerted by the athlete, has been subject of both experimental and numerical research numerous times in the past, as is shown in the review article by Caplan *et al.* [5]. The force due to a steady flow on various rowing oar blades was investigated experimentally by Caplan & Gardner [6, 7]. In their research a comparison is made between various rowing oar blades using a water flume. Some differences in force response of the various blades are observed due to a change in curvature. However, the flow field itself was not investigated. A numerical study of a steady uniform flow over rowing oar blades was performed by Coppel *et al.* [9] in which unfortunately the chosen turbulence model affected the obtained drag coefficients significantly and also the flow field itself was not investigated. In a later numerical study of steady uniform flow over an oar blade by Coppel *et al.* [10] separation of the flow over the blade at high angles of attack was identified by releasing path lines. Although these experiments and simulations at steady flow conditions are a first step in understanding oar blade hydrodynamics, they do not investigate the flow itself and do not account for a free surface or acceleration of the oar blade.

Research on oar blade hydrodynamics that does account for a free surface and for accelerations of the oar blade was performed by Sliasas & Tullis [38]. They investigated both steady flow over an oar blade as well as unsteady flow, i.e. simulating the actual path of a rowing oar blade, including a free surface using commercially available software. In their research they found that the obtained lift and drag coefficients in the steady and unsteady simulations differed substantially, which is to be expected since the observed large accelerations during rowing cause an increased force on the oar blade due to added mass. The deformation of the free surface obtained from the unsteady simulations was found to match qualitatively with actual rowing, but a detailed investigation of the flow field was not performed. Barré & Kobus [2] performed towing tank experiments in which a simplified oar blade model moved along a simplified path. Although the path was simplified, the motion was highly dynamic and near a free surface like in actual rowing. Although during these experiments only force data was acquired and no flow analysis was performed, in later research this force data was compared as a benchmark against numerical sim-

ulations by Leroyer *et al.* [23]. From those numerical simulations it was concluded that both free surface and unsteadiness effects are crucial features in the generation of propulsive forces, since the simulations incorporating both these features were the only ones to match reasonably well with the experimental data. In a more recent study by Robert *et al.* [34] a realistic oar blade path was simulated using the same software as Leroyer *et al.* [23]. Again agreement between experiments and simulations was fair. Both Leroyer *et al.* [23] and Robert *et al.* [34] note that viscosity appeared to play a minor role in the obtained drag and lift coefficients, and therefore an Euler method was used. Since vortex-shedding is observed during on-water rowing and the generation of vorticity is strongly linked to viscosity, the choice for an inviscid method might be a reason why the numerical results only 'fit fairly' well when compared to experiments. On the other hand, inviscid numerical models have been successfully used to describe a start-up vortex during the self-similar stage, as reported by Pullin [32], Krasny & Nitsche [22], and Luchini & Tognaccini [25]. The above overview shows that despite the many attempts it proves difficult to determine the flow field around a rowing oar blade, and the flow phenomena governing propulsion in rowing are still largely unknown; reasons are the turbulent flow, i.e. a Reynolds number Re = $\mathcal{O}(10^5)$ to $\mathcal{O}(10^6)$, large accelerations, the presence of a free surface, and viscosity driven phenomena like vortex shedding which all complicate both experiments and numerical simulations.

2.1.2. A GENERALISATION OF THE PROBLEM

In this study we investigate the effect of the free surface and the effect of the acceleration on the generated drag force on a simplified geometry. Instead of a rowing oar blade we use a rectangular plate with the same aspect ratio as an oar blade (AR = 2) on a scale of 1:2, and instead of the complex cycloid path our plate follows a linear path as is shown in figure 2.1. This linear path may not be very representative for actual rowing at cruising velocity, but it is representative for the start stroke of a race (where the boat is starting from rest). In that case, the oar blade follows an approximately circular path and the oar blade is oriented perpendicular to the flow. The plate is then submerged at different depths h and is accelerated with an acceleration a towards a constant velocity V, as shown in figure 2.2, such that the flow becomes turbulent, at a Reynolds number Re > 10^4. This enables the assessment of the effect of the free surface and acceleration on the plate drag in turbulent flow conditions. Although this fundamental approach may not capture the intricate detailed dynamics and flow patterns during actual rowing, it does isolate the principal effects of the free surface and acceleration on the drag of an oar-like geometry.

By using a more general definition, the applicability of this study becomes broader. For instance, in aquatic locomotion the Basilisk lizard, sometimes dubbed J.C. lizard, is able to run over water by generating a highly dynamic flow close to the air-water interface [18] through a mechanism called 'surface slapping' which generates force by buoyancy, added mass, and inertia [4]. The same mechanism forms the inspiration for water running robots [20]. Of course, also the design of more traditional maritime craft or the field of coastal engineering profits from a better understanding of the effect of acceleration causing added mass and the presence of a free surface affecting drag force. Also in other sports where athletes generate a highly dynamic flow close to the surface this study can be of interest, e.g. in swimming during breast stroke or front crawl [27] or in canoeing [39]. Accelerat-

ing plates are also used to model insect flight or flapping wings of small birds that both appear to have a remarkably high aerodynamic performance due to a leading edge vortex enhancing lift and interaction between wing and vortical wake contributing to net thrust [12, 14].

2.1.3. PREVIOUS WORK ON ACCELERATING PLATES

Obviously, we are not the first to investigate drag on a flat plate. Already at the beginning of the previous century Ludwig Prandtl studied the flow around a plate moving perpendicular to its surface in his work which translates as 'Motion of fluids with very little viscosity' [31]. In the work of Hoerner [17] an overview of the research up to 1954 on the drag of plates normal to a steady flow is found. For an accelerating motion, or flow depending on the frame of reference, we expect an increase in drag on the plate due to added mass. Although the term added mass, or alternatively hydrodynamic mass, is a common enough term in fluid mechanics, little research has been done on added mass for accelerating plates. For sufficiently small motions from rest the added mass effect can be captured by a single coefficient which is fully defined by the plate geometry [29, 30, 43].

The flow around and the drag on a uniformly accelerating plate during larger motions has been of interest since the second half of the previous century of which Koumoutsakos & Shiels [21] provide a clear and concise summary of both numerical and experimental work carried out. It is evident that a plate uniformly accelerated from rest produces a vortex as was readily observed by Prandtl [31]. The generation of this vortex has four stages, as defined by Luchini & Tognaccini [25]. During the first three stages, i.e. the Rayleigh stage, viscous stage, and the self-similar inviscid stage, a vortex is formed and starts growing, but remains attached to the body at which it is formed and is independent of geometry. Only during the last stage, during the vortex expulsion, the vortex starts lagging behind the body. Most experimental work and numerical work is limited in Reynolds number, Re $\approx \mathcal{O}(10^3)$, or is on the very early stages of an accelerating plate, i.e. the first three stages of vortex formation. However, the first three stages already occur within a small motion of the plate, i.e. within a travelled distance of 0.5 to 1 times the plate height [42]. Each of our experiments runs far into the fourth phase, which has not been investigated in great detail.

In the work of Koumoutsakos & Shiels [21] numerical simulations of an accelerating plate in two-dimensional viscous flow were performed up to Re = 1000. It was found that for a uniformly accelerated plate a Kelvin-Helmholtz-type instability was induced in the separating shear layer, which appears to be intrinsic behaviour of the flow. Previously, when this behaviour was observed during experiments by Lian & Huang [24] the same observed flow behaviour was attributed to experimental defects. However, this behaviour being intrinsic to the flow was later disputed once again by Xu & Nitsche [42], as they showed that by increasing the simulation resolution the instabilities disappear. However, Schneider *et al.* [36] report that the instabilities are affected by the shape of the plate tip which suggests that it is intrinsic to the flow.

For an impulsively started plate at constant velocity V, Koumoutsakos & Shiels [21] defined the dimensionless time $t^* = Vt/l_b$, with t the dimensional time; which equals the number of plate heights travelled. The dimensionless time t^* for a plate of height l_b at constant acceleration a is defined by Koumoutsakos & Shiels [21] as $t^* = at^2/l_b$. The

dimensionless time t^* is then equal to two times the number of plate heights travelled by the plate. Koumoutsakos & Shiels [21] found that by introducing t^* the scaled drag coefficient collapsed on a single curve. In the current study the dimensionless time t^* is defined as the number of plate heights travelled. A similar notation was adopted by Xu & Nitsche [42] who reported that it was more suitable to compare results with different accelerations at the same distances travelled than identical times travelled. Gharib *et al.* [15] called this dimensionless time the *formation time* where it proved to be a universal time scale for the generation of a vortex ring by a piston. Also Ringuette *et al.* [33] used the formation time t^* to identify vortex shedding events at the edges of a uniformly accelerated semi-infinite plate normal to the flow. Also in this study the formation time appears to be a useful scaling parameter with respect to vortex shedding. Throughout this study, parameters and variables are expressed in their dimensional form unless their dimensionless counterpart proves a valuable addition to the analysis, i.e. some universal scaling becomes apparent by their use.

The experiment carried out by Ringuette *et al.* [33] somewhat resembles our experiment. The main difference is that our plate is not semi-infinite but three-dimensional, and our plate is not piercing the surface but is submerged below the surface. Also the Reynolds number in our experiments are an order of magnitude larger, i.e. $\mathcal{O}(10^4)$ versus $\mathcal{O}(10^3)$. In their work, force measurements are combined with visualisation techniques and quantitative flow measurements by means of particle image velocimetry (PIV). The latter is used to obtain the vorticity in the flow and from there the dimensionless circulation which can be used to identify vortex shedding events. In this study we use similar techniques to investigate the flow around the plate.

2.2. EXPERIMENTAL SET-UP

Figure 2.1 shows the experimental set-up used in this study. All experiments are done in an open-top glass tank with a horizontal cross-section of 2 m × 2 m and a height of 0.6 m. The dimensions of the tank are chosen as large as practically possible to avoid blockage effects and wall effects. The tank is filled with water up to a level of 0.5 m to avoid spilling over the edge of the tank. The flat plate used in this study has a width l_a = 200 mm and a height l_b = 100 mm which results in a surface blockage ratio of 0.02, i.e. the ratio of the plate area (0.2 m × 0.1 m) over the tank cross-section perpendicular to the direction of motion of the plate (2 m × 0.5 m). According to literature, e.g. West & Apelt [40], at this ratio the presence of the walls of the tank do not have a significant effect on the drag. To match the rowing oar blade on a 1:2 scale the plate thickness l_c should be 2.5 mm. However, to avoid flapping or flexing of the plate a compromise was reached at a plate thickness l_c = 4 mm. The plate is aligned such that its major dimensions l_a and l_b are parallel to the y and z direction, respectively, see figure 2.1b. The plate is mounted to an industrial robot arm (Reis Robotics RL50) with a streamlined strut piercing the air-water interface. A force/torque transducer (F/T transducer) is installed between the robot arm and the strut to measure the hydrodynamic forces acting on the plate. The hydrodynamic forces on the streamlined strut are considered to be negligible compared to those on the flat plate.

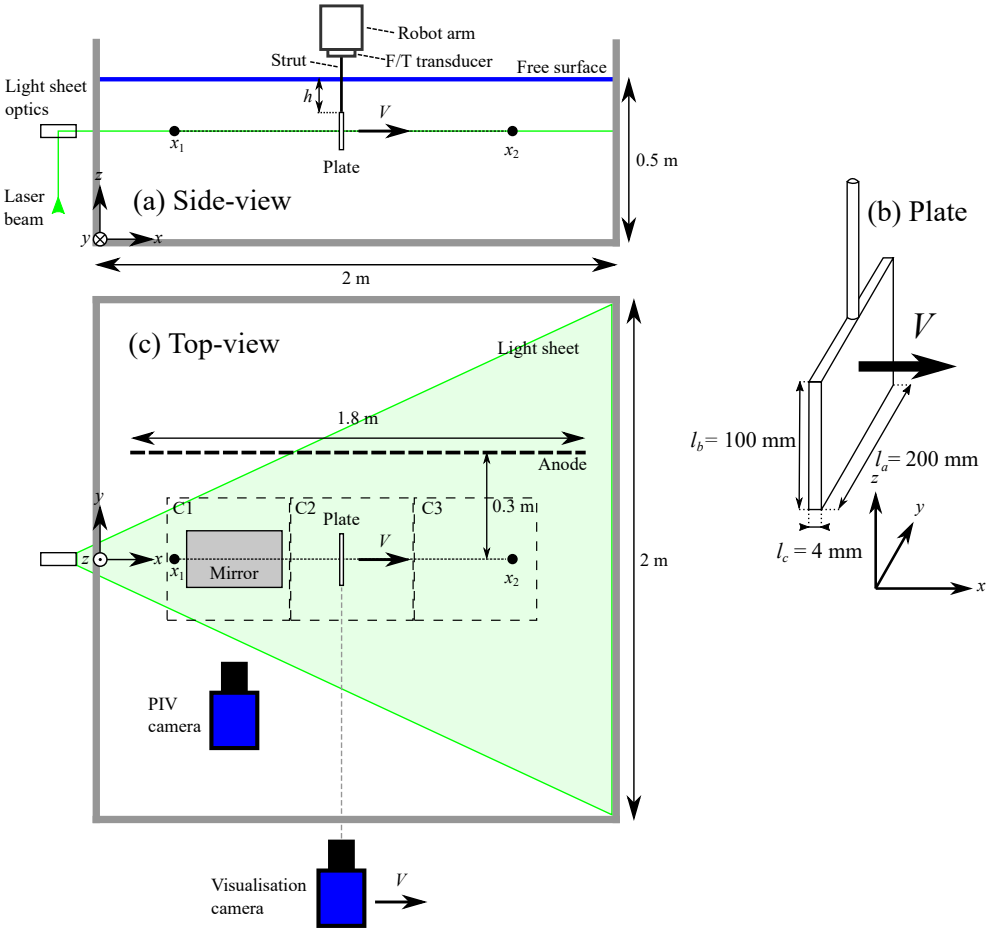

Figure 2.1: Schematic of the experimental set-up. (a) Side-view of the set-up with the robot arm holding the plate moving from x_1 to x_2 at velocity V at a distance from the free surface h. (b) Plate dimensions and orientation. (c) The top-view showing the horizontal light sheet used for particle image velocimetry (PIV) that crosses the plate at half-height. The PIV camera images the field of view via a mirror. Both the camera and mirror are positioned underneath the tank and are moved to different position for each field of view (C1, C2, C3). Also, the anode and the camera moving with the plate for the flow visualisations are shown.

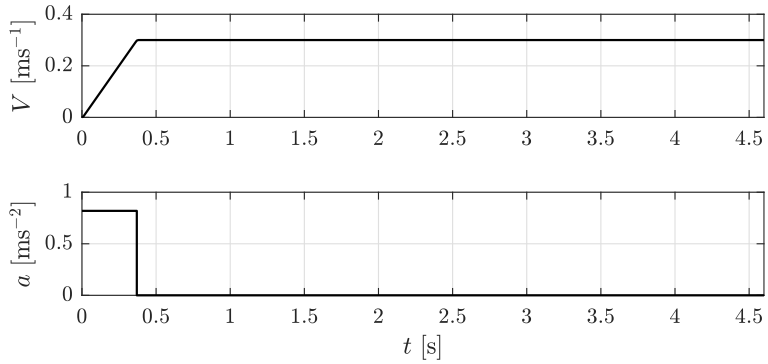

Figure 2.2: Plate velocity V (top) and plate acceleration a (bottom) as a function of time t.

2.2.1. KINEMATICS

The robot moves the flat plate along a straight line in the x-direction, from x_1 to x_2, over a distance of 1.4 m (figure 2.1), starting and stopping at a distance of three times the plate height l_b from the walls, such that the walls do not affect the flow around the plate. The velocity fields obtained from the PIV measurements show that the flow is unperturbed, i.e. a flow velocity magnitude <1% of the plate velocity V, at 2.4 plate heights l_b ahead of the plate. To investigate the effect of the free surface on the drag, the immersion depth h, defined as the distance between the top edge of the plate and the water surface, as shown in figure 2.1, is varied from 0 to 200 mm. The plate is linearly accelerated to a velocity V = 0.30 ms^{-1}; see figure 2.2. The acceleration of the robot is set to a = 0.82 ms^{-2} so that the prescribed velocity of V = 0.30 ms^{-1} is reached in 0.36 s. At V = 0.30 ms^{-1} the Reynolds number (using the plate width l_a as a characteristic length) is Re = 60×10^3, which is well in the turbulent regime. Higher velocities would complicate the experiments by increasing the settling time of the turbid water in the tank between experiments, and would increase the risk of splashing and spills. During the experiments only very small capillary waves are observed, which hold very little energy. Due to the absence of waves we expect a small Froude number, which is defined as

$$Fr = \frac{V}{\sqrt{gL}}, \tag{2.1}$$

where g is the gravitational acceleration, and L is a representative length scale. However, it is hard to define a representative length scale in the geometry and/or water depth used in this experiment. Length scale L could be taken equal to, e.g. the plate major dimensions l_a = 0.2 m, l_b = 0.1 m, some reference length $\sqrt{l_a l_b}$, or the water tank depth (0.5 m), which leads to Fr = 0.21, 0.30, 0.25, and 0.14, respectively. These are all well below the critical Froude number Fr = 1.

2.2.2. FORCE AND PATH DATA ACQUISITION

The robot itself provides the data on the position $x(t)$ and the velocity $V(t)$ at a default rate of 92 Hz. The robot position data is within 0.1 mm repeatable, with a resolution of 1

μm. To analyse the forces on the flat plate a force (ATI 6-DOF) is used that measures the force at a rate of 10 kHz.

2.2.3. HYDROGEN BUBBLE FLOW VISUALISATION

To visualise the flow we use hydrogen bubble flow visualisation. Installed on the front face of the plate (facing the positive x-direction) is a 0.6 mm thick copper wire mesh that acts as the cathode. A 1.8 m long stainless steel screen that is placed parallel to the plate path at a distance of 0.6 m acts as the anode, see figure 2.1. Using an electric potential of 30 V hydrogen bubbles are created at the front surface of the plate. To increase the bubble production rate to a level suitable for visualisation the conductivity of the water was increased by adding 2.5 kg of sodium sulphate. The hydrogen bubbles were illuminated through the glass bottom of the tank using flood lights (3×400 W). Images of the hydrogen bubbles were taken with a high-speed camera (Phantom VEO 640L with a 105 mm Nikon lens) at a frame rate of 500 frames per second (fps). During the recording the camera moved (manually) with the plate in the positive x-direction such that the plate and its wake remained in the camera's field of view. It was found that force signals produced during runs with and without hydrogen bubble flow visualisation do not differ. The variations were similar as found between different runs using an identical set-up.

2.2.4. PARTICLE IMAGE VELOCIMETRY

To quantify the flow field we used planar Particle Image Velocimetry (PIV). The field of view is in the horizontal x,y-plane through the centre of the plate. A 4 megapixel high-speed camera (LaVision Imager Pro HS) was used to capture the flow through the glass bottom upwards in the positive z-direction at a frame rate of 1000 fps. To capture the entire run of the plate over 1.4 m we captured the flow at three different locations along the x-axis, each time using a field of view of approximately 0.6 m × 0.6 m that were stitched together to cover the entire run, as shown in figure 2.1. Neutrally buoyant fluorescent spherical tracer particles (Cospheric UVPMS-BR-0.995, 53-63 μm diameter) were added to the flow (10 g) and were illuminated using a 532 nm Nd-YAG 150 W laser (Litron LDY304-PIV). The acquired images were analysed using commercial software (LaVision DaVis 8.4). To create image pairs from the sequential images acquired at 1000 fps every n-th frame was paired with the (n+6)-th frame resulting in a 6 ms exposure time delay Δt to ensure sufficient displacement of the particle images in the region of interest, i.e. the wake behind the plate. A multi-pass correlation based PIV algorithm was used to obtain the flow velocity field from the image pairs. The interrogation windows of the three subsequent passes were 48×48 pixels for the first pass, and 24×24 pixels for the second and third passes. A 50% overlap between adjacent interrogation positions was used. This resulted in velocity vector fields with a vector spacing of 3.2 mm and a cumulative first and second vector choice of >98% in the area of interest, i.e. in the wake of the plate.

2.3. RESULTS

2.3.1. TYPICAL RESULT FROM THE FORCE MEASUREMENTS

During each run the instantaneous force F_x (perpendicular to the plate surface) is sampled at a rate of 10 kHz. The grey line in figure 2.3 represents F_x as a function of time

for an experiment with a target velocity $V = 0.30$ ms^{-1}, a plate depth of $h = 100$ mm, and an acceleration of $a = 0.82$ ms^{-2}. As one can see, the 10 kHz sampled raw signal shows significant fluctuations. All calculations and analyses are performed using the unfiltered signals. However, for better readability the signal is filtered using a second order Savitzky-Golay filter [35] with a filter width of 201 samples, i.e. 0.02 s. The black line in figure 2.3 represents the filtered signal. The force signal exhibits a clear initial peak at 0.36 s which coincides with the time when the plate reaches its maximum velocity of $V = 0.30$ ms^{-1}; see figure 2.3 (bottom). The initial peak is due to the added mass and the acceleration of the plate, as is discussed in detail in section 2.3.7. The time interval $0 < t < 0.36$ s is called the 'acceleration phase' and is indicated by A in figure 2.3. After the peak, the force gradually decreases and finally reaches a steady value for $t \gtrsim 3.4$ s. This phase is called the 'steady phase' and is indicated by C. The time interval in between the initial peak and the beginning of the steady phase (0.36 s $< t < 3.4$ s) is called the 'transition phase' and is indicated by B. The measurement ends at t = 4.6 s. It is noted that the force signal shows two distinct local maxima during the transition phase B, indicated as 'peak 1' and 'peak 2' in figure 2.3. In section 2.3.6 it is shown that these peaks are related to the development of large flow structures in the wake of the plate. Also, throughout the experiment high-frequency oscillations are present in the force signal, which is due to Kelvin-Helmholtz-like instabilities in the shear layer, which is further discussed in section 2.3.4. Right after starting the plate we observe a local peak followed by a dip in the force signal, i.e. a step response as indicated in figure 2.3. This is a result of the finite stiffness of the plate, the force transducer, and the streamlined strut that connects the two. This finite stiffness causes a typical response of a mass-spring-damper system to a step function; in this case the sudden acceleration of the plate causes a sudden force due to the hydrodynamic mass and mass of the plate [28].

2.3.2. THE EFFECT OF THE PLATE DEPTH ON THE STEADY PHASE DRAG

The plate is moved through the tank for different immersion depths h to investigate the effect of the free surface on the drag on the plate. The immersion depth h is varied between 0 to 200 mm in a randomised order. In total 140 runs were carried out.

The drag force F_x during the steady phase is expressed as

$$F_x = \frac{1}{2}\rho V^2 C_D A, \tag{2.2}$$

where ρ is the fluid density, V the plate velocity, A the frontal area of the plate, and C_D the steady-phase drag coefficient. For each run the steady-phase drag coefficient C_D is calculated and plotted in figure 2.4 using open markers, where each marker represents C_D of a single run at a given depth h. The steady phase drag coefficient C_D reaches a minimum value of $C_D = 1.10$ for $h = 0$, i.e. when the top of the plate is at the surface. For larger values of h, i.e. when the plate is submerged, the drag coefficient increases to a peak value of $C_D = 1.60$ at a depth $h = 20$ mm; a relative increase of 45%. When the plate is submerged further below the surface the drag coefficient decreases, and a constant value of C_D=1.3 is reached for large h.

To the knowledge of the authors, the observed behaviour of C_D with respect to the plate depth h has not been reported previously. However, to be able to make a comparison with literature we consider two limiting cases. The first limiting case occurs for large h

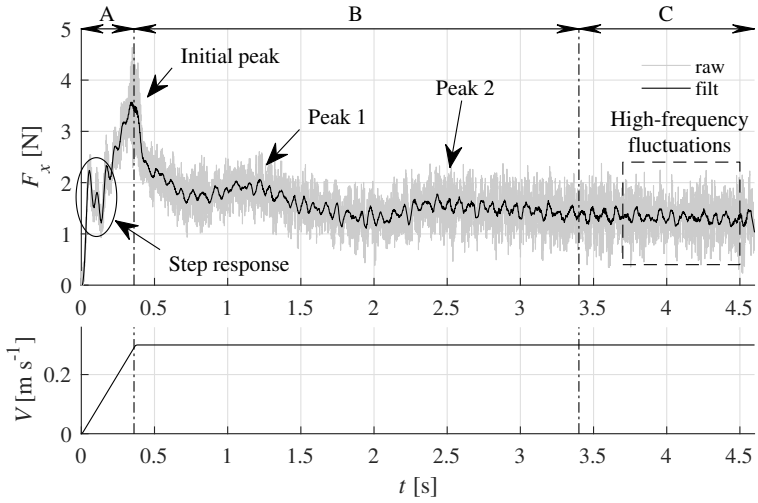

Figure 2.3: (top) a typical unfiltered force signal F_x sampled at 10 kHz (grey) and the filtered force signal (black). Throughout the force signal high-frequency oscillations are present which are caused by Kelvin-Helmholtz-like instabilities in the shear layer as discussed in section 2.3.4. Right after starting the plate we observe a step response due to the finite stiffness of the plate, force transducer and the strut which connects the two. (bottom) The plate velocity V as a function of time.

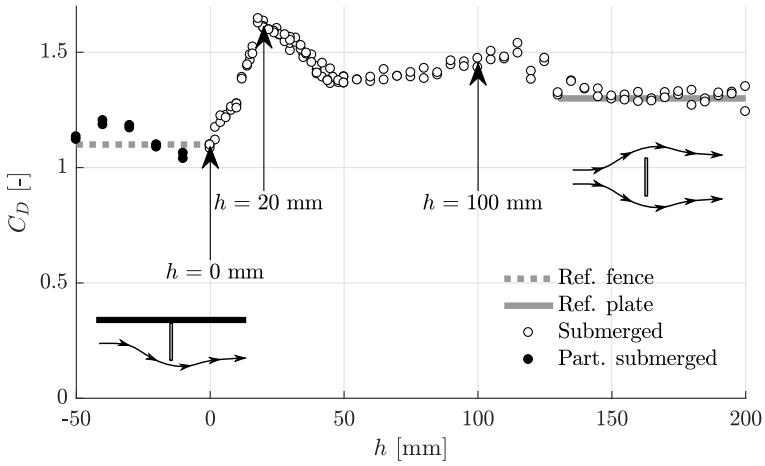

Figure 2.4: The steady-phase drag coefficient C_D as function of plate depth h. For reference the dashed line gives the C_D value for flow over a fence (C_D = 1.10 [19]) and the solid line shows the reference value C_D = 1.30 for flow around a plate (AR = 2) in deep water moving perpendicular to its surface (this study).

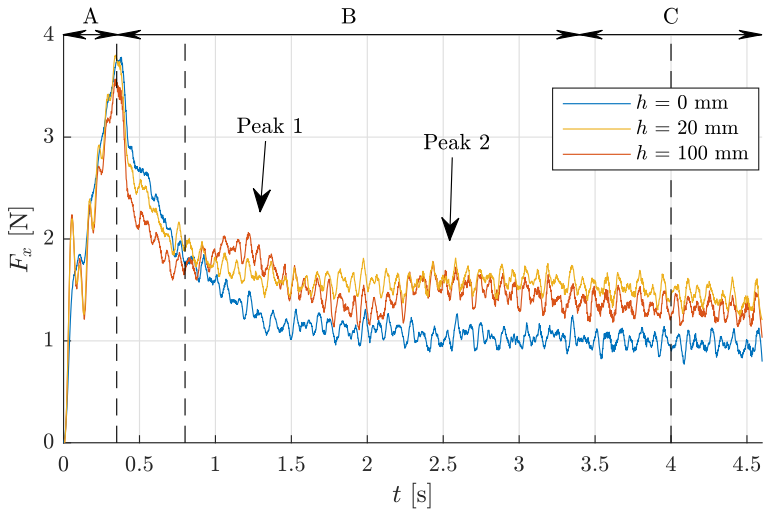

Figure 2.5: The drag force signals $F_x(t)$ for the three selected plate depths, h = 0 mm, h = 20 mm, and h = 100 mm. The vertical dashed lines indicate time instances t_1, t_2, and t_3 when snapshots of the hydrogen bubble flow visualisation were taken as discussed in section 2.3.5.

where the free surface does not affect the drag on the plate any more. For the deep water cases we found C_D = 1.30, which is in close agreement with a value of C_D = 1.26-1.32 for a fully submerged plate with AR = 6 [37] and C_D = 1.2-1.26 for square plates [3]. Another limiting case occurs for h = 0 mm, where we compare the measured drag coefficient with that of a fence, as if the free surface acts as a wall such that the flow does not pass over the top of the plate. Again the found drag coefficient C_D = 1.10 matches well with values found in literature C_D = 1.05-1.12 [19]. The assumption that the plate acts like a fence is verified by letting the plate pierce the surface such that no water flows over the plate, i.e. h <0. The drag coefficients for a partially submerged plate are represented by the closed markers in figure 2.4. Of course, for this surface piercing case the frontal projected area of submerged part of the plate is used for calculating C_D.

2.3.3. INSTANTANEOUS FORCE SIGNALS FOR SELECTED DEPTHS

Three cases are selected for further analysis: the surface case h = 0 mm, the maximum drag case h = 20 mm, and the case h = 100 mm, which equals one blade height l_b. The surface case (h = 0 mm) corresponds to the neutrally buoyant position of an actual rowing oar blade, h = 100 mm, i.e. one blade height, is the practical limit of immersion during actual rowing, and the maximum drag case (h = 20 mm) would be optimal for propulsion. Note that a local minimum and trend break can be seen at h = 50 mm. Although not investigated in this study, we speculate that two drag enhancing mechanisms play a role at this depth which is further discussed in section 2.3.6. The flow visualisations in section 2.3.5 show that the case of h = 100 mm develops a symmetric wake (top-bottom) which suggests it may also be representative for a fully submerged plate. The three cases are indicated in figure 2.4. For the three selected depths, i.e. h = 0 mm, h = 20 mm, and h =

100 mm, experiments are carried out at a velocity V= 0.30 ms^{-1} and an acceleration a = 0.82 ms^{-2}. The instantaneous drag force profiles for these three cases are shown in figure 2.5. It is observed that for all three cases the plate drag is rapidly increasing during the acceleration phase (A), and the maximum drag is reached at the end of this phase. For the case h = 0 mm, the drag force is significantly lower during most of the transition phase (B) and during the steady phase (C). For the case h = 20 mm the drag is higher than in the other cases for t > 1.5 s, which also follows from figure 2.4. Significant differences occur during the transition phase. The force signals show a very different decay to their steady phase values. The case h = 0 mm initially shows the slowest decay but reaches the lowest steady state drag value, while the case h = 100 mm shows the fastest decay but eventually reaches a relatively high steady-phase drag value. Also, the peaks 1 and 2 are only present during the transition phase (B) of the case h = 100 mm.

The drag signals for the three selected cases all show a steep increase during the acceleration phase and a relatively gradual decrease during the transition phase towards the steady phase. Traditionally, the steady phase drag force is described by equation 2.2. However, when dealing with an accelerating object in a quiescent fluid the effect of the added mass must be incorporated in the description of the drag force F_x:

$$F_x(t) = F_{CD}(t) + F_{vm}(t) = \underbrace{\frac{1}{2}\rho V(t)^2 C_D A}_{F_{CD}(t)} + \underbrace{\overbrace{(m_p + m_h)}^{m_v} a(t)}_{F_{vm}(t)}, \tag{2.3}$$

where F_{CD} is the steady phase drag force and F_{vm} the product of the virtual mass m_v and the plate acceleration a. The virtual mass m_v is the sum of the plate mass m_p and the hydrodynamic mass m_h. All variables in equation 2.3 are known except for the hydrodynamic mass m_h. The plate velocity $V(t)$ and the plate acceleration a are prescribed as previously shown in figure 2.2. For each run the value for C_D is taken from figure 2.4. The plate mass m_p = 0.400 kg, while the hydrodynamic mass m_h for a submerged geometry accelerating from rest is estimated by using an empirical correlation. For a rectangular flat plate with an aspect ratio of AR = 2 for inviscid frictionless flow the hydrodynamic mass is modelled as [29]:

$$m_{h(Patton)} = 0.84\frac{\pi}{4}\rho l_a l_b^2 = 1.3\,\text{kg}, \tag{2.4}$$

where l_a and l_b are the major dimensions of the plate (with l_a>l_b). Alternatively, Yu [43] provides an empirical correlation valid for arbitrary plate aspect ratio and plate thickness l_c:

$$m_{h(Yu)} = \rho\left[0.788\frac{l_a^2 l_b^2}{(l_a^2 + l_b^2)^{\frac{1}{2}}} + 0.0619 l_a l_b l_c^{\frac{1}{2}}\right]. \tag{2.5}$$

Figure 2.6 shows the measured drag force $F_x(t)$ for h = 100 mm, next to the theoretical drag force, equation 2.3 with m_h according to equation 2.5. The predicted initial peak in drag force of 2.8 N significantly underestimates the measured peak of 3.6 N. When using expression 2.4 for the hydrodynamic mass, the initial peak is estimated even lower at 2.6 N. Also, the predicted force shows a sharp drop as soon as the acceleration of the plate ends at t = 0.36 s. This is because a force is no longer required for accelerating the virtual mass m_v. However, in the measurements a much more gradual decrease in drag force

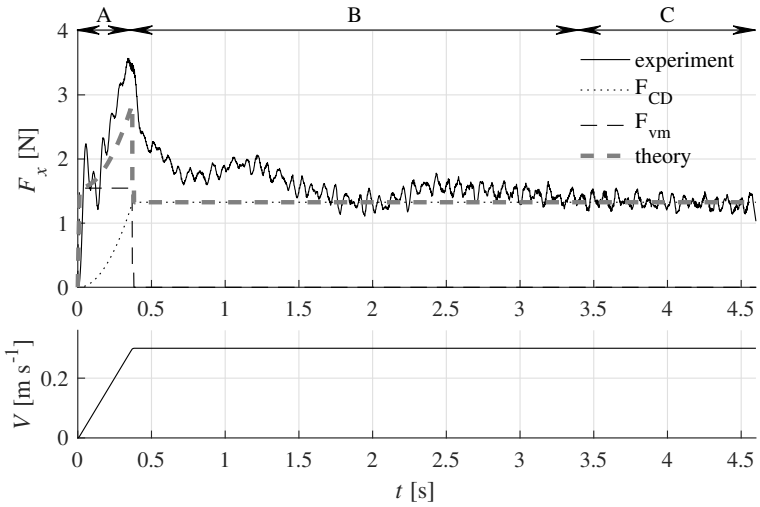

Figure 2.6: The experimentally determined drag force signal $F_x(t)$ for h = 100 mm together with the theoretical drag force and its components F_{CD} and F_{vm} according to equation 2.3 with the hydrodynamic mass m_h according to equation 2.5.

after the initial peak at t = 0.36 s is observed. During experiments, upon accelerating the plate for h = 0 mm and h = 20 mm, a vortex pair is visible at the free surface which is a viscous effect, potentially explaining the mismatch between theory and experiment since the correlations for the hydrodynamic mass are for inviscid flow only. The formation of these vortices is further addressed in section 2.3.5.

ALTERNATIVE FORMULATION OF THE EMPIRICAL CORRELATION BY YU

In the correlation proposed by Yu [43] in the second term, i.e. the term that models the effect of the plate thickness l_c, the fitting constant has a dimension of $m^{\frac{1}{2}}$, which is considered to be rather awkward. Payne [30] even states that the correlation is therefore incorrect. With 0.788 close to $\pi/4$ the equation can be rewritten, while satisfying symmetry with respect to l_a and l_b, to

$$m_h = \rho \frac{l_a^2 l_b^2}{(l_a^2 + l_b^2)^{\frac{1}{2}}} \left[\frac{\pi}{4} + A \left(\left[\frac{l_c}{l_a} \right]^{\frac{1}{2}} + \left[\frac{l_c}{l_b} \right]^{\frac{1}{2}} \right) \right] \tag{2.6}$$

where A is a dimensionless fitting parameter. Based on the normalised L2 norm the fitting parameter found is A = 0.190, which yields a mean difference between the experimental data by Yu [43] and equation 2.6 of 0.015 with a standard deviation σ = 0.0135. Interestingly, equation 2.5 as proposed by Yu [43] provides a better fit with a mean difference of 0.0099 with a standard deviation σ = 0.0073.

2.3.4. SHEAR LAYER INSTABILITIES

As described in the introduction, many studies investigating accelerating flat plates encounter vortices which are formed in the shear layer between the wake of the plate and

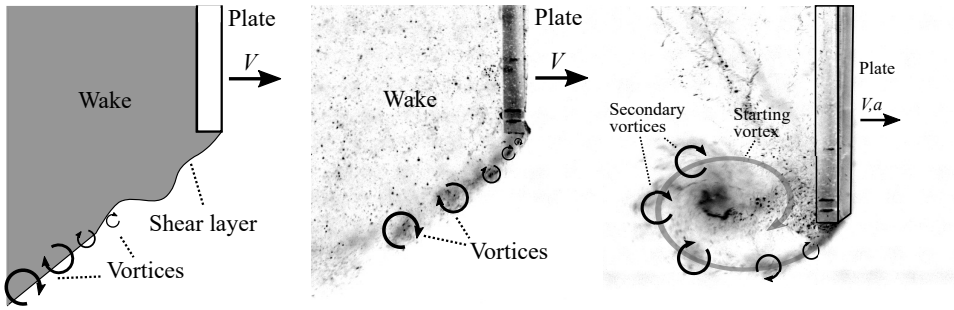

(a) (b) (c)

Figure 2.7: (Side view) (a) The flow separates at the plate edge. At some distance from the plate vortices are formed due to the Kelvin-Helmholtz-like instability in the shear layer coming from the plate edge. (b) At constant velocity small vortices are generated in the shear layer and shed into the wake, similar to the observations by Prandtl [31]. (c) The shear layer with the smaller secondary vortices rolls up during the acceleration phase to form the large starting vortex in a very similar way as was observed by Lian & Huang [24].

the flow separating at the plate edge, e.g. Lian & Huang [24]. The mechanism by which these vortices are generated is similar to that of the Kelvin-Helmholtz instability and is depicted in figure 2.7a. These shear layer instabilities are very close to the plate and can be seen in the force signal; see figure 2.3. These are also visible in the flow visualisations discussed in section 2.3.5, where the hydrogen bubbles end up in the vortex cores; see figure 2.7c. Not only during the acceleration phase, but also during the other phases, i.e. where the plate travels at constant velocity, the secondary vortices are generated in the shear layer at a consistent frequency. When the starting vortex has disintegrated the generated secondary vortices are simply shed into the wake as shown in figure 2.7b. The frequency at which the vortices are generated was determined based on the flow visualisations for each h at $a = 0.82$ ms^{-2} and $V = 0.20^{-1}$ and 0.30 ms^{-1} and was found to be 17 Hz. The power spectrum of the drag force signal consistently shows a peak at this frequency for all runs. The power spectra determined for different values of acceleration, velocity, and immersion depth, were all similar, i.e. the eight most dominant frequencies all lie in the range of 13-20 Hz with the most dominant frequency at approximately 17 Hz. Minor variations between runs are observed. We hypothesise that these variations are due to perturbations introduced by the experimental apparatus that might be different for each run; see also Lian & Huang [24].

2.3.5. FLOW VISUALISATIONS

To determine what causes the discrepancy between the predicted plate drag (based on a constant added mass coefficient) and measured plate drag, the flow around the plate is visualised for the three selected plate depths, $h = 0$ mm, $h = 20$ mm, and $h = 100$ mm. The acceleration is again set to $a = 0.82$ ms^{-1} and the velocity $V = 0.30$ ms^{-1} for all three runs. During each run the camera moves with the plate while viewing the plate and its wake from the right-hand side. Snapshots are taken at three different time instants, i.e. (i) $t_1 = 0.35$ s, close to the end of the acceleration phase (A), (ii) at $t_2 = 0.8$ s during the transition phase (B), (iii) and $t_3 = 4.0$ s during the steady phase (C). t_1, t_2, and t_3 are also marked in

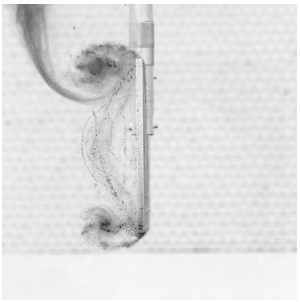

(a) $h = 100$ mm, $t = 0.35$ s. Acceleration phase.

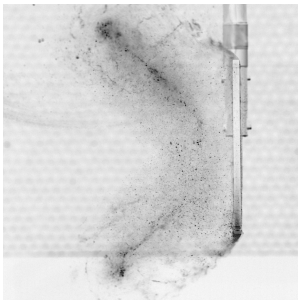

(b) $h = 100$ mm, $t = 0.80$ s. Transition phase.

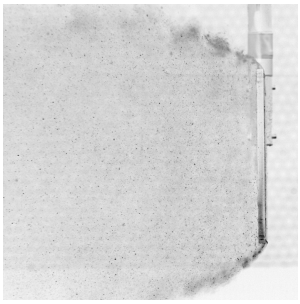

(c) $h = 100$ mm, $t = 4.00$ s. Steady phase.

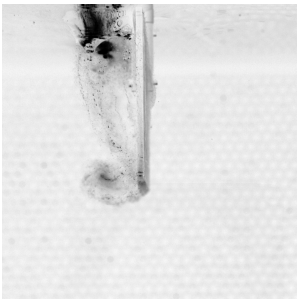

(d) $h = 0$ mm, $t = 0.35$ s. Acceleration phase.

(e) $h = 0$ mm, $t = 0.80$ s. Transition phase.

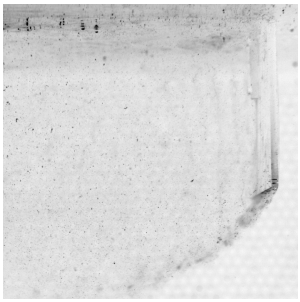

(f) $h = 0$ mm, $t = 4.00$ s. Steady phase.

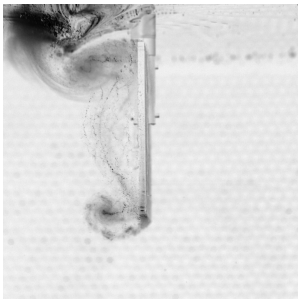

(g) $h = 20$ mm, $t = 0.35$ s. Acceleration phase.

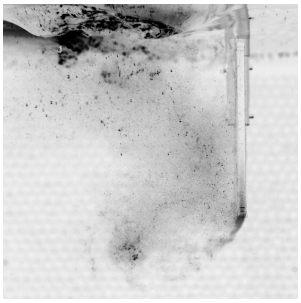

(h) $h = 20$ mm, $t = 0.80$ s. Transition phase.

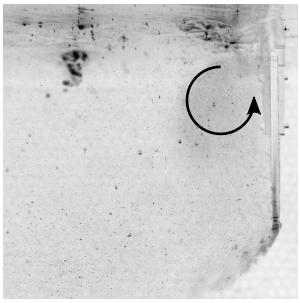

(i) $h = 20$ mm, $t = 4.00$ s. Steady phase.

Figure 2.8: (Side view) Flow visualisations using hydrogen bubbles generated at the plate surface for each selected depth h, at a plate acceleration $a = 0.82$ ms^{-2}, and plate velocity $V = 0.30$ ms^{-1}. The hydrogen bubbles collect in the cores of the vortices that are formed in the shear layer and wake.

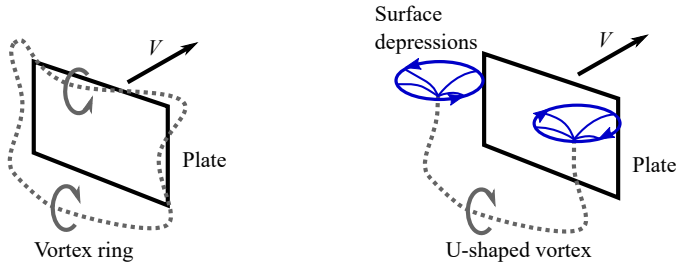

(a) h = 100 mm. (b) h = 0 mm.

Figure 2.9: Vortex formation during the acceleration phase. In the case of h = 100 mm (a) the plate is fully submerged and a closed vortex ring is formed behind the plate. In the case of h = 0 mm (b) the top of the plate coincides with the water surface, and a closed vortex ring cannot be formed. Instead, a U-shaped vortex is formed, which attaches to the surface with both ends, creating surface depressions.

figure 2.5. Flow visualisation movies are available in the supplemental material for h = 0 (movie1), 20 (movie2), and 100 mm (movie3)[1].

Figure 2.8 (a-c) shows the development of the flow for the deep water case h = 100 mm. Immediately after setting the plate in motion (t = 0 s) a vortex ring forms at the plate edges, closely trailing behind the plate until the end of the acceleration phase; see figure 2.8a. During the transition phase this vortex ring deforms: the top and bottom of the ring move away from the plate, while the part of the ring that formed at the left and right edges of the plate contracts towards the centre of the plate, remaining close to the plate surface; see figure 2.8b. During the transition phase the vortex ring continues to stretch and finally breaks up after which the wake gradually assumes its steady shape; see figure 2.8c.

In the h = 0 mm case, the top face of the plate coincides with the air-water interface. Therefore, during the acceleration of the plate, the formation of a closed vortex ring, as found in the deep water case h = 100 mm, is prevented. Instead, a U-shaped starting vortex is formed, of which the free ends attach to the air-water interface and produce strong depressions in the interface; see figure 2.8d. A schematic side-by-side comparison of the vortices in the h = 0 and the h = 100 mm case is given in figure 2.9. During the transition phase the U-shaped vortex detaches and quickly loses strength, visible as the flattening of the bottom of the surface vortices, meaning that they are no longer connected to a strong vortex below; see figure 2.8e. Also it appears that the vortex cores are no longer strong enough to capture the hydrogen bubbles in a well-defined core. The shifting away of the surface vortices as well as the break-up of the U-shaped vortex continues until a steady-phase wake similar to that of the deep water case is formed, except that in the case of h = 0 mm the wake is limited by the free surface, effectively cutting off part of the wake; see figure 2.8f.

In the h = 20 mm case, i.e. the case with maximum drag during the steady phase, the flow behaviour is a mixture of features observed in the flows for the deep water (h = 100 mm) and surface case (h = 0 mm). During the acceleration phase both a vortex ring and vortices connected to the air-water interface are formed; see figure 2.8g. During

[1] https://www.cambridge.org/core/journals/journal-of-fluid-mechanics/article/drag-force-on-an-accelerating-submerged-plate/EB6F8190B82EF385B98BFA5D70C3EB10

the transition phase the surface vortices shed more quickly than in the h = 0 mm case, deforming the vortex ring in streamwise direction; see figure 2.8h. After the vortex ring disintegrates a steady wake is formed similar to that of the h = 0 mm case. However, the gap between the top of the plate and the air-water interface causes a flow over the plate creating a large circulation zone closely trailing the plate as indicated in figure 2.8i. This creates a low pressure region on the wake-side of the plate explaining the maximum drag during the steady phase found for this case.

2.3.6. LARGE FLOW STRUCTURES

Figure 2.5 shows that the maximum drag is reached at the end of the acceleration phase for all three cases. During the acceleration phase the drag is mainly due to acceleration of the plate mass m_p and the hydrodynamic mass m_h. One would expect the plate deepest submerged to entrain most water and therefore to have the largest hydrodynamic mass. However, it is clear that both the h = 0 mm and the h = 20 mm cases have a higher initial peak. This is caused by the observed strong surface vortices formed in these two cases, resulting in strong low pressure zones close to the plate, and thus creating a larger drag. One more difference is the observed peaks 1 and 2 in the drag force signal for the h = 100 mm case, which are not observed in the force signals for the h = 0 mm and h = 20 mm cases. It is observed that in the case of h = 100 mm several large vortical structures are formed and shed during the transition phase, instead of just the formation of a starting vortex. The structures are of similar size and shape as the starting vortex, although less defined, and their creation and shedding coincides with peaks 1 and 2.

Coming back to the observed trend break at h = 50 mm in figure 2.4, we speculate that at this depth two drag enhancing mechanisms play a role as stated in section 2.3.3. Firstly, a circulation zone is formed close to the plate, as is discussed in section 2.3.5. This circulation zone increasingly enhances plate drag from h = 0 mm to h = 20 mm where this effect reaches its maximum. We further speculate that as the gap between the top of the plate and the free surface increases, from h = 20 mm to h = 50 mm, the circulation zone weakens and consequently the plate drag decreases. The second drag enhancing mechanism is the growth of the wake size, i.e. the wake height, with increasing plate depth. Since the separation points on the flat plate are well-defined due to the sharp edges of the plate, unlike e.g. the separation points on a cylinder which vary with Reynolds number [41], the drag on the flat plate and the wake size of the flat plate, i.e. the wake height, are positively correlated. At larger plate depths a smaller part of the wake is clipped by the free surface, and consequently, a larger mass of water is entrained in the plate wake thus increasing the plate drag. Figure 2.4 indicates that the drag during the steady phase for the h = 0 mm case is significantly lower than that for the deep water case (h = 100 mm). The wake size of the surface case (h = 0 mm), is only about 75% of the size of the deep water case (h = 100 mm); see figure 2.8c and 2.8f. The ratio of drag coefficients $C_{D0mm}/C_{D100mm} \approx 0.8$ reflects the ratio of the wake sizes in vertical direction (≈ 0.75), which is in accordance with our hypothesis that drag and wake size are positively correlated. Finally, in figure 2.4 a local maximum at h = 100 mm can be seen, although less pronounced than the maximum at h = 20 mm. We hypothesise that this local maximum or trend break is caused by weakening interactions between the plate wake and the free surface.

In the next sections (2.3.7 and 2.3.8) the instantaneous force signal during the accel-

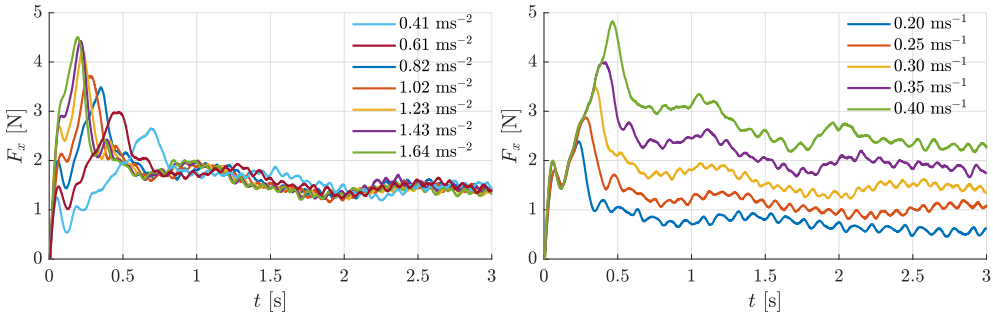

(a) (b)

Figure 2.10: Drag force signals $F_x(t)$ measured at plate depth h=100 mm. (a) $F_x(t)$ for various accelerations towards a fixed plate velocity $V = 0.30$ ms^{-1}. (b) $F_x(t)$ for a fixed acceleration of $a = 0.82$ ms^{-2} towards various plate velocities V.

eration and transition phase is discussed. For a further analysis of the large structures on the basis of PIV measurements we refer the reader to section 2.3.9 and 2.3.10.

2.3.7. ALTERNATIVE MODELLING OF THE HYDRODYNAMIC MASS

As observed in the flow visualisations the entrained mass in the wake of the plate during the acceleration phase is not constant, but grows larger over time, and so does the plate drag force. This suggests an increasing hydrodynamic mass m_h over time, instead of a constant hydrodynamic mass as suggested by Patton [29] and Yu [43]. Moreover, due to the acceleration strong vortices are formed close to the plate that increase the drag on the plate even further through their pressure fields. To investigate the variation of the hydrodynamic mass over time, experiments are carried out for different combinations of plate velocity, acceleration, and plate depth. Each combination of velocity (V = 0.20, 0.25, 0.30, 0.35, 0.40 ms^{-1}) and acceleration (a = 0.41, 0.62, 0.82, 1.02 1.23, 1.44, 1.64 ms^{-2}) is tested for each depth (h = 0, 20, 100 mm) resulting in 105 measurements. Figure 2.10 shows the effects of variations in acceleration a and target velocity V on the drag force F_x as function of time; note that from here on, all force signals are filtered to improve readability using a second order Savitzky-Golay filter with a 0.1 s window. During the steady phase the plate drag scales with $F_x \sim V^2$ as is expected from equation 2.3; see figure 2.10b. However, during the acceleration phase, the plate drag appears to increase linearly with time $F_x \sim t$ which for constant acceleration is identical to $F_x \sim V$ (figure 2.10b), and is not in agreement with equation 2.3. Also, the increase of the plate drag with respect to time, i.e. the rate of change dF/dt, appears to scale with acceleration $dF_x/dt \sim a$; see figure 2.10a.

To investigate the increase in force with time during the acceleration phase, the common force decomposition (equation 2.3), is rewritten such that a residual force due to the acceleration of the hydrodynamic mass m_h is defined:

$$F_{mh} = F_x - \underbrace{m_p a(t)}_{F_{mp}} - \underbrace{\frac{1}{2}\rho V(t)^2 C_D A}_{F_{CD}}, \tag{2.7}$$

This modelling choice effectively isolates the increase in drag due to unsteady effects. For small movements starting from rest, the residual force F_{mh} matches the product of the acceleration a and the hydrodynamic mass m_h from equation 2.5 as proposed by Yu [43]; see the markers in figure 2.11a. Note that a small offset in time, equal to $t_{sr} = 0.07$ s, takes into account the step response. Since the behaviour of the force signal during the acceleration phase is independent of the target velocity V (figure 2.10b), we use the measurements with the highest target velocity of $V = 0.40$ ms^{-1} to fit a model, as these data contain the longest acceleration time. Figure 2.11a shows linear fits through the theoretical added mass as proposed by Yu [43], with a fit for each signal defined as:

$$F_{mh} = \frac{dF_{mh}}{dt}(t - t_{sr}) + m_{h(Yu)}a, \tag{2.8}$$

where the only free fitting parameter is the rate of change of the residual force dF_{mh}/dt. In figure 2.11b all found rates of change of force dF/dt are plotted as function of acceleration a. The markers show the values of dF/dt for different accelerations for the three selected depths, while the lines indicate the clear linear behaviour of dF/dt with respect to acceleration. To give a physical interpretation to this, it is assumed that the residual force F_{mh} during the acceleration phase is due to the acceleration of the hydrodynamic mass in the wake of the plate. Note that this assumption does not necessarily capture the intricate phenomena of the formation of the ring vortex or the subsequent deformation of the free surface, which possibly increase the plate drag via other mechanisms than entrainment. However, this assumption does enable us to model the increased plate drag in a simple and convenient manner. We define the residual force as:

$$F_{mh} = m_h a, \tag{2.9}$$

where the hydrodynamic mass m_h is time dependent since the acceleration a is constant for each measurement, while F_{mh} is increasing in time. This leads to the definition of the entrainment rate of mass in the wake of the plate:

$$\frac{dm_h}{dt} = \frac{1}{a}\frac{dF_{mh}}{dt}, \tag{2.10}$$

shown as a function of the acceleration a in figure 2.11c. When the plate is at the free surface ($h = 0$ mm) the entrainment rate dm_h/dt is strongly increased when compared to the deeper immersed plates; at lower accelerations this almost doubles. Also, we show that for all three selected plate depths the entrainment rate is gradually increasing with acceleration up to $a \approx 1$ ms^{-2}, while for higher accelerations the entrainment rate has a constant value. At a higher entrainment rate the wake grows more rapidly over time thus faster increasing the plate drag force. The maximum force experienced by the plate during uniform acceleration is the sum of the steady phase drag force F_{CD} and the residual force F_{mh}, which are both dependent on immersion depth h as shown in figure 2.4 and 2.11c, respectively. The maximum force achieved at some depth h is then dependent on the set target velocity V and acceleration a. Apparently a trade-off exists between steady phase drag and entrainment, e.g. the case $h = 0$ mm has the lowest steady phase drag coefficient but has the highest entrainment rate.

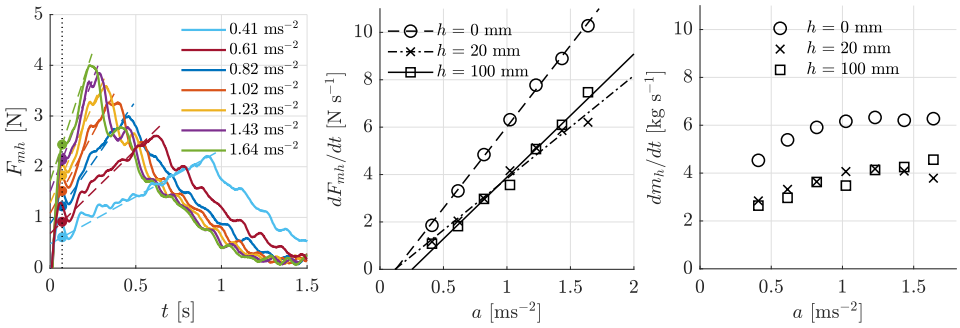

(a) (b) (c)

Figure 2.11: (a) The solid line represents the residual force F_{mh} as function of time (t) for different accelerations towards a fixed plate velocity V = 0.40 ms^{-1} at plate depth h = 0 mm. The markers represent the force due to hydrodynamic mass as proposed by Yu [43]. The dashed line represents a linear fit through the force signal $F_{mh}(t)$ during the acceleration phase. The vertical dotted line marks the time offset t_{sr} to account for the step response. (b) The rate of change of force dF/dt as function of the accelerations a for the selected plate depths. (c) The entrainment rate dm_h/dt as function of acceleration a for the three selected plate depths.

2.3.8. FORCE DURING THE TRANSITION PHASE

Figure 2.11a shows that the residual force F_{mh} does not vanish immediately after the plate reaches its target velocity (i.e. when a reaches 0 ms^{-2}), although this would be expected from the general definition; see equation 2.9. Instead, the force F_{mh} appears to drop sharply to a non-zero value and then gradually decays to zero, after which the total force F_x equals the steady phase drag force F_{CD}. The force which vanishes immediately upon a reaching 0 we call a 'force due to added mass', since it relates to the acceleration of the plate. The gradually decreasing force we call a 'history force', which is due to the developing wake caused by the past acceleration of the plate, which exists long after the plate reaches its target velocity. This is analogues to the virtual mass force for a spherical particle: $F = \frac{\rho_c V_p}{2}\left(\frac{D\vec{u}}{Dt} - \frac{d\vec{v}}{dt}\right)$ [11], where $\frac{\rho_c V_p}{2}$ is the displaced fluid mass, $\frac{d\vec{v}}{dt}$ the particle acceleration (added mass term), and $\frac{D\vec{u}}{Dt}$ the material derivative of the fluid (history term).

We assume that the plate reaches the constant target velocity at time t_c and location x_c. As discussed in section 2.3.5 the acceleration and transition phase are dominated by the formation and shedding of vortices. As discussed in section 2.1.3, a suitable dimensionless time to describe these flow phenomena is t^*, i.e. the 'formation time', defined as

$$t^* = \frac{1}{l_b}\int_0^t V(\tau)d\tau, \tag{2.11}$$

where $V(t)$ is the instantaneous velocity at time t, and l_b a characteristic length, which here is chosen to be the plate height. The non-dimensional time t^* is then effectively the number of plate heights travelled, which is identical to the non-dimensional time used in the simulations by Koumoutsakos & Shiels [21].

Figure 2.12 shows the drag force signal as a function of the post-acceleration formation time $t^* - t_c^*$ during the early transition phase for a plate depth h = 100 mm and a velocity V = 0.30 ms^{-1}. Note that t^* at constant velocity linearly increases with dimensional time t.

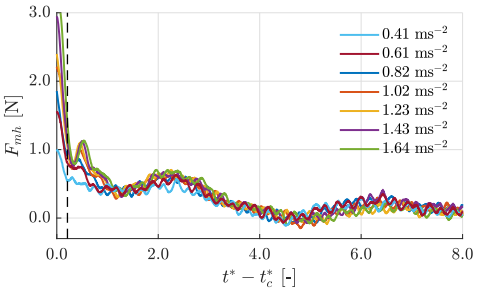

(a) Residual force as function of post-acceleration formation time for h = 100 mm, velocity V = 0.30 ms^{-1}, and varying accelerations.

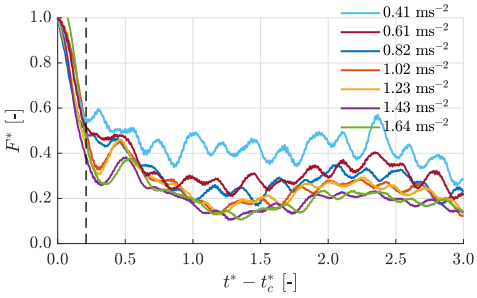

(b) Normalised residual force as function of post-acceleration formation time for h = 100 mm, velocity V = 0.30 ms^{-1}, and varying accelerations.

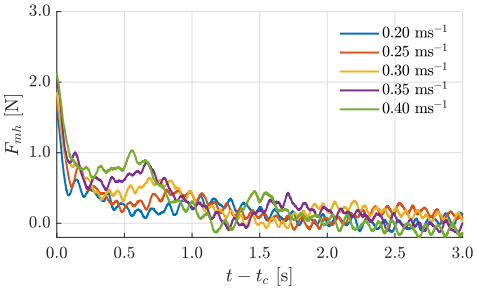

(c) Residual force as function of post-acceleration time for h = 100 mm, acceleration a = 0.82 ms^{-2}, and varying velocities.

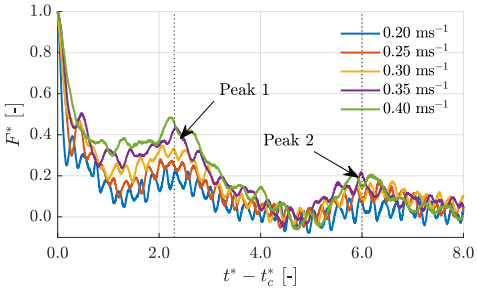

(d) Normalised residual force as function of post-acceleration formation time for h = 100 mm, acceleration a = 0.82 ms^{-2} and varying velocities.

Figure 2.12: The residual force in dimensional form F_{mh} (left) and non-dimensional form F^* (right) as function of the post-acceleration time $t - t_c$ or formation time $t^* - t_c^*$ for different accelerations towards a fixed plate velocity V = 0.30 ms^{-1} (top figures) or towards different velocities at a fixed acceleration a = 0.82 ms^{-2} (bottom figures) for plate depth h = 100 mm. In (a) and (b) the dashed line indicates the dimensionless step response time t_{sr}^*. In (d) the dotted lines indicate the location of peak 1 and peak 2 which for different velocities coalesce in non-dimensional time.

As shown in figure 2.12a the force signals F_{mh} quickly decrease when the acceleration ends and converge after $t^* - t_c^* \approx 1$, i.e. when the plate has travelled at constant velocity V over a distance of a single plate height l_b. This implies that the varying accelerations at which the plate accelerated to its target velocity do not cause lasting effects in the flow beyond the travelled distance of a single plate height l_b. Next, we introduce the normalised force F^* defined as

$$F^* = \frac{F_{mh}}{F_{mh}(t_c)}, \tag{2.12}$$

where the residual force F_{mh} is normalised by its maximum value at time t_c. In figure 2.12b it can be seen that the normalised force F^* immediately after the acceleration ends, thus within the step response time of the force signal due to the abrupt change in force on the plate (indicated by the dashed line), has decreased by 50% to 70%. The initial decrease appears to scale with acceleration, i.e. force signals based on a higher acceleration have a larger initial decrease, while for lower acceleration the initial decrease is smaller. This implies that the added mass force is more dominant for higher accelerations, while for lower accelerations F_{mh} is more like a history force.

The force F_{mh} as a function of $t - t_c$ does not converge for different velocities when a remains constant (see figure 2.12c). The normalised force F^* as a function of $t^* - t_c^*$ does not converge for different velocities either, but the low-frequency peaks, indicated as peak 1 and peak 2, now nicely align in dimensionless time (see figure 2.12d). Those peaks are associated with the formation and shedding of large vortical structures in the wake, see section 2.3.6. It appears that the formation time t^*, as proposed by Gharib *et al.* [15] and applied to a vortex ring generated by a jet, also is a universal time scale for the development of the vortical structures in the wake of the plate. Also, the lower velocities show a larger initial decrease than the higher velocities, indicating that for lower velocities the residual force F_{mh} acts more like a force due to added mass than like a history force.

Figure 2.13a shows that also for the case of $h = 0$ mm for different accelerations towards a fixed plate velocity of $V = 0.30$ ms^{-1}, the force signals converge after the plate has travelled at constant velocity over a distance of a few plate heights, i.e. the plate drag force is no longer affected by the initial acceleration by which the plate reached its target velocity. However, when considering the normalised force F^* for the case $h = 0$ mm, shown in figure 2.13b, it is obvious that the initial decrease, i.e. the decrease within the step response time t_{sr}^*, is much smaller than for the case of $h = 100$ mm (see figure 2.12b); 20-40% for $h = 0$ mm, compared to 50-70% for $h = 100$ mm. This indicates that the effect of added mass is far less pronounced for the surface case ($h = 0$ mm) than it is for the deeper immersed plate ($h = 100$ mm) and that the residual force F_{mh} for $h = 0$ mm acts more like a history force than a force due to added mass. Despite the difference in the initial decrease of the residual force and the absence of peak 1 and peak 2 in the force signal for the case of $h = 0$ mm, the force signal is similar to that of the $h = 100$ mm case with respect to changing acceleration: the relative initial decrease is proportional to acceleration.

Figure 2.13 shows the change in force signals during the transition phase for different velocities and a fixed acceleration of $a = 0.82$ ms^{-2} for the case $h = 0$ mm. Comparison of figures 2.13b and 2.12b shows that the initial decrease for all velocities is again smaller for the case of $h = 0$ mm than for the deeper immersed plate $h = 100$ mm. However, in each case the initial decrease is largest for the smallest velocity and becomes smaller with

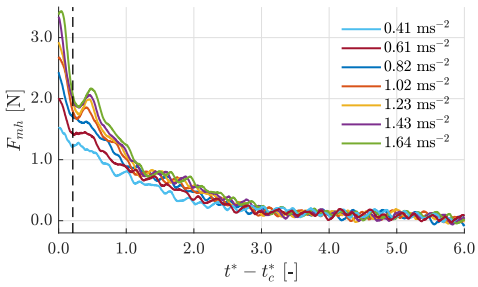

(a) Residual force as function of post-acceleration formation time for h = 0 mm, velocity V = 0.30 ms^{-1}, and varying accelerations.

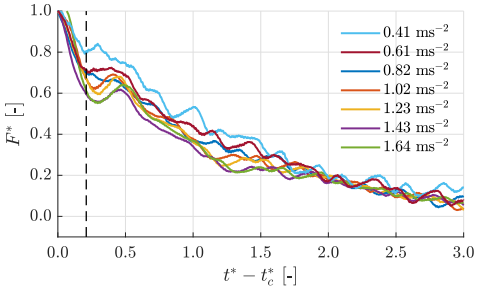

(b) Normalised residual force as function of post-acceleration formation time for h = 0 mm, velocity V = 0.30 ms^{-1}, and varying accelerations.

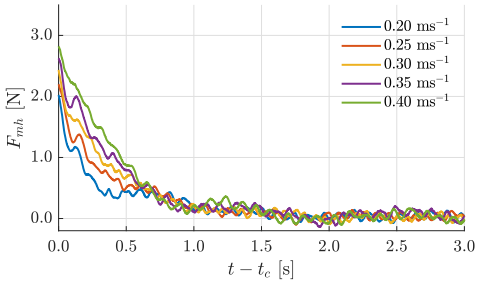

(c) Residual force as function of post-acceleration time for h = 0 mm, acceleration a = 0.82 ms^{-2}, and varying velocities.

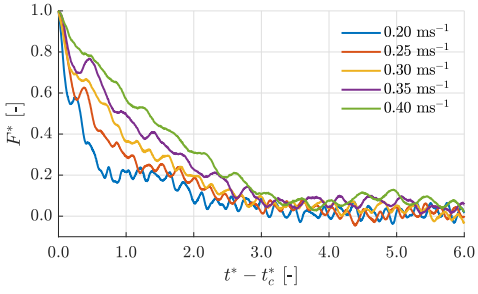

(d) Normalised residual force as function of post-acceleration formation time for h = 0 mm, acceleration a = 0.82 ms^{-2} and varying velocities.

Figure 2.13: The residual force in dimensional form F_{mh} (left) or non-dimensional form F^* (right) as function of the post-acceleration time $t - t_c$ or formation time $t^* - t_c^*$ for different accelerations towards a fixed plate velocity V = 0.30 ms^{-1} (top figures) or towards different velocities at a fixed acceleration a = 0.82 ms^{-2} (bottom figures) for plate depth h = 0 mm. In (a) and (b) the dashed line indicates the dimensionless step response time t_{sr}^*.

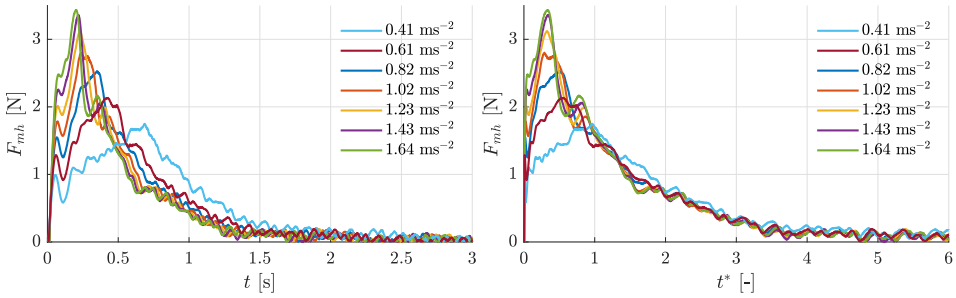

(a) (b)

Figure 2.14: Force versus time t and the formation time t^* for varying accelerations towards $V = 0.30$ ms^{-1} at depth $h = 0$ mm. (a) Dimensional time t. (b) Formation time t^*.

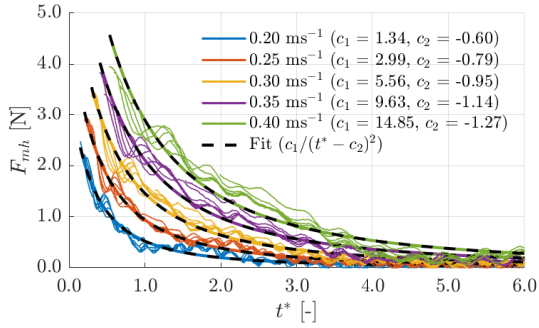

Figure 2.15: Force signal F_{mh} versus formation time t^* during the transition phase for different accelerations towards different velocities (solid lines). Fits of the form $c_1/(t^* - c_2)^2$ through each set of force signals corresponding to a single velocity (dashed lines).

increasing velocity. Contrary to the deeper immersed plate $h = 100$ mm, the force signal of the $h = 0$ mm case shows no peaks during its decrease in magnitude from acceleration phase to steady phase. Not unexpectedly due to the absence of characteristic features during the transition phase, introducing the formation time t^* does not seem to better align the force signals in time during the transition phase.

When considering the force-time signal of the entire run at a depth of $h = 0$ mm for different accelerations towards a target velocity of $V = 0.30$ ms^{-1}, shown in figure 2.14a, we see that the signals do not converge until $t = 1.5$ s. However, when introducing the formation time t^* we clearly see that all force signals collapse on a single curve during the transition phase; see figure 2.14b. Different target velocities each appear to have their own unique curve to which force signals from different accelerations collapse, as shown in figure 2.15. The curve to which all signals collapse are of the form $c_1/(x - c_2)^2$ with c_1 and c_2 increasing with increasing target velocity V. The fitting coefficients are shown in the legend of figure 2.15. The shapes of these curves appear to be determined in full by the target velocity. The formation number from which a force signal starts following this curve depends on the acceleration only. We consider a scaling argument to interpret the

behaviour of the force signal by $1 \sim 1/x^2$. From the definition of the formation time t^*, equation 2.11, it is obvious that t^* is identical to the plate travel distance $x(t)$ expressed in the number of plate heights l_b. The flow visualisation showed that the acceleration phase is dominated by the generation of a large starting vortex which is shed upon reaching the target velocity; see section 2.3.5. Let U be the flow velocity of such an irrotational vortex that scales with the inverse of the distance to this vortex $U \sim 1/x$. Since dynamic pressure q scales with velocity squared $q \sim U^2$ we can state that the dynamic pressure at the wake-side of the plate due to the shed vortex scales with $q \sim 1/x^2$. For the sake of simplicity we assume that we can use Bernoulli's principle for incompressible irrotational flow such that the total pressure P is constant throughout the flow, i.e. $P = p + q$. We state that the static pressure p increases over plate travel distance as q decreases by $\sim 1/x^2$. Since the plate drag force is the difference in static pressure over the plate, an increase in static pressure at the wake-side of the plate implies a decrease in drag force on the plate. This scaling argument matches the observed behaviour $F_{mh} \sim 1/x^2$.

2.3.9. VORTICITY

The flow field was analysed using PIV to provide a quantitative insight and to reveal the more intricate structures in the flow that were not captured by the visualisations. Although the flow is highly three-dimensional, as is evident from figure 2.8, two-component planar PIV still reveals interesting differences, and similarities, between the three selected cases $h = 0$, 20, and 100 mm.

The PIV measurements are done in the horizontal mid-plane of the plate for all three selected plate depths $h = 0$, 20, and 100 mm, at an acceleration of $a = 0.82$ ms^{-1}, and a target plate velocity $V = 0.30$ ms^{-1}. The chosen parameters correspond with the three force measurement results shown in figure 2.5 and discussed in section 2.3.3. The PIV results are represented through the vorticity ω_z based on the local flow circulation by an 8-point estimation [26]. A discrete representation is used [1] since it allows for different spacing between vectors in the x- and y-direction. In the here presented results the dimensionless vorticity

$$\omega_z^* = \frac{\omega_z l_b}{V} \tag{2.13}$$

is used, similar to Ringuette *et al.* [33]. The locations x and y are made dimensionless by l_b resulting in x^* and y^*, respectively, such that the plate location x^* is identical to the formation time t^*, i.e. $x^*(t^*) = t^*$. The order of presentation of the different depths is the same as in the results of the flow visualisation in section 2.3.5, i.e. $h = 100$ mm, followed by $h = 0$ mm, and $h = 20$ mm.

Figure 2.16 shows the vorticity ω_z^* for all three selected depths for different times t, including the instances in time corresponding to those of the flow visualisations in figure 2.8. Note that a movie of the time evolution of all three cases, side-by-side, is available in the supplemental material (movie4). For all three cases the formation of a vortex pair during the acceleration phase, i.e. up to $t = 0.35$ s appears very similar and matches to the cross-section of the vortex ring at the mid-plane of the plate, as shown in figures 2.8a, 2.8d, and 2.8g.

When the plate approaches $x^* = 2$ at $t = 0.80$ s the wakes start to differ. The vortex pair of the case $h = 100$ mm is still very close and concentrated to the mid-plane of the plate,

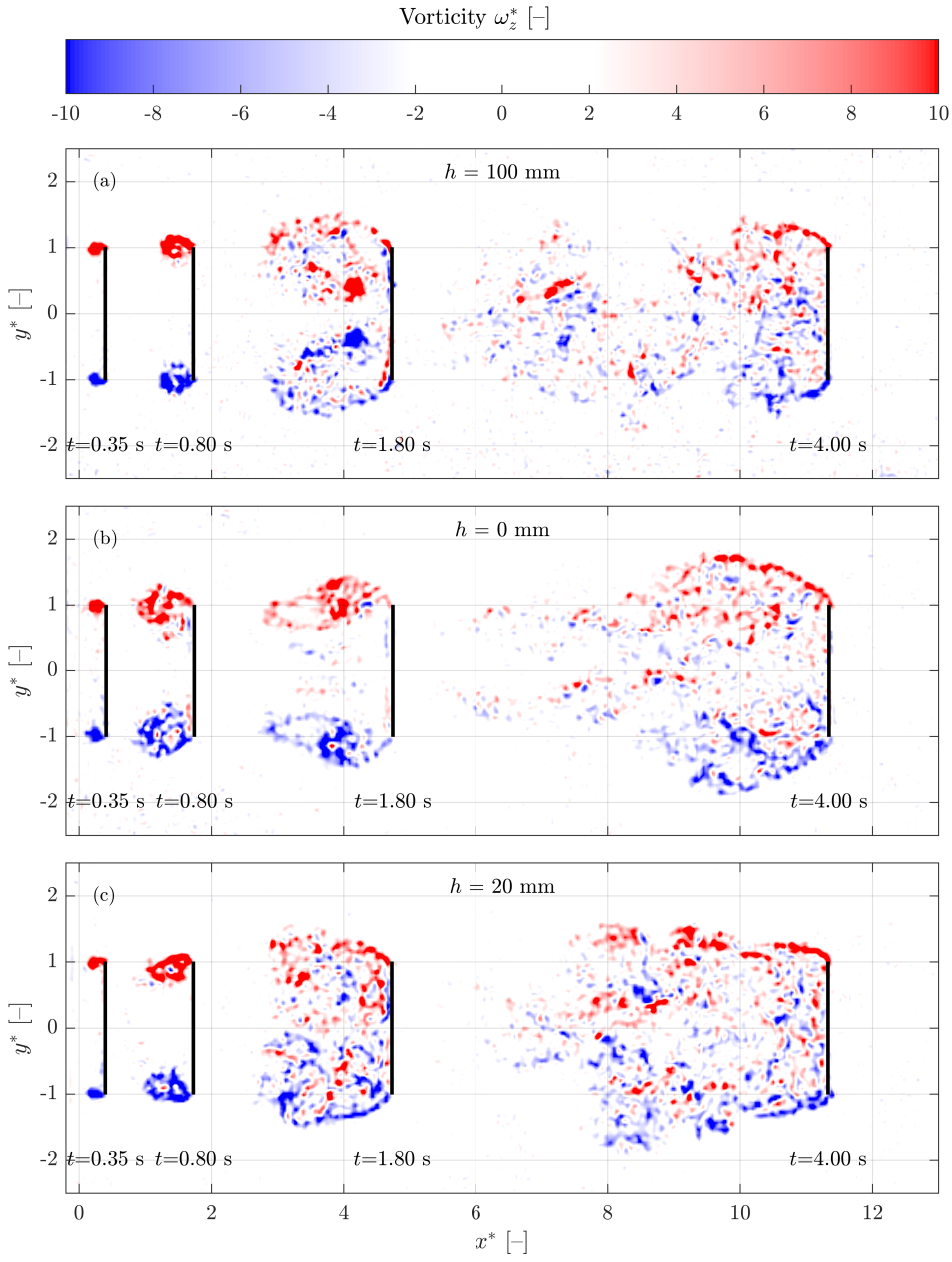

Figure 2.16: (Horizontal plane at plate half-height) Dimensionless vorticity ω_z^* for different instances in time t at the three selected depths (a) h = 100 mm, (b) h = 0 mm, and (c) 20 mm. The plate location x^* matches the formation time t^*, i.e. $x^*(t^*) = t^*$.

as is also seen in figure 2.8b, while in both cases $h = 0$ and $h = 20$ mm the vortices start to travel away from the plate and become less defined. This matches the behaviour shown in figure 2.8e and 2.8h.

For $t^* > 4$ at $t = 1.80$ s, i.e. well in the transition phase, each wake becomes very distinct. The vortices in the case of $h = 100$ mm are still attached to the plate, but have moved inwards, i.e. the vortex ring has contracted in the y-direction, and two large circulation zones around the vortex pair are formed in which the secondary vortices formed in the shear layer are shed. During this contraction process the two highly concentrated circulation zones move from the plate edge towards the centre of the plate creating a strong and large low pressure zone. We speculate that this is associated with a characteristic peak in the drag force at $t^* = 2.8$, e.g. shown as peak 1 in figure 2.12d. At the same plate depth h = 100 mm, some time after the situation at $t = 1.80$ s shown in figure 2.16, the two well-defined vortices trailing closely behind the centre of the plate touch and collapse which may be associated with a second peak in the drag force signal, e.g. shown as peak 2 in figure 2.12d. In the other two cases the circulation zones are not so concentrated. The large circulation zones in the case of $h = 0$ mm stretch in streamwise direction and detach, while the circulation zones in the case of $h = 20$ mm already disintegrate into a chaotic wake.

Well into the steady phase, i.e. at $t = 4.00$ s where the plate passes $x^* = 11.5$, the wakes also look very distinct. The case of $h = 100$ mm shows an asymmetric wake with what appears to be an oscillating tail, which is a well-known phenomenon for steady flow over a plate [13, 16]. The cases $h = 0$ mm and $h = 20$ mm both show a symmetric wake of similar size, but the latter has a large amount of vorticity very close to the plate which, we conjecture, (partially) explains the maximum steady phase drag C_D found for this plate depth ($h = 20$ mm), see figure 2.4. Also, we note the difference in wake angle. Whereas the wake angles in the vertical plane are quite similar, clearly visible in the visualisation (figure 2.8), the wake angles in the horizontal plane differ substantially. It appears that the case with the highest drag ($h = 20$ mm) has the smallest wake angle, while the case with the lowest drag ($h = 0$ mm) has the largest wake angle, see figure 2.16.

To test the reproducibility of the PIV measurements, the experiments were performed three times for each plate depth h. The realisations at the same depth are highly reproducible. Only at a plate depth of $h = 100$ mm around $t = 4.00$ s a clear difference between realisations is found, as shown in figure 2.17. The two different realisations are very similar except that the tail of the wake of the realisation shown in the top figure sweeps up, while in the figure at the bottom the tail sweeps down. A sweeping tail which starts in an arbitrary direction shows that this is not due to imperfections in the experimental set-up.

2.3.10. CIRCULATION AND SHEDDING EVENTS

In previous studies [15, 33] the total circulation Γ was used to identify vortex shedding events. The total circulation is obtained by integrating the local vorticity over a surface, i.e.

$$\Gamma = \int_S \omega_z dS. \tag{2.14}$$

The dimensionless circulation Γ^* is obtained by integration of ω_z^* (defined in equation 2.13) over the dimensionless flow field area S formed by the entire range of x^* and y^*. Kelvin's circulation theorem states that integration over S should yield a net circulation

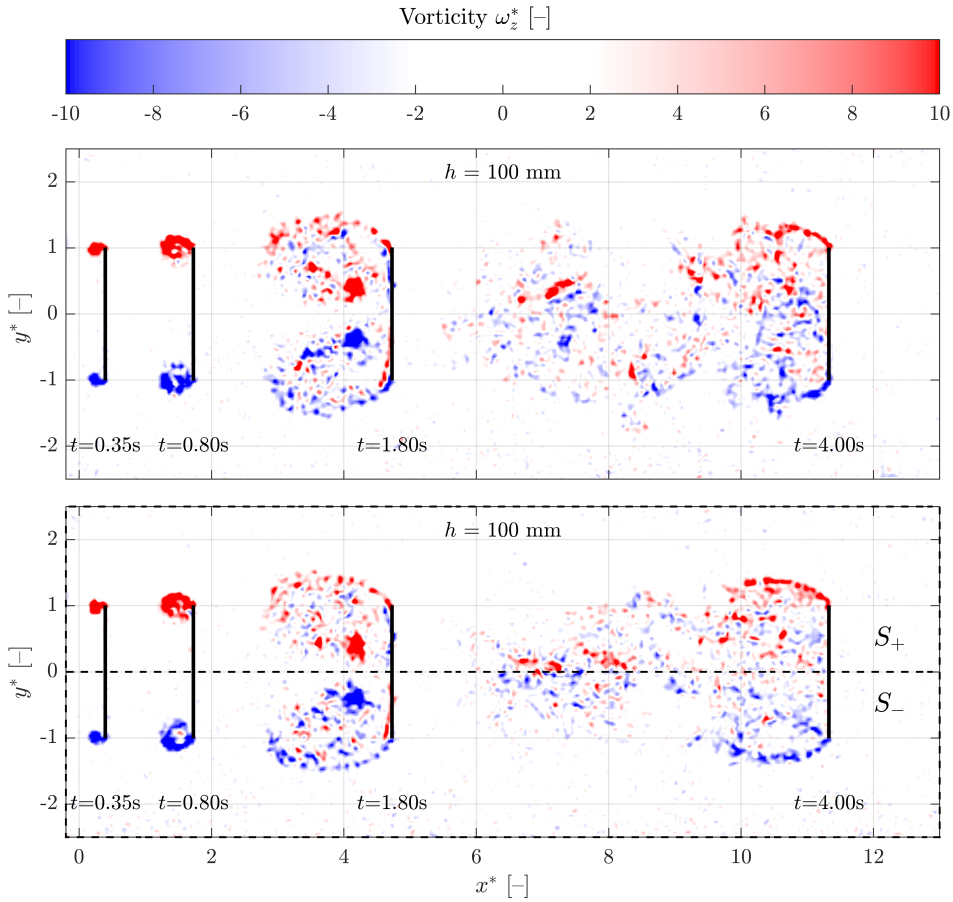

Figure 2.17: (Horizontal plane at plate half-height) Dimensionless vorticity ω_z^* for different instances in time t at a selected depth of h = 100 mm. The flow behaviour appears to be very similar for both realisations. Only in the steady phase t = 4.00 s the tail of the wake sweeps up in one realisation (top figure) and down in the other (bottom figure) which matches the characteristic oscillating wake as was already observed by Fage & Johansen [13]. The dashed line around the outer border shows the area of integration S for which the circulation is obtained. The symmetry line through y^* = 0 is also marked and shows the dividing line between integration surfaces S_- and S_+.

of $\Gamma^* = 0$ if the integration boundary is along a material contour [8] as long as the flow is symmetric, i.e. produces no lift. The flow conditions for the theorem to hold, i.e. inviscid and barotropic flow, are fulfilled by choosing the material contour along the boundaries of the field of view of the PIV measurements, where the flow is at rest, indicated by the dashed line along the outer border in figure 2.17 (bottom).

The grey lines in figure 2.18 show the circulation Γ^* as function of the formation time t^* for $h = 100$, 0, and 20 mm, respectively. For all three plate depths, throughout each realisation, the total circulation Γ^* is very close to zero. However, at the intervals $4.8 < t^* < 6$ and $t^* > 9.4$ the measured circulation Γ^* does not appear to be conserved perfectly. This deviation between measurements and theory is explained by measurement errors (random noise). The non-zero total circulation based on S coincides with the stitching seams of the flow field as indicated by the dashed vertical lines in figure 2.18, showing that the flow field is not stitched seamlessly. In the case of $h = 20$ mm the trailing vortex, as shown in figure 2.8i, might cause large out of plane motion which also affects the measurement accuracy [1].

As was noted before, the flow field maintains symmetrical well into the steady phase. To quantify this symmetry and to identify vortex shedding events, the flow field area S is subdivided into two areas along the symmetry plane of the plate, S_- and S_+, corresponding to $y^* < 0$ and $y^* > 0$, respectively (figure 2.17 bottom). Integration of the vorticity over each area results in the total circulation Γ^* of each region, as shown in figure 2.18. Throughout all runs, i.e. for all cases and each realisation, the circulation is $\Gamma^* > 0$ for area S_+ and $\Gamma^* < 0$ for area S_-. Clearly, for $t^* < 4.8$ all cases behave very similar with virtually no difference between realisations.

The ability of the total circulation Γ^* to identify vortex shedding becomes clear at $6 < t^* < 8$ for the case $h = 100$ mm, where a temporary decrease in circulation occurs due to the two touching vortices as described in 2.3.9. The same mechanism is described by Ringuette *et al.* [33] as an 'inward' pinch-off. They obtained a circulation profile with 'inward' pinch-off occurring at $t^* \approx 4$ where in this study the pinch-off occurs at $t^* \approx 6$. Their circulation profile is very similar in shape compared to the one presented here, even though the plate in their work pierces the surface and has different dimensions, i.e. $l_a = 0.127$ m and height $l_b = 0.0635$ m. In the case of $h = 20$ mm an ordinary pinch-off occurs at $t^* = 8$, identified by an interval of constant total circulation [15]. For the case of $h = 0$ mm shedding events were neither observed in the vorticity field, nor are indications of those events present in the measured circulation.

Apart from identifying shedding events, the total circulation in S^- and S^+ in figure 2.18 quantitatively show that the experiments are well reproducible, although the circulation increasingly deviates for larger times t^*. This deviation is smallest for the case $h = 0$ mm, which suggests that the free surface suppresses this deviation.

2.4. DISCUSSION AND CONCLUSION

In this study the flow around plates accelerating at a towards a fixed plate velocity V at various submerged depths h are investigated using measurement techniques that complement each other. The drag force on the plate as function of time is measured, the three-dimensional flow around the plate is visualised using hydrogen bubble flow visualisation, and the two-dimensional flow field in the horizontal mid-plane of the plate is

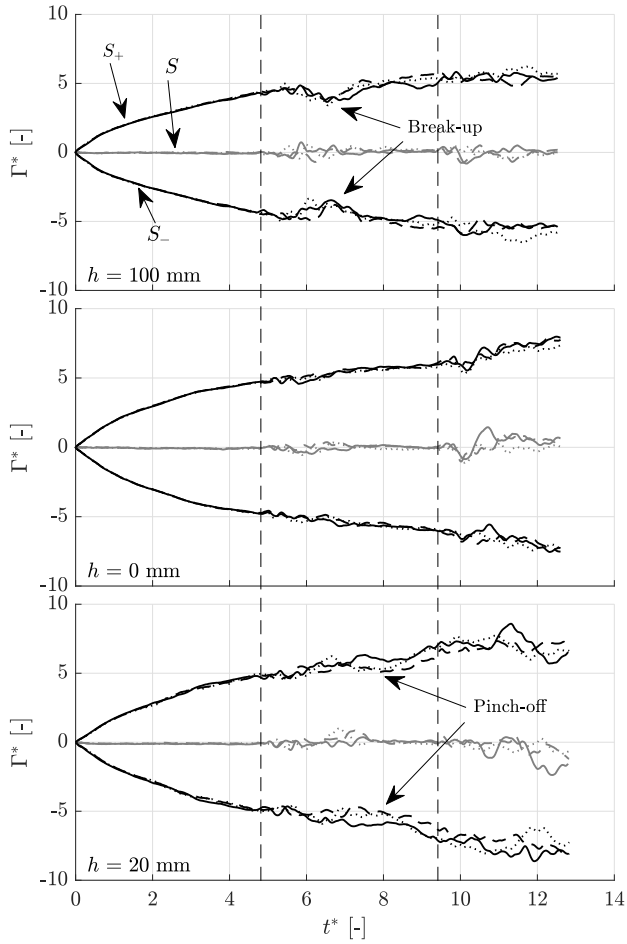

Figure 2.18: The grey lines show the circulation Γ^* as function of formation time t^* based on the total flow field S, while the black lines show the circulation Γ^* based on the top half area S_+ and bottom half area S_- as indicated in the figure. The three different realisations at each depth are represented by different line styles. A break-up event in the case $h = 100$ mm is clearly visible around $t^* = 7$, as is a pinch-off event around $t^* = 8$ in the case $h = 20$ mm. The vertical dashed lines show the stitching seams of the flow field.

measured quantitatively using PIV from which the vorticity ω_z and total circulation Γ are derived.

The steady phase drag coefficient is found to have a remarkable peak at a plate depth of $h = 20$ mm, i.e. 45% higher than the drag at the surface ($h = 0$ mm) and 20% higher than when the plate is submerged one plate height $h = 100$ mm ($h/l_b = 1$). The definition of the steady phase $t > 3.4$ s ($t^* > 10$) based on the measured force signals matches with the flow visualisations (figure 2.8, and as movies available in the supplemental material as movie1, movie2, and movie3) and the vorticity fields (figure 2.16, supplemental material movie4). The drag force during the acceleration phase appears to be very complex but is shown to be well behaved:

$$F_x(t) = \underbrace{m_p a(t)}_{F_{mp}} + \underbrace{\frac{1}{2}\rho V(t)^2 C_D A}_{F_{CD}} + \underbrace{\frac{dm_h}{dt} a(t)(t - t_{sr}) + m_{h(Yu)} a}_{F_{mh}}. \tag{2.15}$$

We showed that the force due to added mass F_{mh} is constant for small t^* and matches results reported by Yu [43]. For t^* the expression is expanded based on an entrainment rate $\frac{dm_h}{dt}$ that models an increasing mass in the wake of the plate. This entrainment rate appears to be independent of velocity and almost constant for different accelerations a. We conclude that the entrainment rate is an important parameter to predict maximum hydrodynamic forces on plate-like geometries and that the entrainment rate is strongly enhanced by the vicinity of a free surface; at the surface, for a plate depth of $h = 0$ mm, the entrainment rate is found to be 50% larger than for plate depths of $h = 20$ and $h = 100$ mm. During the transition phase the force decreases for the case of $h = 100$ mm along a distinct profile with two large peaks, peak 1 and peak 2. These are associated with vortex shedding events visible in both the visualisations, the vorticity field, and the circulation profiles. For different velocities these peaks perfectly align in time by use of the formation time t^*, as shown in figure 2.12d. Also, the force due to hydrodynamic mass during the transition phase appears to scale with the formation time as $F_{mh} \sim 1/t^{*2}$, where t^* is essentially the distance travelled by the plate. This scaling is hypothesised to be due to the plate moving away from the shed starting vortex. A scaling argument supports this hypothesis and in the visualisations it is shown that a large vortex in the vertical plane is indeed shed.

The motivation for this study stems from (competitive) rowing. During rowing the oar blade moves along a complicated cycloid path not only producing drag, but also lift, making a comparison with an accelerating flat plate along a straight path somewhat complicated. However, during the start of a rowing match the oar blade accelerates from rest along a more linear path and travels ≈ 10 times the blade height before the next stroke ($t^* \approx 10$); very much like the flat plate in this study. It stands to reason that for a rowing oar blade an optimal depth exists, which is a trade-off between decreasing entrainment rate and increasing steady phase drag with increasing depth h. Also the starting technique where athletes use several short strokes to achieve cruising speed as fast as possible seems hydrodynamically advantageous. The drag on the plate is at its maximum while accelerating and up to the steady phase a history force is present. This means that while accelerating the plate and during the transition phase the generation of drag force is more efficient, i.e. the plate produces a higher force at an equal or lower velocity than in the steady phase. During the acceleration phase this effect is strongest, so with several short

strokes the oar blade spends a longer time in the acceleration phase and early transition phase, and would thus be more efficient.

ACKNOWLEDGEMENTS

This work is part of the research programme “Optimisation of propulsion in and over water" with project number 12868, which is (partly) financed by the Netherlands Organisation for Scientific Research (NWO).

REFERENCES

[1] ADRIAN, R. J. & WESTERWEEL, J. 2011 *Particle image velocimetry*. Cambridge University Press.

[2] BARRÉ, S. & KOBUS, J. M. 2010 Comparison between common models of forces on oar blades and forces measured by towing tank tests. *Proceedings of the Institution of Mechanical Engineers, Part P: Journal of Sports Engineering and Technology* **224** (1), 37–50.

[3] BEARMAN, P. W. 1971 An investigation of the forces on flat plates normal to a turbulent flow. *Journal of Fluid Mechanics* **46** (1), 177–198.

[4] BUSH, J. W. M. & HU, D. L. 2006 Walking on water: biolocomotion at the interface. *Annu. Rev. Fluid Mech.* **38**, 339–369.

[5] CAPLAN, N., COPPEL, A. & GARDNER, T. 2010 A review of propulsive mechanisms in rowing. *Proceedings of the Institution of Mechanical Engineers, Part P: Journal of Sports Engineering and Technology* **224** (1), 1–8.

[6] CAPLAN, N. & GARDNER, T. N. 2007 A fluid dynamic investigation of the Big Blade and Macon oar blade designs in rowing propulsion. *Journal of Sports Sciences* **25** (6), 643–650.

[7] CAPLAN, N. & GARDNER, T. N. 2007 Optimization of oar blade design for improved performance in rowing. *Journal of Sports Sciences* **25** (13), 1471–1478.

[8] COHEN, I. M. & KUNDU, P. K. 2007 *Fluid Mechanics*. Academic Press.

[9] COPPEL, A., GARDNER, T., CAPLAN, N. & HARGREAVES, D. 2008 Numerical Modelling of the Flow Around Rowing Oar Blades (P71). In *The Engineering of Sport 7*, pp. 353–361. Springer, Paris.

[10] COPPEL, A, GARDNER, T. N., CAPLAN, N. & HARGREAVES, D. M. 2010 Simulating the fluid dynamic behaviour of oar blades in competition rowing. *Proceedings of the Institution of Mechanical Engineers, Part P: Journal of Sports Engineering and Technology* **224** (1), 25–35.

[11] CROWE, C. T., SCHWARZKOPF, J. D., SOMMERFELD, M. & TSUJI, Y. 2011 *Multiphase Flows with Droplets and Particles*. CRC Press.

[12] DICKINSON, M. H. & GÖTZ, K. G. 1993 Unsteady Aerodynamic Performance of Model Wings at Low Reynolds Numbers. *Journal of Experimental Biology* **174** (1), 45–64.

[13] FAGE, A. & JOHANSEN, F. C. 1927 On the flow of air behind an inclined flat plate of infinite span. *Proc. R. Soc. Lond. A* **116** (773), 170–197.

[14] FERNANDEZ-FERIA, R. & ALAMINOS-QUESADA, J. 2018 Unsteady thrust, lift and moment of a two-dimensional flapping thin airfoil in the presence of leading-edge vortices: a first approximation from linear potential theory. *Journal of Fluid Mechanics* **851**, 344–373.

[15] GHARIB, M., RAMBOD, E. & SHARIFF, K. 1998 A universal time scale for vortex ring formation. *Journal of Fluid Mechanics* **360**, 121–140.

[16] HEMMATI, A., WOOD, D. H. & MARTINUZZI, R. J. 2016 Effect of side-edge vortices and secondary induced flow on the wake of normal thin flat plates. *International Journal of Heat and Fluid Flow* **61**, 197–212.

[17] HOERNER, S. F. 1965 *Fluid-dynamic drag: practical information on aerodynamic drag and hydrodynamic resistance*. Hoerner Fluid Dynamics.

[18] HSIEH, S. T. 2003 Three-dimensional hindlimb kinematics of water running in the plumed basilisk lizard (Basiliscus plumifrons). *Journal of Experimental Biology* **206** (23), 4363–4377.

[19] JACOBS, A. F. G. 1985 The normal-force coefficient of a thin closed fence. *Boundary-layer meteorology* **32** (4), 329–335.

[20] KIM, H., JEONG, K. & SEO, T. 2017 Analysis and Experiment on the Steering Control of a Water-running Robot Using Hydrodynamic Forces. *Journal of Bionic Engineering* **14** (1), 34–46.

[21] KOUMOUTSAKOS, P. & SHIELS, D. 1996 Simulations of the viscous flow normal to an impulsively started and uniformly accelerated flat plate. *Journal of Fluid Mechanics* **328**, 177–227.

[22] KRASNY, R. & NITSCHE, M. 2002 The onset of chaos in vortex sheet flow. *Journal of Fluid Mechanics* **454**, 47–69.

[23] LEROYER, A., BARRÉ, S., KOBUS, J. M. & VISONNEAU, M. 2010 Influence of free surface, unsteadiness and viscous effects on oar blade hydrodynamic loads. *Journal of Sports Sciences* **28** (12), 1287–1298.

[24] LIAN, Q.-X. & HUANG, Z. 1989 Starting flow and structures of the starting vortex behind bluff bodies with sharp edges. *Experiments in Fluids* **8** (1-2), 95–103.

[25] LUCHINI, P. & TOGNACCINI, R. 2002 The start-up vortex issuing from a semi-infinite flat plate. *Journal of Fluid Mechanics* **455**, 175–193.

[26] LUFF, J. D., DROUILLARD, T., ROMPAGE, A. M., LINNE, M. A. & HERTZBERG, J. R. 1999 Experimental uncertainties associated with particle image velocimetry (PIV) based vorticity algorithms. *Experiments in Fluids* **26** (1-2), 36–54.

[27] MATSUUCHI, K., MIWA, T., NOMURA, T., SAKAKIBARA, J., SHINTANI, H. & UNGERECHTS, B. E. 2009 Unsteady flow field around a human hand and propulsive force in swimming. *Journal of Biomechanics* **42** (1), 42–47.

[28] MEIROVITCH, L. 2001 *Fundamentals of Vibrations*. McGraw-Hill.

[29] PATTON, K. T. 1965 An experimental investigation of hydrodynamic mass and mechanical impedances. PhD thesis, 1979, MS Thesis, Univ. of Rhode Island.

[30] PAYNE, P. R. 1981 The virtual mass of a rectangular flat plate of finite aspect ratio. *Ocean Engineering* **8** (5), 541–545.

[31] PRANDTL, L. 1904 Über Flussigkeitsbewegung bei sehr kleiner Reibung. *Verhandl. III, Internat. Math.-Kong., Heidelberg, Teubner, Leipzig, 1904* pp. 484–491.

[32] PULLIN, D. I. 1978 The large-scale structure of unsteady self-similar rolled-up vortex sheets. *Journal of Fluid Mechanics* **88** (3), 401–430.

[33] RINGUETTE, M. J., MILANO, M. & GHARIB, M. 2007 Role of the tip vortex in the force generation of low-aspect-ratio normal flat plates. *Journal of Fluid Mechanics* **581**, 453–468.

[34] ROBERT, Y., LEROYER, A., BARRÉ, S., RONGÈRE, F., QUEUTEY, P. & VISONNEAU, M. 2014 Fluid Mechanics in Rowing: The Case of the Flow Around the Blades. *Procedia Engineering* **72**, 744–749.

[35] SAVITZKY, A. & GOLAY, M. J. E. 1964 Smoothing and Differentiation of Data by Simplified Least Squares Procedures. *Analytical Chemistry* **36** (8), 1627–1639.

[36] SCHNEIDER, K., PAGET-GOY, M., VERGA, A. & FARGE, M. 2014 Numerical simulation of flows past flat plates using volume penalization. *Computational and Applied Mathematics* **33** (2), 481–495.

[37] SCHUBAUER, G. B. & DRYDEN, H. L. 1937 The effect of turbulence on the drag of flat plates. *NACA Annual Report* **22**, 129–133.

[38] SLIASAS, A. & TULLIS, S. 2009 Numerical modelling of rowing blade hydrodynamics. *Sports Engineering* **12** (1), 31.

[39] TULLIS, S., GALIPEAU, C. & MORGOCH, D. 2018 Detailed On-Water Measurements of Blade Forces and Stroke Efficiencies in Sprint Canoe. *Proceedings* **2** (6), 306.

[40] WEST, G. S. & APELT, C. J. 1982 The effects of tunnel blockage and aspect ratio on the mean flow past a circular cylinder with Reynolds numbers between 104 and 105. *Journal of Fluid Mechanics* **114**, 361–377.

[41] WILLIAMSON, C. H. K. 1996 Vortex dynamics in the cylinder wake. *Annual review of fluid mechanics* **28** (1), 477–539.

[42] XU, L. & NITSCHE, M. 2015 Start-up vortex flow past an accelerated flat plate. *Physics of Fluids* **27** (3), 033602.

[43] YU, Y. T. 1945 Virtual masses of rectangular plates and parallelepipeds in water. *Journal of Applied Physics* **16** (11), 724–729.

3

HYDRODYNAMICS OF ROWING PROPULSION

This chapter presents the results of the time-resolved flow field measurements around a realistic rowing oar blade that moves along a realistic path through water, together with the simultaneously measured hydrodynamic forces acting on the blade. The aim of these experiments is to identify the relevant flow phenomena that govern rowing propulsion, and subsequently use this information to adjust the oar blade configuration to improve rowing propulsion. Analysis of the instationary flow field around the oar blade during the drive phase indicated how the initial formation, and subsequent development, of leading edge and trailing edge vortices are related to the generation of instationary lift and drag forces, and how these forces contribute to rowing propulsion.

To quantify the rowing propulsion efficiency we introduced the energetic efficiency η_E and the impulse efficiency η_J, where the latter can be interpreted as the alignment of the generated impulse with the propulsive direction. It is found that in the conventional oar blade configuration, the generated impulse is not aligned with the propulsive direction, indicating that the propulsion is suboptimal. By adjusting the angle at which the blade is attached to the oar the generation of leading and trailing edge vortices is altered such that the generated impulse better aligns with the propulsive direction thus increasing the efficiency.

This chapter (with minor adaptations) is submitted as an article to Journal of Fluid Mechanics (under review, April 2020).

3.1. INTRODUCTION

3.1.1. COMPETITIVE ROWING

Competitive rowing is an Olympic sport where the differences between the winner and the runners-up are very small, usually less than 1 s over a 2,000 m race while a race typically lasts 6 minutes. Since finishing times are so close, small improvements of the hydrodynamic propulsion can have a large impact on the outcome of a race. The optimisation of the propulsion requires good understanding of the oar blade motion and the flow field around the oar blade with its corresponding hydrodynamic forces. In this study we capture the oar blade kinematics during actual on-water rowing and then reproduce the (scaled) motion in a laboratory, which enables the use of advanced flow field measurement techniques, such as particle image velocimetry (PIV), together with simultaneous force measurements.

After the athlete inserts the oar blade in the water and exerts a force on the handle, the oar is pivoting on the oar lock and moves through the water generating propulsion; this is called the *drive* phase. Throughout the drive phase the oar blade remains in a vertical position and at a constant depth with its top edge at the height of the otherwise unperturbed free surface. In this study it is assumed that the rowing motion and generated forces are in the horizontal plane (x,y-plane), because (1) the kinematics during the drive phase are exclusively in this plane, and (2) it is known that during on-water rowing athletes do not need to exert any (significant) vertical force on the oar handle to keep the oar blade at constant depth below the surface. This implies that the resultant force on the rowing oar blade is also solely in the x,y-plane.

The oar blade path follows from the superposition of the pivoting motion of the oar on the motion of the pivot point, i.e. the boat motion, as illustrated in figure 3.1. In that figure, both the boat velocity and the angular velocity of the oar are taken constant, while in reality both vary in time. The positive x-direction is defined as the direction of the boat motion, the y-direction is perpendicular and outwards to that (away from the hull) in the horizontal plane[1], and the angle θ defines the oar orientation, where $\theta = 0°$ is parallel to the y-direction. The oar angle θ is defined positive in counter-clockwise direction, and thus increases from the catch, e.g. $\theta = -50°$, to the release, e.g. $\theta = 30°$.

3.1.2. PREVIOUS RESEARCH ON ROWING

The hydrodynamics of a steady flow over an oar blade has been investigated both numerically and experimentally by Caplan & Gardner [5] and Coppel *et al.* [6], but neither account for the presence of a free surface, nor do they account for the accelerations and decelerations of the oar blade, or the strong curvature of the blade path. In the works of Sliasas & Tullis [22], Leroyer *et al.* [15] and Robert *et al.* [21] the unsteady motion of the oar blade was incorporated in their numerical simulations using commercial software. They all found that the results for unsteady flow differed substantially from steady flow over an oar blade. In the work by Robert *et al.* [21] the results are benchmarked against unsteady experimental work by Barré & Kobus [3] and were found to match reasonably well only when the free surface and unsteady motion of the oar blade were incorporated. Also, it should be noted that the rowing motion in the benchmark was strongly simplified, with

[1] Note that the resulting definition is 'port/starboard agnostic'.

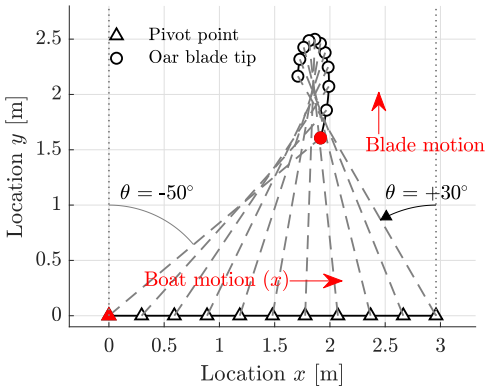

Figure 3.1: A generic oar blade path composed of the boat motion along a straight line (in positive x-direction) and the rotation of the oar around a pivot point fixed to the boat (with $\theta = 0°$ corresponding to a position of the oar perpendicular to the boat motion). For simplicity, both the angular velocity and the boat velocity are taken constant for this generic path with $V_{boat} = 3.7$ ms^{-1} and $\omega = 100°$s^{-1}. The grey dashed lines represent the oar orientation, and the open spheres mark the oar blade tip. The oar blade tip moves in positive y-direction at the catch (red marker) and in negative y-direction during the last part of the stroke.

the most important simplification being the absence of a catch and release, i.e. the rowing oar blade was kept submerged during both the drive and recovery phases such that consecutive strokes were no longer hydrodynamically independent. One of the most advanced measurement of the forces acting on a rowing blade was carried out by Hofmijster *et al.* [12] who carried out on-water force measurements. However, in that study the flow field itself was not investigated. Due to technical limitations they were unable to validate their assumption regarding the point of application of the hydrodynamic forces acting on the blade, which was needed for the calculation of the efficiency of the rowing motion. Labbé *et al.* [14] investigated the optimal oar characteristics, e.g. the optimal inboard and outboard length of the oar, by use of a theoretical model and a model rowing boat with four 'robot rowers', i.e. pulley-mass systems that provide a constant force during the propulsive phase. In their study the actual flow around the oar blade was not investigated.

The accurate numerical simulation of the flow around a rowing oar blade is difficult because of the high Reynolds number, $Re \approx \mathcal{O}(10^5)$-$\mathcal{O}(10^6)$, the presence of a free surface, the complex path of the oar blade during the drive phase with large accelerations and decelerations (up to 10 ms^{-2}), and the lack of a suitable turbulence model for the strongly anisotropic flow. Experimental work in a laboratory environment is difficult mainly because the oar blade moves fast along a complex path that is difficult to replicate, especially due to the large accelerations and decelerations. Although the oar blade force can be measured during actual on-water rowing, investigating the flow field outside a laboratory environment using advanced techniques, like particle image velocimetry (PIV), is extremely challenging. Also, it is evident that the focus of most rowing research is on the measurement of forces and not on flow field phenomena that play a role in the propulsion in rowing, which is the subject of this study.

The objective of this study is to provide insights in the flow field around a rowing oar blade that can be used to improve rowing performance. The flow field around a realistic

oar blade and for realistic rowing motion is determined through particle image velocimetry. With force measurements performed simultaneously with the PIV the flow phenomena that generate propulsion during the drive phase are identified.

3.1.3. HYDRODYNAMIC FORCES

The oar blade moving along its path can be considered as a plate-like geometry at a varying angle of attack. For (quasi-) steady flow, the hydrodynamic force acting on the oar blade can be decomposed in a lift force component F_L and the drag force component F_D defined as:

$$F_D = \frac{1}{2}\rho|V|^2 C_D A \qquad \text{and} \qquad F_L = \frac{1}{2}\rho|V|^2 C_L A, \tag{3.1}$$

where ρ is the fluid density, $|V|$ is the velocity magnitude of the incoming flow, A is a representative surface, and C_D and C_L are the drag and lift coefficients, respectively. Under steady conditions for sufficiently high Re the drag coefficient is independent of Re. Both the lift and drag coefficients vary with the angle of attack. The lift coefficient C_L increases with angle of attack to a maximum. For still larger angle of attack the lift decreases due to massive flow separation, which is called stall [2].

Previous research by Caplan & Gardner [5] and Coppel *et al.* [6] showed that considering the flow around the oar blade as steady or quasi-steady does not produce realistic results. Studies on unsteady hydrodynamics indeed show that both the lift and drag can be strongly increased by an unsteady motion of the object in the flow. An acceleration of the object enhances the hydrodynamic drag through the mechanism of added mass, as described by Yu [28] and Patton [18] for flat plates. The increase in drag on the object is even larger for accelerations over longer durations due to the formation of trailing vortical structures, as described by e.g. Pullin & Wang [19], Ringuette *et al.* [20], Xu & Nitsche [27] and Grift *et al.* [11].

The enhancement of lift due to an acceleration of a plate-like geometry is described extensively in various studies, e.g. by Dickinson & Götz [7] or Birch & Dickinson [4], who both investigated insect flight where the lift through unsteady wing beating is larger than the lift determined from steady flow analysis. A dominant mechanism in the observed lift enhancement is the occurrence of a leading-edge vortex (LEV). An excellent overview of the mechanics and modelling of LEVs is given by Eldredge & Jones [9], where leading edge vortices are investigated for a variety of plate kinematics at varying angles of attack, e.g. impulsively started plates, translational pitching plates, and rotating plates.

It is interesting that the studies on unsteady drag and the studies on unsteady lift produce very similar force profiles for accelerating plates. Also, these studies adopt the same dimensionless time, which is effectively the number of characteristics lengths travelled by the object. For example, Eldredge & Jones [9] refer to this as the time measured in convective time units, while Gharib *et al.* [10] and Grift *et al.* [11] refer to it as the dimensionless formation time. The work by Eldredge & Jones [9] on LEVs is limited to a maximum angle of attack of 45°, and the normal plates studied, e.g. by Gharib *et al.* [10] and Grift *et al.* [11], are (obviously) limited to a 90° angle of attack.

3.1.4. DECOMPOSITION OF THE HYDRODYNAMIC FORCE

Figure 3.2 illustrates three decompositions of the measured hydrodynamic force on the oar blade that are used throughout this study[2]. The force on the oar blade is measured as the normal component F_n and tangential component F_t relative to the rowing oar blade. To investigate the propulsion we also define F_x as the propulsive component of the hydrodynamic force in x-direction, i.e. the direction of the boat motion, and the non-propulsive component F_y that is perpendicular to F_x and directed in the positive y-direction. To decompose the hydrodynamic force in a lift component F_L lift and a drag component F_D drag it is necessary to define a proper reference velocity. This is not trivial, since the oar blade is not only translates in the x,y-plane, but it is also rotates in this plane. Therefore, a single point on the blade is chosen to define a single flow velocity. We have chosen the blade tip as reference location, since, based on the kinematics, it is expected that a LEV will be formed at the blade tip during the first part of the drive phase when the blade moves sideways under quite a large angle of attack α, as shown in figure 3.2. In this figure, the solid grey line represents the path of the blade tip. The drag F_D is defined opposite to the motion of the blade tip and the lift F_L is perpendicular to F_D. The angle of attack α is defined as the angle between the chord line of the blade and the tangent of the trajectory of the blade tip, as shown in figure 3.2.

3.1.5. DEFINITION OF EFFICIENCY AND EFFECTIVENESS

Two aspects of the drive are considered to characterise the performance of the rowing motion: *effectiveness* and *efficiency*. The propulsion that is generated during the drive is the total change in momentum in x-direction, i.e. the change in the x-component of the impulse vector $\vec{J}$ that is defined as:

$$\vec{J} = \int_{t_{catch}}^{t_{release}} \vec{F}(t)\,dt, \tag{3.2}$$

where t_{catch} and $t_{release}$ are the times when the oar blade enters and leaves the water, respectively, and $\vec{F}$ is the hydrodynamic force vector that can be decomposed in a propulsive component F_x and a non-propulsive component F_y. The effectiveness of the propulsion is defined as J_x, i.e. the component of the impulse in x-direction.

For the athlete the cost of generating propulsion is the total energy spent (work performed) during the drive phase. Therefore, it is interesting to define an efficiency in terms of propulsion per unit energy. Since both the kinematics of the oar blade (translation $\vec{V}$ and rotation $\vec{\omega}$) as well as the hydrodynamic force $\vec{F}$ and moment $\vec{M}$ are known, the instantaneous power P can be defined as:

$$P(t) = \vec{F}(t) \cdot \vec{V}(t) + \vec{M}(t) \cdot \vec{\omega}(t), \tag{3.3}$$

and the total energy spent (work performed) E during the drive then becomes:

$$E = \int_{t_{catch}}^{t_{release}} P(t)\,dt. \tag{3.4}$$

[2]Note that this figure is not a free body diagram. It describes the force decomposition of the measured normal F_n and tangential component F_t into drag, lift, propulsive and non-propulsive force and shows the path of the blade tip that was chosen as point of reference to be able to determine the angle of attack α.

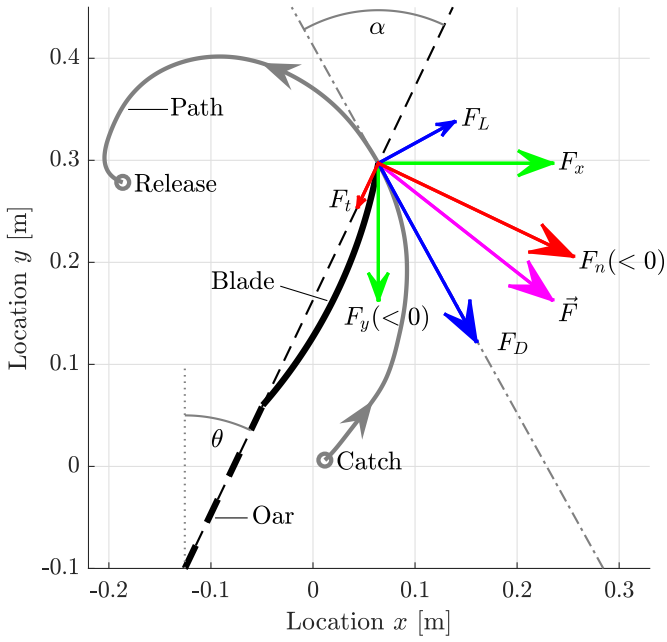

Figure 3.2: The blade (solid black line) moving along the path (solid grey line) from 'catch' towards the 'release' in the direction illustrated by the tangential line (dash-dotted grey) at an angle of attack α, i.e. the angle between the path tangent and the oar blade that is at an orientation θ. The hydrodynamic force on the oar blade $\vec{F}$ (magenta) consists of a component tangential to the blade F_t and normal to the blade F_n (red). The measured force can also be decomposed in a propulsive component F_x and a non-propulsive component F_y (green) that are defined parallel to the x-direction and y-direction, respectively. Alternatively, the hydrodynamic force can be decomposed in a lift component F_L and a drag component F_D (blue), defined perpendicular and opposed to the direction of motion, respectively. The annotation '(< 0)' indicates that the vector component opposes the direction that is defined as positive.

The energetic efficiency can now be defined as the ratio of the effectiveness J_x and the energy E as in:

$$\eta_E = \frac{Jx}{E}. \tag{3.5}$$

Note that this quantity is not dimensionless and has the dimension of sm^{-1}, i.e. a reciprocal of velocity. Multiplication of η_E by a reference velocity would yield a dimensionless quantity. However, within the scope of this study we did not find a meaningful reference velocity that led to a dimensionless energetic efficiency that provides more insight than the dimensional energetic efficiency defined in equation 3.5.

Another approach to quantify the efficiency of rowing, is to determine the degree in which the impulse $\vec{J}$ is in the desired direction for propulsion, i.e. in the x-direction. The impulse efficiency η_J is defined as the alignment of the impulse vector with the x-direction:

$$\eta_J = \frac{J_x}{|\vec{J}|}, \tag{3.6}$$

with $0 < \eta_J < 1$, where $\eta_J = 1$ indicates that the impulse vector is directed in the propulsive direction, and $\eta_J = 0$ indicates that the impulse vector is directed perpendicular to that, i.e. not contributing to propulsion at all. Alternatively, one could use the angle ϕ_J between the impulse vector $\vec{J}$ and the propulsive direction x as a measure of efficiency[3]:

$$\phi_J = \arctan\left(\frac{J_y}{J_x}\right). \tag{3.7}$$

3.2. OAR BLADE KINEMATICS

3.2.1. KINEMATICS BY IMAGE ANALYSIS OF ON-WATER ROWING

To determine the oar blade kinematics, a rowing boat passing underneath a bridge is filmed from atop of the bridge. The camera (GoPro Hero 5 black) is aimed downwards, perpendicular to the water surface, and 1920×1080 pixel images are recorded at a rate of 120 frames per second (fps). The oar blade kinematics are obtained by tracking markers on the oar using a correlation-based algorithm. The markers on the oar also serve as a calibration target to transform the recorded kinematics from the image domain (pixels) to the physical domain (meters).

The lens distortion is removed from the captured images by using the commercial software MATLAB 2018B, which has a built-in chequerboard calibration and fish-eye model based on the model proposed by Urban *et al.* [24]. The oar blade kinematics are then obtained by using a template-based image correlation similar to that proposed by van Houwelingen *et al.* [13]. The oar blade path is captured with a resolution of 4.2 mm in the physical plane, while the algorithm uses sub-pixel accurate correlation through peak fitting [1]. The oar blade path is determined as a function of time based on the marker locations in each captured frame. A typical result is shown in figure 3.3. The start and end of the drive phase are determined by visual inspection of the captured images.

The kinematics of an oar blade are determined for three scenarios: a men's coxless four (M4-) at race pace and at 'standard' pace, i.e. the pace that can be maintained for

[3] Note that the impulse efficiency η_J and angle ϕ_J are directly related through $\eta_J = \sin\phi_J$.

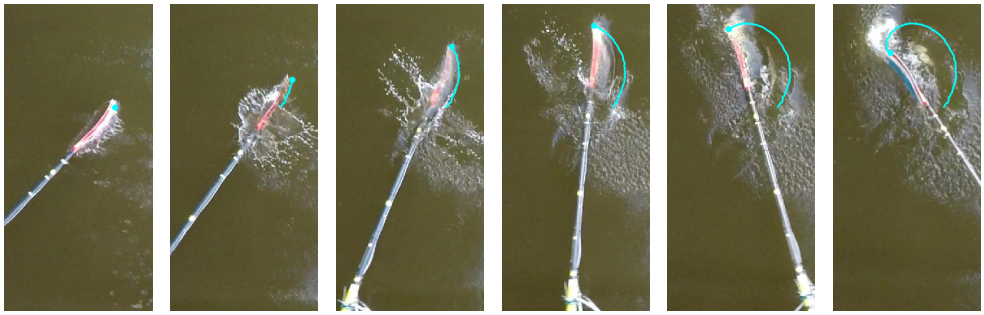

t_d = 0.00 s (catch) t_d = 0.15 s t_d = 0.32 s t_d = 0.48 s t_d = 0.64 s t_d = 0.81 s (release)

Figure 3.3: The path of the oar blade tip (solid blue line) during the drive of a men's coxless four (M4-) from catch to release at equidistant times. Images were acquired by filming from a fixed position on a bridge viewing vertically downward.

a long time without getting exhausted, under neutral weather conditions, and a men's coxed four (M4+) at standard pace with strong head wind. All participants are considered experienced elite rowers and the resulting oar blade paths are shown in figure 3.4. In all three scenarios the blade enters the water with its tip at the location $x = 0$, $y = 0$, after which the blade moves along the path and rotates counter-clockwise. Typical boat velocities are 4, 4.5 and 5 ms^{-1} for the M4+, M4- at standard pace, and the M4- at race pace, respectively. Figure 3.4b shows that for all scenarios the catch occurs at $\theta \approx -50°$ and the oar angle increases approximately linear over time. The release angle varies between $\theta \approx 25°$ for the slowest boat (M4+, head wind) and $\theta \approx 30°$ for the fastest boat (M4-, race). Also a clear difference in *slip* is observed, i.e. the distance the oar blade travels through the water in negative x-direction (opposed to the boat motion). The slip is largest for the slowest scenario, the M4+ with head wind, and smallest for the fastest scenario, the M4- at race pace, see figure 3.4a.

The kinematics of the M4- at standard pace was chosen for further analysis, since its velocity and acceleration, scaled down for use in the laboratory as discussed in §3.3.2, are within the operating range of our experimental set-up, see §3.3 for details. The chosen kinematics lay in between the kinematics of the other two more extreme scenarios and are thought to be representative for a variety of rowing strokes.

3.3. EXPERIMENTAL SET-UP

The experimental set-up used in this study is essentially the same set-up used by Grift *et al.* [11] with some minor adaptations. The oar blade kinematics are reproduced in the experimental set-up (see figure 3.5) using a 1:2 scale model of the oar blade attached to a force/torque transducer (AMTI 6-DOF with a sample rate of 10 kHz), which in turn is mounted on the arm of an industrial robot (Reis Robotics RL50) via a cylindrical strut (with a circular cross-section) piercing the free surface such that the top of the oar blade coincides with the free surface when the latter is unperturbed. The strut holds the blade at the same point as that the oar shaft holds the blade during actual on-water rowing.

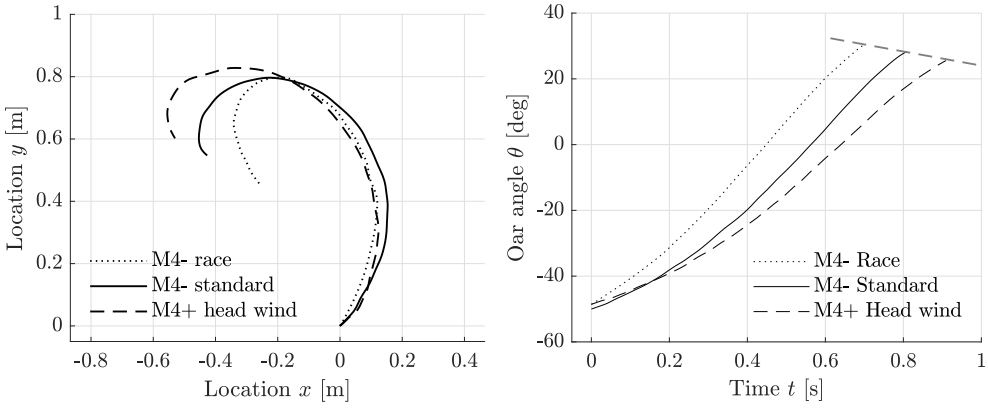

(a) (b)

Figure 3.4: (a) The oar blade paths for a men's coxed four (M4+) with head wind (dashed line), and for a men's coxless four (M4-) at race pace (dotted line) and standard pace (solid line). (b) The oar angle θ as a function of time t during the drive phase. The release angle decreases for faster boats (dashed grey line).

The robot position is sampled at a default rate of 92 Hz with a resolution of 1 µm and is repeatable within 0.1 mm, which is small with respect to the typical dimensions of the oar blade and its path. It is assumed that the hydrodynamic force on the strut is negligible (based on a much smaller strut frontal area $\approx 10^{-4}$ m^2 compared to the blade area ≈ 0.02 m^2, while the drag coefficients are of the same order of magnitude). The force due to the inertia of the strut and blade are not negligible. To isolate the force due to the fluid flow from the measured force, each experiment was performed in both water and air and the measured force in air was subsequently subtracted from the measured force in water.

The robot arm is placed above an open-top glass tank having a horizontal cross-section of 2 m × 2 m and a height of 0.6 m filled with water up to 0.5 m. The size of the tank is chosen as large a practically feasible. To estimate the effect of the finite size of the tank on the hydrodynamics, a surface blockage is defined as the ratio of the surface area of the blade $A_{blade} \approx l_a \times l_b$ (see figure 3.6a) and the tank cross-section in the vertical plane A_{tank} = 2 m × 0.5 m. This results in a blockage ratio of 0.034, which according to West & Apelt [26] is sufficiently small to assume that the walls of the tank do not have a significant effect on the hydrodynamic force on the blade. During the experimental runs surface waves are generated, but measuring a single stroke in the set-up is completed before waves are reflected from the tank wall to the oar blade. The water in the tank is kept at a temperature of 20°C, to keep the water density ρ and water viscosity μ constant at ρ = 1.0×10^3 kgm^{-3} and $\mu = 1.0 \times 10^{-3}$ Pa s, respectively. Each measurement is performed in water that is completely stagnant, which in practice requires 15 minutes between experimental runs.

3.3.1. PARTICLE IMAGE VELOCIMETRY

The vorticity in a selected horizontal plane is obtained through particle image velocimetry (PIV) [1] to capture the intricacies of the flow around the oar blade. The plane is at the centre of the blade as indicated in figure 3.6a. The tank provides full optical access, i.e. the side walls and bottom of the tank are all made of glass. A PIV camera (Phantom VEO 640L) is positioned underneath the tank and parallel to the water surface, imaging frames of 2560×1600 pixels at 500 fps via a 45° mirror, as indicated in figure 3.5a. The field of view is 0.6 m×1.0 m. Ten grams of neutrally buoyant fluorescent spherical tracer particles (Cospheric UVPMS-BR-0.995, 53-63 μm diameter) are added to the water. These particles are illuminated using two overlapping light sheets from opposing sides to avoid shadows from the opaque oar blade model that is positioned in the light sheet. The light sheets are generated using a single dual cavity Nd:YAG laser (Litron 150 W LDY303-HE PIV) followed by a beam splitter.

The acquired images are processed using commercial software (LaVision DaVis 8.4). To create image pairs from the sequential images every frame (n) is paired with the next frame (n+1). The exposure time delay Δt between the pair of images at 500 fps is then 2 ms. A multi-pass correlation based PIV algorithm is used to obtain the velocity field from the image pairs. The interrogation windows are set at 64×64 pixels for the first pass and at 32×32 pixels for the two subsequent passes. A 50% overlap between adjacent interrogation windows is used. This results in velocity fields with a vector spacing of 6.1 mm and a typical cumulative first and second vector choice larger than 98% in the part of the flow perturbed by the blade.

3.3.2. SCALING OF THE KINEMATICS AND OAR BLADE

Due to the limitations of the experimental set-up (primarily the maximum velocity and maximum acceleration of the robot) the oar blade kinematics (both geometry and velocity) were reproduced at a 1:2 scale of the actual kinematics. The resulting oar blade model has a width of l_a = 275 mm and a height of l_b = 125 mm, see figure 3.6. To investigate the scaling behaviour the velocity is varied through a velocity scaling factor κ as shown in table 3.1, where κ = 1.00 corresponds to the maximum velocity setting in the laboratory environment, which is 0.5 times the actual velocity during on-water rowing.

As will be discussed in detail in §3.4.2, the ratio of momentum transferred in x-direction, J_x, and in y-direction, J_y, is constant for $\kappa \geq 0.50$ and the magnitude of the hydrodynamic

-	κ [-]	V_{ref} [ms^{-1}]	L_{ref} [m]	T_{ref} [s]	Re [-]	Fr [-]
Real	-	1.77	0.37	0.21	6.57×10^5	0.93
Exp.	1.00	0.89	0.19	0.21	1.64×10^5	0.65
Exp.	0.75	0.66	0.19	0.28	1.23×10^5	0.49
Exp.	0.50	0.44	0.19	0.42	0.82×10^5	0.33
Exp.	0.25	0.22	0.19	0.84	0.41×10^5	0.16

Table 3.1: The effect of different scaling options on the Reynolds number Re, Froude number Fr, and characteristic time scale T_{ref}. During the experiment different velocity scaling factors κ are investigated. Based on the Reynolds number Re all configurations appear to be in the turbulent regime. Based on the Froude number Fr, all configurations appear to be in the so-called subcritical flow regime. The characteristic time scale T_{ref} is identical for real on-water rowing and the experiments at κ = 1.00.

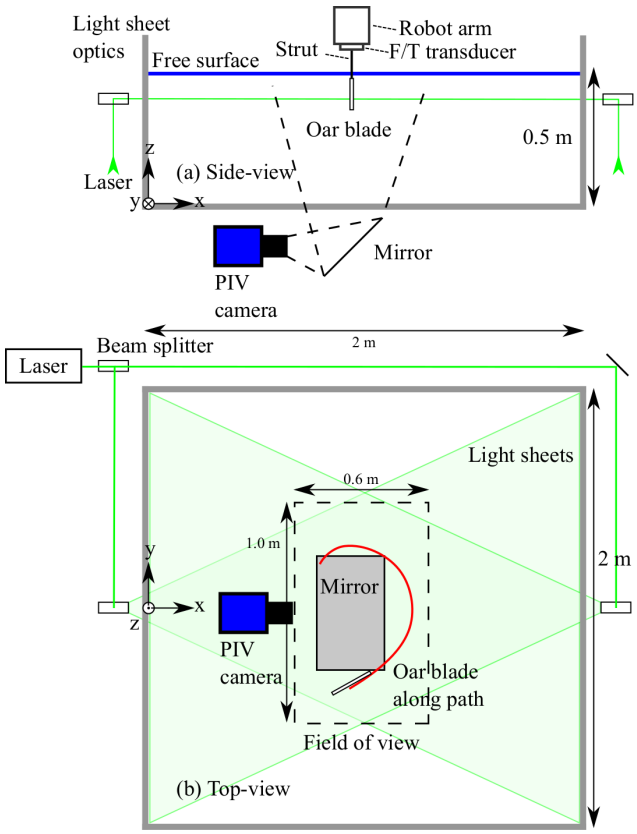

Figure 3.5: (a) Experimental set-up with the robot arm holding the oar blade just below the free surface via a force/torque (F/T) transducer and a strut. (b) Light sheets from opposite sides illuminate the tracer particles in the field of view to avoid shadows due to the opaque oar blade. The PIV camera is positioned underneath the tank and captures images via a 45° mirror.

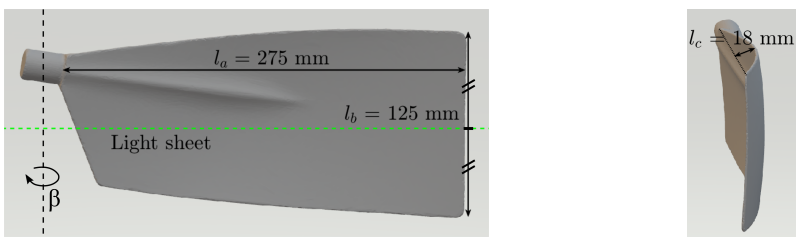

(a) (b)

Figure 3.6: (a) Front view of the oar blade model with blade width l_a = 275 mm, and blade height l_b = 125 mm. The light sheet for the PIV measurements is located at blade half-height. The angle at which the oar is attached to the blade can be adjusted through the blade angle β. The axis of rotation, which is also where the strut holds the oar blade, is perpendicular to the x-y plane and $\beta = 0°$ is the standard orientation of the blade, i.e. the blade is mounted as a direct extension of the oar. (b) Side view of the oar blade model giving an impression of the camber of the blade, with a maximum camber of l_c = 18 mm.

force scales with $V_{ref}^2 \sim \kappa^2$. This implies that the general flow pattern does not vary with κ for sufficiently large velocities, which suggests that the flow has reached the turbulent regime for $\kappa \geq 0.50$. The Reynolds number Re is defined as:

$$Re = \frac{\rho L_{ref} V_{ref}}{\mu}, \tag{3.8}$$

where the characteristic length L_{ref} is based on the plate dimensions $L_{ref} = \sqrt{l_a \times l_b}$, and the characteristic velocity V_{ref} is the mean velocity of the blade tip during the drive phase. The resulting Reynolds numbers for the different configurations are shown in table 3.1. The velocity scaling factor $\kappa = 0.50$ corresponds to a Reynolds number of $Re = 0.82 \times 10^5$, which is deemed sufficiently high to be in the turbulent regime.

Due to the presence of a free surface one might expect that wave-making resistance could be of importance and this is expressed through the Froude number:

$$Fr = \frac{V_{ref}}{\sqrt{g L_{ref}}}, \tag{3.9}$$

where $g = 9.81$ ms^{-2} is the gravitational acceleration. We defined the length scale L_{ref} on the major dimensions of the plate, although it is difficult to determine a characteristic length scale for a plate-like geometry located just below the surface (see Grift *et al.* [11]), but even more so for a rowing oar blade, since its orientation and direction of motion vary strongly in time. At the start of the drive the blade moves through the water sideways barely disturbing the surface, while half-way the drive phase the blade moves approximately perpendicular to its surface. However, with the defined length scale we obtain $Fr < 1$, indicating subcritical flow for on-water rowing and for all experimental configurations, see table 3.1. This explains why scaling with Froude number Fr is not obligatory and the generation of surface waves is not dynamically relevant. The characteristic time scale $T_{ref} = L_{ref}/V_{ref}$ is only the same for actual on-water rowing and the experiments performed for $\kappa = 1$.

3.3.3. VALIDATION OF THE OAR BLADE PATH IN THE EXPERIMENT SET-UP

The industrial robot reproduces the oar blade path very well as shown in figure 3.7a with a maximum deviation of less than 0.01 m, which is small (1%) relative to the total path length of 0.96 m. Also, the blade tip coordinates x and y as a function of time t are very well reproduced as shown in figure 3.7b. At any moment in time the blade tip is within a distance of 0.03 m from the measured kinematics, which again is a small deviation (3%) relative to the total path length of 0.96 m.

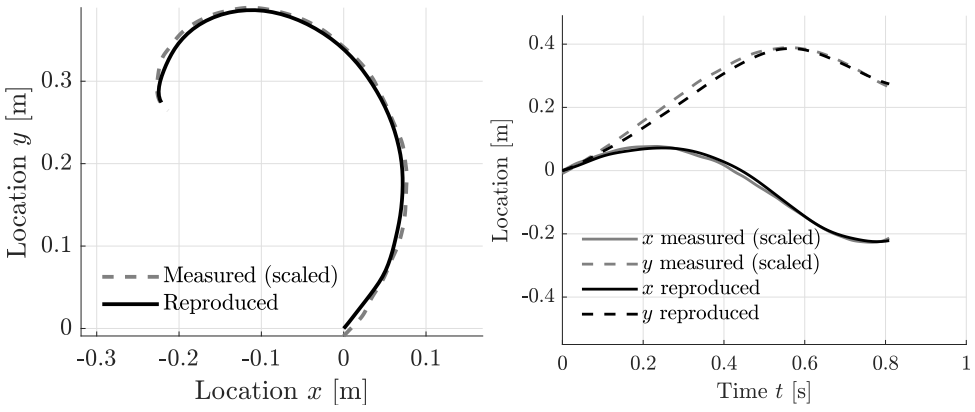

(a) (b)

Figure 3.7: Comparison of the measured (and scaled) path of the oar blade tip (dashed grey line) and the path of the oar blade tip reproduced by the robot (solid black line). (a) The path of the blade tip in the x-y plane. (b) The coordinates x and y of the blade tip as a function of time t.

3.3.4. OVERVIEW OF THE REPRODUCED KINEMATICS

The detailed kinematics as reproduced by the robot are shown in figure 3.8. The kinematics shown in figure 3.8b to 3.8f are plotted against dimensionless time t^* which is defined as

$$t^* = \frac{t - t_{catch}}{t_{release} - t_{catch}}, \tag{3.10}$$

such that the catch is at $t^* = 0$ and the release at $t^* = 1$. The kinematics as function of t^* are identical for all κ. In the figure the kinematics for a standard oar blade geometry ($\beta = 0°$) are shown in black. The kinematics for an adapted blade geometry where the oar blade angle is increased to $\beta = 15°$ are shown in grey. At that angle rowing propulsion is found to be optimal, which is further discussed in section 3.4.4.

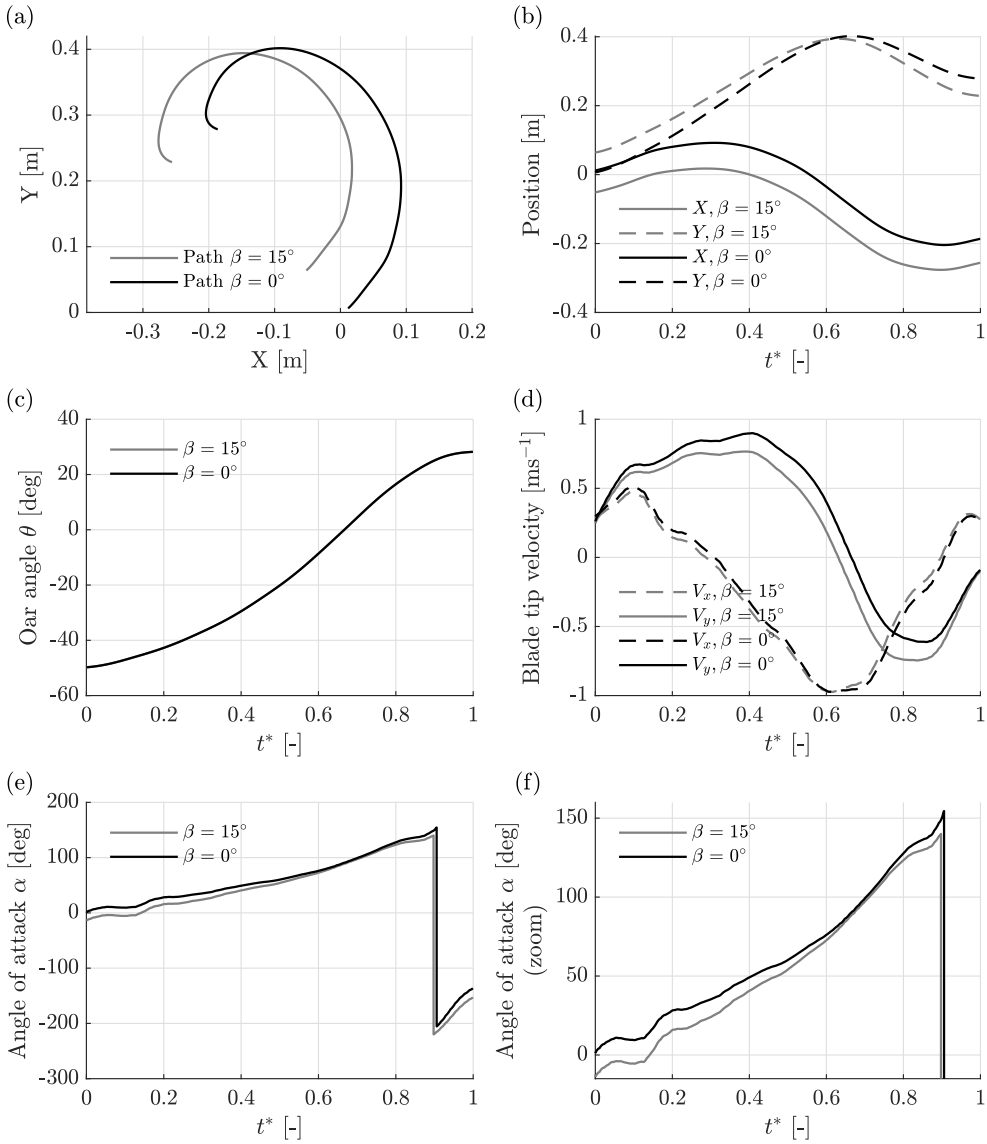

Figure 3.8: (black) Reproduced kinematics for the standard oar blade geometry, i.e. β = 0°, (grey) reproduced kinematics for the optimised oar blade geometry, i.e. β = 15°. (a) The oar blade tip path, (b) the oar blade tip position as a function of dimensionless time t^*, (c) the oar angle θ as a function of dimensionless time t^*, (d) the oar blade tip velocity components V_x and V_y as function of dimensionless time t^*, and (e) and (f) the angle of attack α as a function of dimensionless time t^*.

3.4. RESULTS

In this section, force measurements obtained using the F/T transducer, oar blade kinematics obtained from the robot position data system, and flow fields obtained from the PIV measurements are presented and interpreted to provide insight in the hydrodynamics of rowing propulsion. Results are presented on the force on, and the flow field around, a rowing oar blade moving along the path shown in figure 3.7a. To compare the results for drives with different durations due to different velocity scaling factors κ results are shown as function of dimensionless time t^*. Since the catch and release take a finite amount of time (just like in reality), some hydrodynamic force associated with the catch and release is generated outside the time interval $0 \leq t^* \leq 1$.

3.4.1. REPEATABILITY OF FORCE MEASUREMENTS

To check the repeatability of the robot motion and the force measurements all measurements were performed multiple times for different values of κ. Three realisations for $\kappa = 1.00$ at the standard blade angle $\beta = 0°$ are presented in figure 3.9a. It is seen that the three realisations of the measured force components F_n and F_t overlap almost perfectly. Also, the blade path, i.e. the location of the oar blade tip in time, is reproduced accurately with a maximum deviation of 0.2 mm, which is close to the 0.1 mm repeatability specified by the manufacturer of the robot and very small (0.1 %) relative to the total path length of 0.96 m. The minor fluctuations that appear in the force signal in figure 3.9a are consistent with the fluctuations in the velocity of the blade that is shown in figure 3.9c. For clarity, this is indicated by the dashed red arrows that show that the local maxima in F_t and local minima in F_n correspond to the local maxima in the tip velocity. The velocity fluctuations match the prescribed path and similar velocity fluctuations are found in the recorded path as well.

EFFECTS OF VELOCITY SCALING

It is seen in figure 3.9b that the force signals are qualitatively very similar for different values of κ. Based on figure 3.9d, where the measured force is divided by κ^2, the force indeed appears to scale well with κ^2 (and thus with $|V|^2$), as might be expected from equation 3.1, except around the release at $t^* \approx 1$. During the release the wake that followed the oar blade during the drive phase impinges on the blade, which is further discussed in §3.4.3, and apparently this process somewhat varies with the velocity scaling factor. However, we argue that for the largest part of the drive phase they are in excellent agreement, as is further illustrated by the integrated quantities presented in §3.4.2.

3.4.2. DECOMPOSITION OF A TYPICAL FORCE MEASUREMENT

Figure 3.10 shows the various components of the measured hydrodynamic force according to the three decompositions described in §3.1.4, see figure 3.2.The results in figure 3.10 pertain to a standard blade angle $\beta = 0°$ and a velocity scaling factor $\kappa = 1.00$. Note that $\kappa = 1.00$ can be seen as representative for all $\kappa \geq 0.5$.

DECOMPOSITION IN NORMAL COMPONENT F_n AND TANGENTIAL COMPONENT F_t

In figure 3.10 the hydrodynamic force on the blade is decomposed in a normal component F_n and a tangential component F_t. The normal component F_n first decreases to a

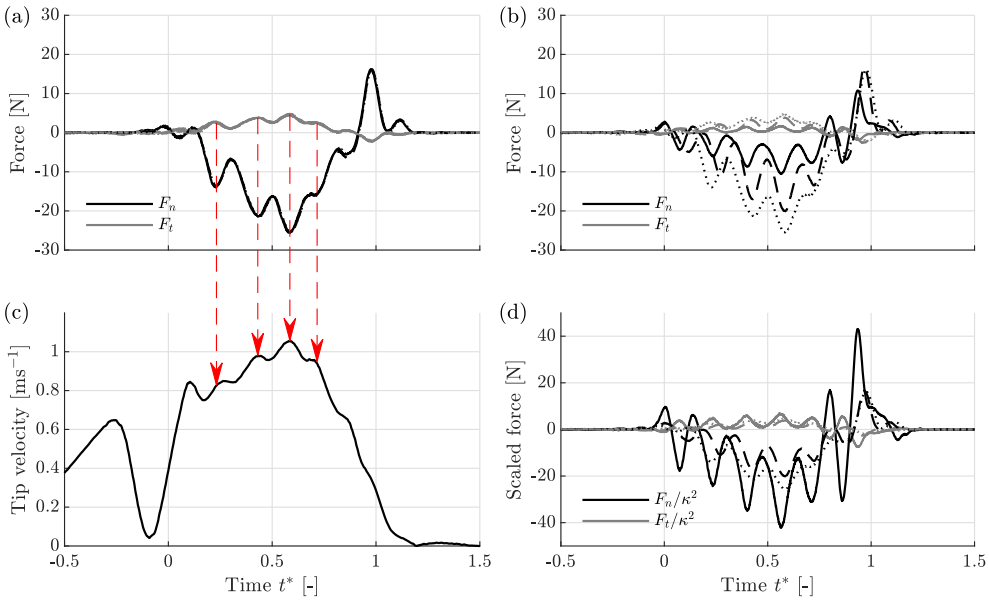

Figure 3.9: (a) Measured force components F_n and F_t as a function of t^* for three realisations at a velocity scaling factor κ = 1.00. The three different realisations are indicated by different line styles, but these lines are overlapping almost perfectly. (b) Measured force components F_n and F_t as a function of t^* for different velocity scaling factors, i.e. κ = 0.50 (—), 0.75 (- - -), 1.00 (· · ·). (c) The small fluctuations in the blade velocity (marked with red arrows) match the fluctuations in the force signal shown in figure 3.9a. (d) The measured force components F_n and F_t as a function of t^* for κ = 0.50 (—), 0.75 (- - -) and 1.00 (· · ·) scaled with κ^2 reasonably match, thus scale similar to equation 3.1.

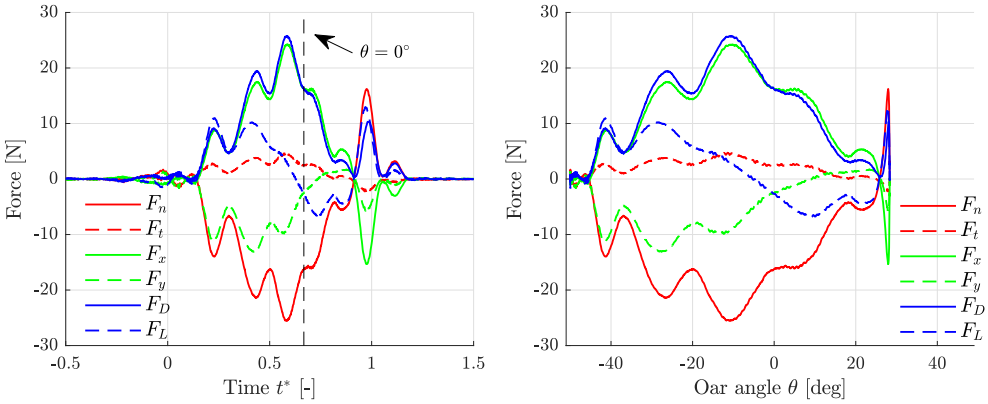

Figure 3.10: The decomposition of measured forces F_n and F_t in propulsive force F_x and non-propulsive force F_y as well as the decomposition in drag force F_D and lift force F_L, see figure 3.2 and equation 1.1, for κ = 1.00. (a) The decomposed forces as a function of t^* and (b) as a function of oar angle θ. In (a) the vertical dashed line shows the time instance when the oar is perpendicular to the boat motion, i.e. θ = 0°. It is evident that the first part of the drive, i.e. when θ<0°, contributes most to the momentum transfer. (b) The maximum in propulsive force F_x occurs just before the perpendicular position of the oar at θ = -10° or t^* = 0.60.

minimum at θ = -10° and then increases again towards a peak around the release at t^* = 1. The normal component F_n acts in the direction of the convex side of the oar blade during the drive phase and reverses only for a short period in time around the release when the wake flow impinges on the decelerating blade.

The tangential component F_t follows a very similar profile, but it has opposite sign and the magnitude is approximately 20% of that of the normal component F_n. Throughout the drive, the tangential component F_t is directed towards the pivot point of the oar and it only reverses for a short period of time around the release. This means that the tangential component is opposing the boat motion for an oar orientation of $\theta < 0°$, and is therefore only contributing positively to propulsion for $\theta > 0°$, i.e. during the last part of the drive. Since in actual on-water rowing the oar is mechanically constrained only in its motion in negative tangential direction, the athlete has to apply a counter-force in negative tangential direction, i.e. push the oar outwards, to keep the oar in place.

DECOMPOSITION IN PROPULSIVE AND NON-PROPULSIVE COMPONENTS F_x AND F_y

Very useful is the decomposition of the hydrodynamic force in a propulsive component F_x and non-propulsive component F_y, as shown in figure 3.10. During most of the drive phase the propulsive component F_x positively contributes to propulsion, i.e. $F_x > 0$. Only around the release the sign of the propulsive component briefly reverses. This is due to the aforementioned wake flow impinging on the decelerating oar blade. Directly after the catch the propulsive component F_x is small and it then steadily increases to a maximum at $\theta \approx -10°$, which is in agreement with the value reported by Soper & Hume [23]. However, a direct comparison between force profiles is difficult since the reported forces in this study, the hydrodynamic forces (isolated from the forces exerted by the athlete and forces due to inertia of the oar blade/shaft), are fundamentally different from the forces generally reported in literature. The reported forces in literature are the sum of hydrodynamic forces, forces applied by the athlete and forces due to inertia of the oar blade/shaft [23]. The non-propulsive component F_y is applying a compressive force perpendicular to the boat motion ($F_y < 0$) throughout most of the drive.

EFFECTIVENESS AND EFFICIENCY

The effectiveness J_x and the efficiencies η_J and η_E are calculated from the propulsive and non-propulsive components F_x and F_y as described in §3.1.5. The effectiveness, J_x and efficiencies, η_J and η_E, as a function of the velocity scaling factor κ are shown in figure 3.11a and 3.11b, respectively, for 57 measurements. The effectiveness J_x appears to be linear in κ. This is explained by the use of a scaling argument. Let $F_x \sim V^2 \sim \kappa^2$, and for the integration interval τ, i.e. the duration of the drive phase, τ, $\tau \sim 1/V \sim \kappa^{-1}$, then $J_x \sim F_x\tau \sim \kappa$. The same argument holds for J_y, which implies that the ratio of these components $\eta_J = J_x/J_y$ is a constant. Indeed the impulse efficiency is constant at $\eta_J = 0.84$ for $\kappa \geq 0.50$, see figure 3.11b. This implies that the flows around the oar blade are qualitatively the same for $\kappa \geq 0.50$. Throughout the remainder of this study only results for $\kappa \geq 0.50$ are presented, as we deem the flow at lower values of κ not representative for actual on-water rowing.

Figure 3.11b shows that the energetic efficiency η_E decreases with increasing κ. Using a similar scaling argument as before we find: $\eta_E = J_x/E$, where $E \sim FV\tau \sim \kappa^2$ so that $\eta_E \sim \kappa^{-1}$. Although the exact behaviour of the energetic efficiency $\eta_E \sim \kappa^{-1}$ cannot be

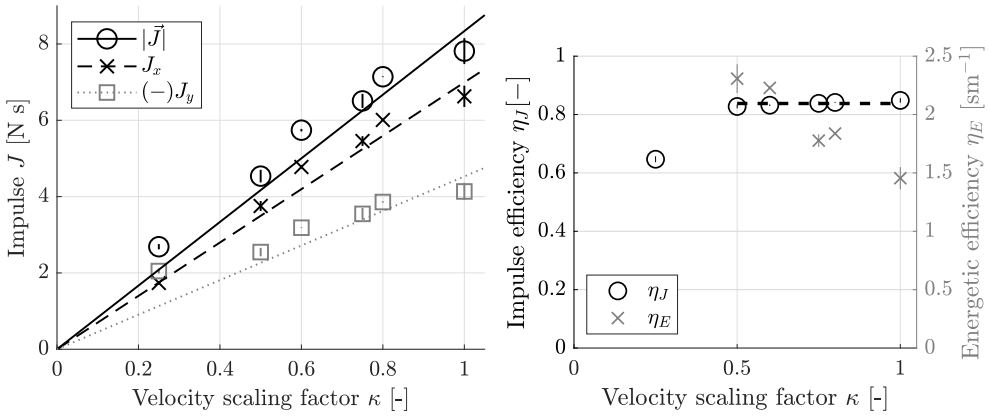

(a) (b)

Figure 3.11: Effectiveness J_x and efficiencies η_J and η_E as a function of κ for a total of 57 force measurements. The markers represent the mean value and the vertical bars through the markers denote $\pm\sigma$ error bars where σ is the standard deviation. (a) The effectiveness J_x, defined in equation 3.2, is approximately linear in κ. (b) For $\kappa \geq 0.50$ the impulse efficiency η_J, defined in equation 3.6, is constant at $\eta_J = 0.84$. The energetic efficiency η_E is decreasing with increasing κ.

confirmed due to the limited range of κ that can be tested in the experimental set-up, η_E is clearly decreasing with increasing κ. In §3.4.4 it is shown empirically that $\eta_E \sim \kappa^{-0.7}$.

CONTRIBUTION OF LIFT AND DRAG TO PROPULSION

By decomposing the measured hydrodynamic force in a lift component F_L and drag component F_D, as defined in figure 3.2 and equation 1.1, it is possible to obtain insight into the relevant flow phenomena that occur during the drive phase. Since the oar blade is shaped somewhat like a thin plate at a finite angle of attack α, it is expected that the oar blade produces drag when moving in a direction normal to the blade surface (i.e. at 90° angle of attack) and the oar blade produces mainly lift at small angles of attack. Figure 3.10 shows that the drag F_D is dominant in the middle of the drive phase, where the blade indeed moves normal to its surface. The lift F_L is predominantly generated at the start of the drive phase and, to a lesser extent, at the end of the drive phase.

In figure 3.10 it is clear that the drag component F_D and the propulsive component F_x are strongly correlated. However, correlation is no causation. When the lift F_L and drag F_D are projected on the propulsive direction x we can see the contribution of the lift and drag to the propulsion, shown in figure 3.12. Contrary to the apparent cause suggested by the correlation, propulsion is caused by both lift and drag. Especially in the first part of the drive phase lift F_{Lx} dominates the propulsion F_x, while half-way the drive the propulsion is solely due to drag F_{Dx}. However, towards the end of the drive lift F_{Lx} again contributes to propulsion, but less so than in the beginning of the drive phase.

3.4.3. FLOW FIELD AROUND THE OAR BLADE

The flow field in a horizontal plane at blade half-height is measured with PIV to investigate what flow phenomena govern propulsion in rowing. The PIV measurements are per-

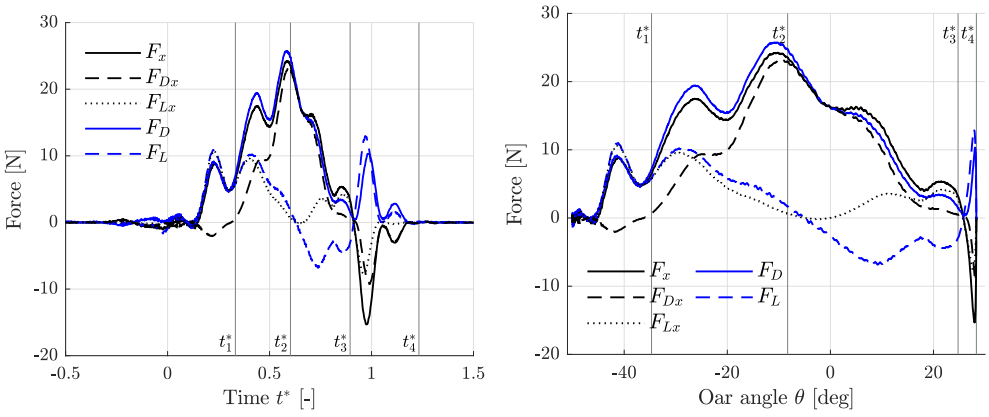

(a) (b)

Figure 3.12: The propulsive force F_x is composed of the propulsive part F_{Dx} due to drag F_D and the propulsive part F_{Lx} due to lift F_L as a function of (a) dimensionless time t^* and (b) the oar angle θ for $\kappa = 1.00$. The lift is positively contributing to propulsion up to the start of the release at $\theta \approx 25°$. In both figures the vertical lines indicate the times of the flow field snapshots shown in figure 3.14. Dimensionless time $t_1^* = 0.33$ is roughly in the middle of the lift phase, $t_2^* = 0.60$ is at maximum propulsion, $t_3^* = 0.89$ is at a minimum drag just before the release and $t_4^* = 1.23$ is just after the release.

formed at $\kappa = 1.00$ to match real on-water rowing as close as possible. The PIV measurements are highly repeatable in the sense that all but the smallest (turbulent) flow features reproduce very well. Each measurement is performed three times and is then phase averaged to reduce the statistical scatter. The vorticity component ω_z is calculated from the velocity vectors by an 8-point estimation based on the local flow circulation as described by Luff *et al.* [17]. Figure 3.13 shows a typical vorticity field together with the velocity vectors to illustrate the resolution of the PIV measurement. In the remainder of this paper the velocity fields will be presented at a lower vector density, i.e. some velocity vectors will be skipped to improve the readability of the figures.

EVOLUTION OF THE FLOW FIELD AROUND THE OAR BLADE

In figure 3.14, the flow field evolution is illustrated by sequential snapshots at the selected times that are indicated in figure 3.12. The oar blade is marked by the black line and its tip follows the path indicated by the grey line. The drive phase starts at $t^* = 0$ with the blade tip at $x = 0$, $y = 0$. At the start of the drive phase the blade moves away from the boat in positive y-direction and generates lift, which contributes to propulsion, i.e. the lift vector has a component in positive x-direction. At $t_1^* = 0.33$, the oar blade is in the middle of its lift generation phase, see figure 3.12a. The corresponding flow field is shown in figure 3.14a. It is seen that a leading edge vortex (LEV) (I) is formed and that a vortex sheet (II) is attached to the trailing edge of the blade. The geometry of the oar blade during this stage is similar to that of a thin airfoil or a curved plate at a small angle of attack. Since the oar blade is rapidly accelerated, see figure 3.9, its motion can be considered as impulsively started. For an impulsively started airfoil a similar vortex sheet at the trailing edge is observed, see figure 3.15. Wagner [25] reported that for an impulsively started airfoil at

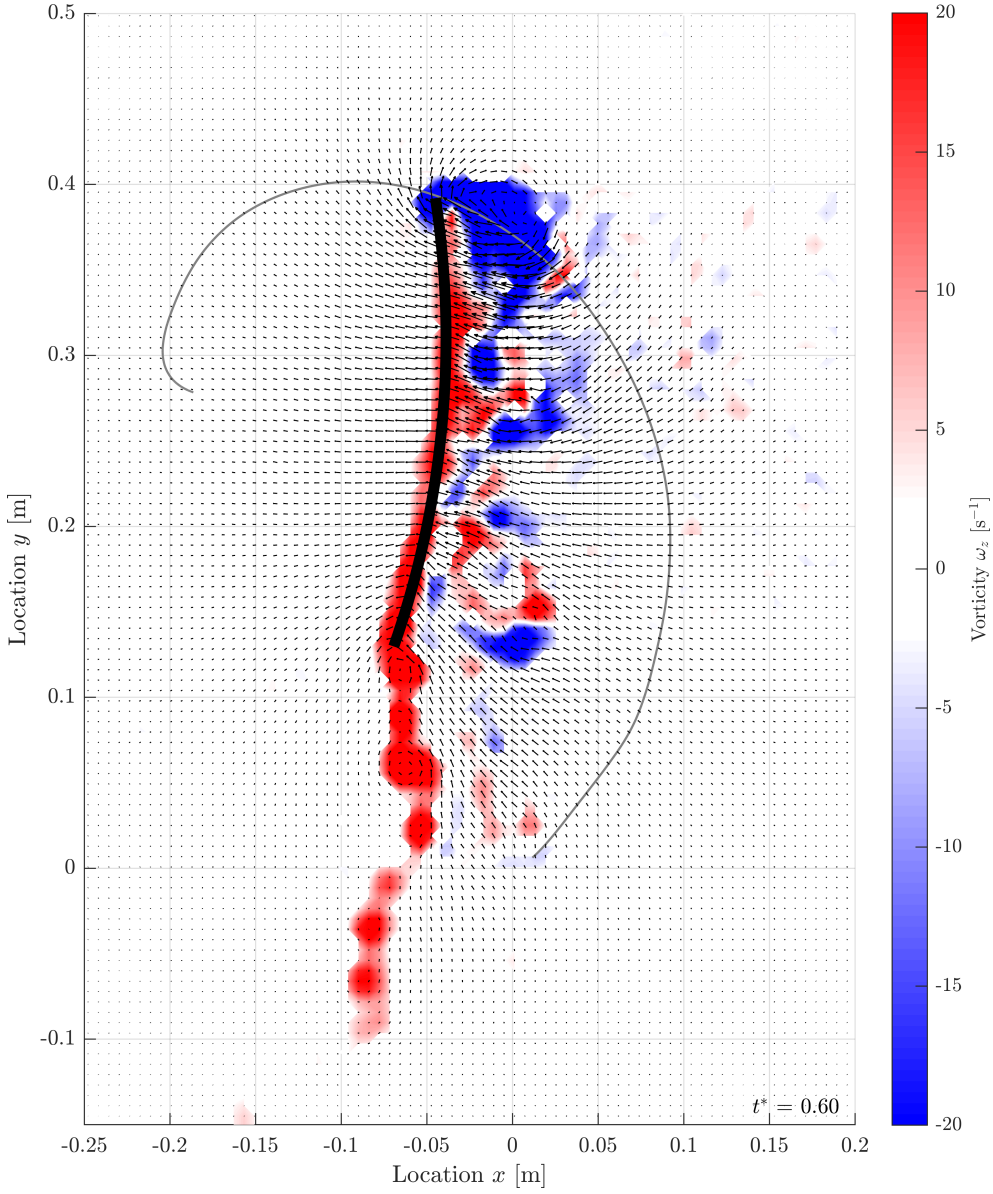

Figure 3.13: The vorticity field around the oar blade for a velocity scaling factor $\kappa = 1.00$ at time $t_2^* = 0.60$, which corresponds to the maximum propulsive force, see figure 3.12. Red and blue indicate positive and negative vorticity, respectively, and the velocity vectors are shown as black arrows. The oar blade is represented by the thick black line, and the oar blade path is shown as a thin grey line.

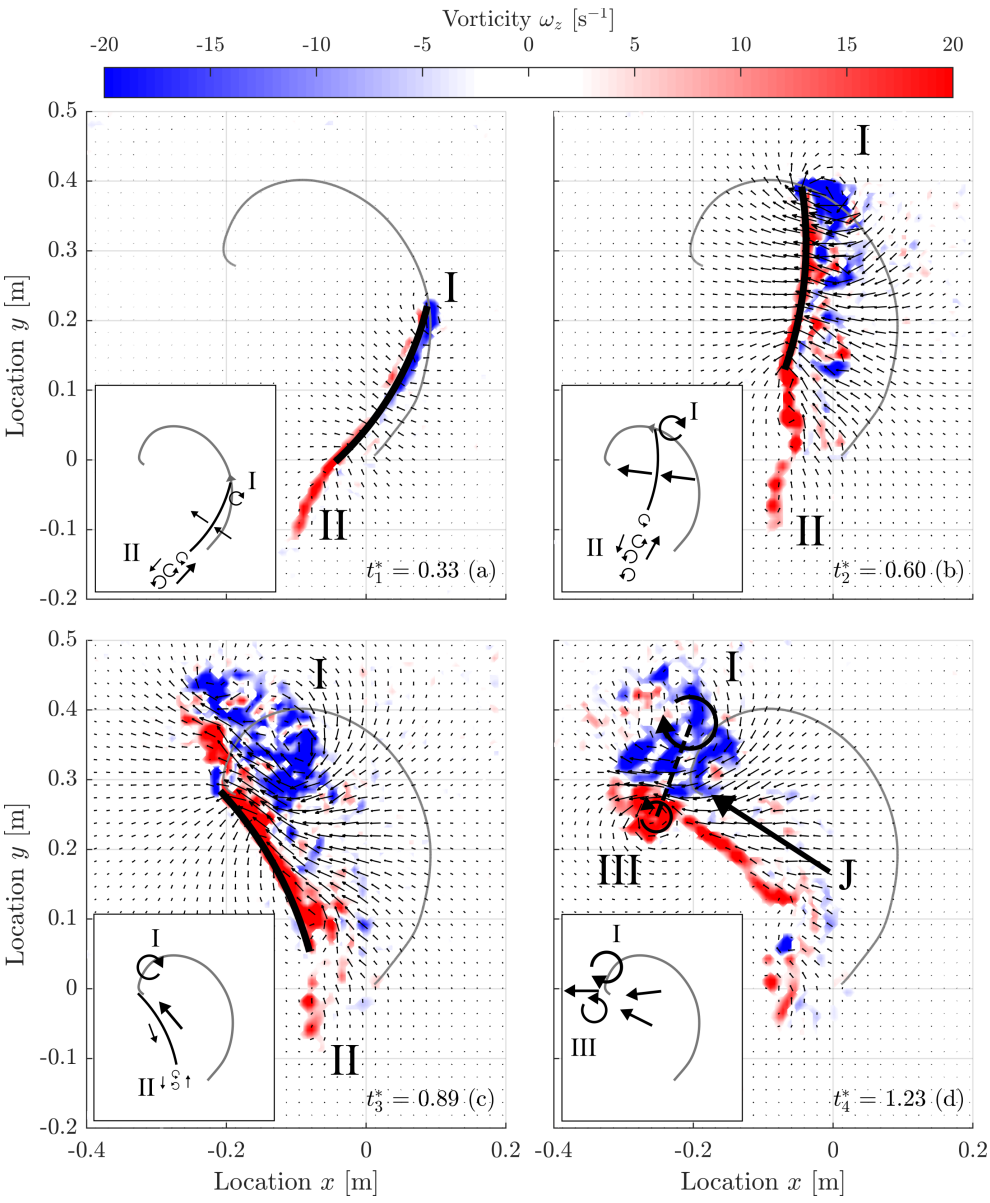

Figure 3.14: Snapshots of the velocity field (black arrows) and the vorticity field (contours) for the dimensionless times t_1^* to t_4^* as indicated in figure 3.12. The snapshots are taken at (a) the start of the drive phase t_1^* = 0.33, (b) in the middle of the drive phase t_2^* = 0.60, (c) just before the release t_3^* = 0.89 and (d) just after the release t_4^* = 1.23. The oar blade and the path of the oar blade tip are shown as black and grey lines, respectively. In each snapshot an inset sketches the main flow features relevant for propulsion. A straight arrow indicates the flow direction and relative magnitude, and the circular arrows indicate vortical structures. Roman numeral I indicates a leading edge vortex and II indicates a vortex street. In (d) a vortex pair I-III and the impulse vector $\vec{J}$ are shown. The trailing-edge vortex layer rolls up in a vortex with opposite circulation than the LEV, so that they form a vortex pair that propels itself to the left. A jet-type of flow is generated more or less in negative x-direction, an indication of propulsion.

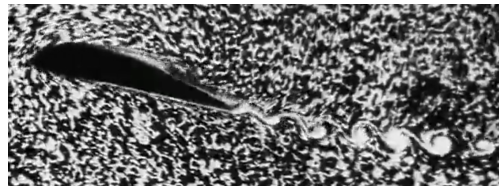

Figure 3.15: A snapshot of the video 'Anfahrt eines Tragflügels (Filmkamera mitfahrend)' by Ludwig Prandtl (1936). An airfoil at a low angle of attack that is impulsively started in a fluid at rest generating lift, while the camera moves with the airfoil. A vortex sheet attached to the trailing edge is clearly visible. (https://doi.org/10.3203/IWF/C-1#t=05:48,08:16)

a small angle of attack, a vortex sheet is formed at the trailing edge and that the lift during the initial translation is small compared to the steady state lift. Only after the airfoil travelled seven chord lengths the lift has reached 90% of its steady state value. This is known as the Wagner effect [16]. For impulsively started airfoils with a sharp edge, like our oar blade, a LEV is also formed. This LEV can be lift enhancing, when a low pressure zone at the convex side of the oar blade is formed, or can be detrimental to the generated lift, when the LEV is located at the concave side of the blade or when the LEV moves close to the trailing edge [16]. Alternatively, the oar blade motion can be seen as a pitching plate, because the angle of attack α, as defined in figure 3.2, increases rapidly. The oar blade motion resembles the plate pitching around its leading edge as described by Eldredge & Wang [8] and Eldredge & Jones [9]. They report that pivoting around the leading edge provides a larger maximum C_L/C_D than pivoting around quarter or half chord length (measured from the leading edge).

The lift generated by the oar blade during the first part of the drive phase has similar magnitude as the generated drag, see figure 3.10, even though the blade moves through the fluid in quite a streamlined fashion. This implies that the generated lift is quite small. In agreement with the observations of Wagner [25], it appears that the blade does not travel far enough through the water to be effective in generating lift. The presence of the LEV does enhance lift, since it remains close to the leading edge at the convex side of the oar blade.

Figure 3.14b depicts the flow field at dimensionless time $t_2^* = 0.60$, when the drag and propulsion are at a maximum. The vortex sheet (II) has grown in length and the LEV (I) has increased in size and has shifted a small distance away from the blade. The angle of attack is now close to 90° (i.e. perpendicular to the path), which explains that the drag is at its maximum while the lift is close to zero, as is seen in figure 3.12. The large vortex (I) is still close to the oar blade and causes a low pressure zone at the convex side of the blade, thus contributing to increased drag, similar to the trailing vortical structure in the study by Grift *et al.* [11].

Figure 3.14c shows the flow field at $t_3^* = 0.89$ when the drag is at its minimum and the lift is of opposite sign compared to the lift generated at t_1^*, but the lift still contributes to the propulsion due to the blade orientation. The trailing vortex (I) has grown even larger in size, but is no longer close to the blade and its low pressure zone is therefore thought unlikely to cause the measured lift. Instead, we hypothesise that the observed lift is the result of the velocity difference between the fluid on both sides of the oar blade. The vortex

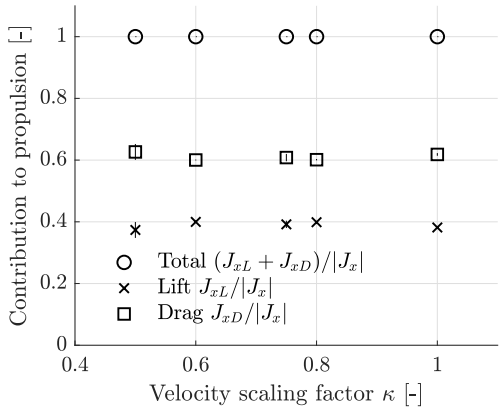

Figure 3.16: The contribution of lift and drag to propulsion (defined as the ratio of the impulse due to lift J_{xL} or drag J_{xD} and the magnitude of the total generated impulse in propulsive x-direction $|J_x|$) for 57 measurements. The vertical bar in each marker indicates the standard deviation of the measurements.

sheet (II) can hardly be discerned anymore. Figure 3.12 shows that a rapid decrease in the propulsive force signal F_x occurs immediately after $t_3^* = 0.89$. This is caused by the oar blade wake that impinges on the blade during the release at $t^* = 1$.

Figure 3.14d shows the flow field after the release at $t_4^* = 1.23$. The large velocity difference between both sides of the oar blade at t_3^* has led to the development of a vortex (III) upon the rapid extraction of the oar blade. In combination with LEV (I) a vortex pair (I-III) is formed, which is clearly visible at the water surface as strong depressions and will be well-known to anyone who has an interest in actual on-water rowing. This vortex pair produces a jet-like flow field in the region in between the cores of the vortices. The direction of the total impulse generated during the drive phase $\vec{J}$, see equation 3.2, is closely related to the orientation of this jet-like structure, i.e. it is perpendicular to a line that connects the cores of the vortex pair.

Figure 3.16 shows that that both lift and drag contribute to propulsion. Lift accounts for 40% of the propulsion and drag for 60%, independent of the velocity scaling factor κ. We have identified a leading edge vortex as a generator of lift and the jet-like structure that forms immediately after the release appears to correspond well with the direction of the generated impulse with is directly related to the impulse efficiency η_J.

3.4.4. IMPROVING HYDRODYNAMIC EFFECTIVENESS AND EFFICIENCY

Figure 3.11b shows that the impulse efficiency η_J is not optimal, i.e. $\eta_J < 1$, due to the generation of an impulse J_y perpendicular to the direction of motion. The propulsion angle corresponding to an impulse efficiency of $\eta_J = 0.84$ is $\phi_J = -28.4°$. This means that the generated impulse is not fully parallel to the direction of motion of the boat, i.e. the x-direction, but instead is directed outwards as is clearly visible in figure 3.14d. In practice this means that part of the work performed by the athlete is used to generate an impulse component J_y that does not contribute to propulsion. To see if the effectiveness and/or efficiency of the drive phase can be improved the oar blade angle β is varied, i.e. the blade is rotated about a vertical axis as illustrated in figure 3.6a. Obtaining maximum efficiency

or effectiveness is not as trivial as rotating the blade by -28.4°, because it was determined in the previous chapter that multiple flow phenomena contribute to propulsion. Both the initial formation and subsequent evolution of LEVs and TEVs differently respond to a change in blade angle. Therefore, the blade angle is varied over a range of angles.

For $\beta > 0°$ the impulse vector $\vec{J}$ is expected to be better aligned with the x-axis (see §3.4.3) thus increasing impulse efficiency η_J, and possibly the effectiveness J_x and the energetic efficiency η_E, since less energy is used to generate non-propulsive impulse J_y. On the other hand, for $\beta < 0°$ the angle of attack α is increased and the LEV discussed in §3.4.3 will generate more lift that could enhance propulsion. For $\beta > 0°$ the LEV will become weaker and is likely to generate less lift.

EFFECTIVENESS FOR DIFFERENT BLADE ANGLES

The blade angle was varied between β = -20° and β = 25° in steps of 5°. Each combination of blade angles β and three selected velocity scaling factors κ = 0.50, 0.75 and 1.00 was tested multiple times resulting in a total of 164 tests. While the blade angle is varied, the kinematics of the oar are kept the same as for the standard oar with blade angle β = 0°, which is referred to as the *standard case*. Of course, in reality a change in blade angle will affect the generated propulsion and consequently change the boat motion, which in part defines the oar blade path. However, this is considered a secondary effect and is neglected in this study.

Figure 3.17a shows the effectiveness J_x as a function of blade angle β for the three velocity scaling factors κ. The most effective blade angle is between β = 0° and β = -5° and the behaviour of the effectiveness J_x with varying blade angle β is very similar for all velocity scaling factors. The effectiveness J_x is approximately linear in κ over almost the entire range of blade angles β as was already observed for the standard case β = 0°. In figure 3.17b the composition of the generated impulse is shown for κ = 1.00, noting that κ = 0.50 and 0.75 behave similarly. The propulsion generated by lift J_{xL} decreases approximately linearly with blade angle β. The propulsion due to drag J_{xD} increases with increasing blade angle up to its maximum at β = 10° after which the propulsion due to drag decreases again. It appears that our hypothesis of increasing lift for lower blade angles $\beta < 0°$ holds, although the loss in propulsion due to drag clearly outweighs the gain in propulsion due to lift. Also, for increasing blade angles $\beta > 0°$ the loss of propulsion due to lift is not compensated by a gain in propulsion due to drag. The contribution of lift J_{xL} and drag J_{xD} for each combination of κ and β can be normalised by dividing these contributions by the total propulsion magnitude $|J_x|$. The normalised contribution of the lift $\hat{J}_{xL}$ and drag $\hat{J}_{xD}$ to propulsion are shown as a function of β in figure 3.17c. The results for different velocity scaling factors are so close that tests for different velocity scaling factors are shown using a single mean and a single vertical bar representing the standard deviation. It is evident that for larger blade angles β the contribution of the drag becomes increasingly larger than the contribution of the lift. Only at blade angles smaller than $\beta < -10°$ the lift contributes more to propulsion than the drag.

EFFICIENCIES FOR DIFFERENT BLADE ANGLES

Figure 3.18 shows the impulse efficiency η_J and the energetic efficiency η_E, as defined in §3.1.5, for each combination of blade angle β and velocity scaling factor κ. Figure 3.18a

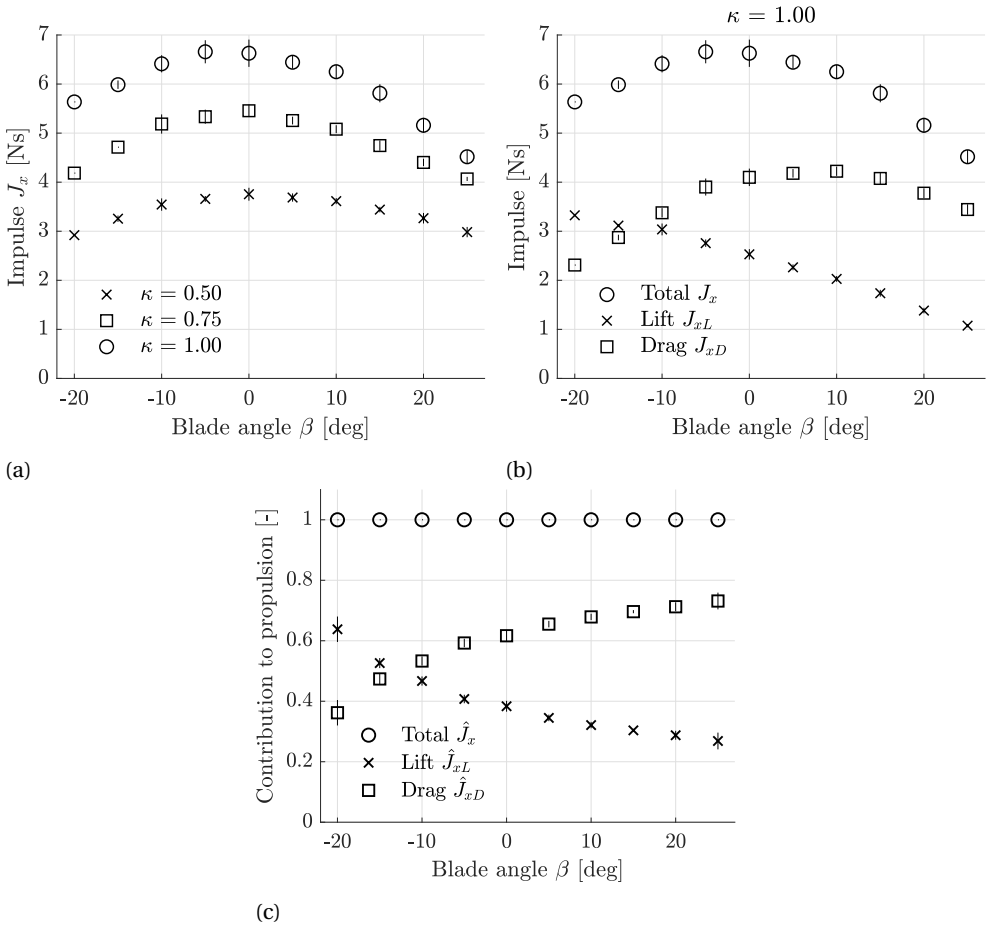

Figure 3.17: (a) The effectiveness J_x, i.e. the impulse generated in x-direction as a function of the blade angle β for different velocity scaling factors κ = 0.50, 0.75, and 1.00. (b) The contribution of the lift J_{xL} and drag J_{xD} to the total propulsive impulse J_x as a function of blade angle for κ = 1.00. (c) The relative contribution of the lift and drag to propulsion as a function of β for all velocity scaling factors κ. (all) The vertical bar in each marker indicates the standard deviation of the measurements.

shows that the impulse efficiency η_J is independent of velocity scaling factor κ. The maximum impulse efficiency η_J is found for $\beta \approx 15°$. At its maximum the impulse efficiency $\eta_J = 1$, which indicates that the impulse vector $\vec{J}$ is fully aligned with the propulsive direction x. This is a 19% increase over the standard case with $\eta_J = 0.84$.

Figure 3.18b shows that the energetic efficiency η_E reaches its maximum for a blade angle of 10°-15° for all velocity scaling factors κ. To illustrate the relative gain or loss in energetic efficiency for each blade angle β, compared to the standard case $\beta = 0°$, the normalised energetic efficiency is introduced as $\hat{\eta}_E = \eta_E/\eta_E(\beta = 0)$. $\hat{\eta}_E$ is plotted as a function of β and behaves identical for all κ, see figure 3.18c. The maximum increase of normalised energetic efficiency $\hat{\eta}_E$ is approximately 22% and occurs at a blade angle $\beta \approx$ 10-15°. Since normalisation collapses the energetic efficiency η_E for different scaling velocity factors κ on a single curve, it is reasonable to expect a scaling directly based on κ. From the scaling argument proposed in §3.4.2 it is expected that $\eta_E = J_x/E \sim \kappa^{-1}$ and indeed a similar scaling of $\eta_E \sim \kappa^{-0.7}$ is found in the experiments, see figure 3.18d.

FORCE SIGNALS FOR EFFECTIVE AND FOR EFFICIENT ROWING

The force signals of the most effective (standard) case $\beta = 0°$ and that of the most efficient case $\beta = 15°$ are shown in figure 3.19. Figure 3.19a compares the normal force component F_n and tangential force component F_t. The tangential component is close to zero throughout the drive for a blade angle $\beta = 15°$, while in the standard case ($\beta = 0°$), the tangential force is considerable. The normal component F_n as a function of t^* for the most efficient blade angle $\beta = 15°$ is very similar to the standard case throughout the drive phase, but is of slightly smaller magnitude in the first part of the drive phase $t^* < t_2^*$ and larger during the remainder of the drive phase. A notable difference is the small positive peak in the normal component F_n for $\beta = 15°$ at the beginning of the drive phase at $t^* = 0$.

In figure 3.19b the force signal is decomposed in a propulsive component F_x and non-propulsive component F_y. For a blade angle of $\beta = 15°$ it was shown that the impulse efficiency is $\eta_J = 1.00$, see section §3.4.4, which implies that the generated impulse vector is in the x-direction, such that $J_y = 0$. From figure 3.19b it is clear that integration of the non-propulsive component F_y over the drive phase duration would indeed yield zero for the case $\beta = 15°$, while this is clearly not the case for the standard case $\beta = 0°$ explaining the lower impulse efficiency for the standard case. For the case $\beta = 15°$, the propulsive component F_x is very similar to that of the standard case $\beta = 0°$. The values of F_x for $\beta = 15°$ are slightly lower for $t^* < t_2^*$ and larger for the remainder of the drive. A negative peak in propulsive component F_x can be observed for $\beta = 15°$ shortly after the catch at $t^* = 0$, which means negative propulsion, i.e. slowing down the boat.

The lift F_L and drag F_D for both the most efficient case $\beta = 15°$ and the standard case $\beta = 0°$ are shown in figure 3.19c. The lift for $\beta = 15°$ shows a clear negative peak right after the catch at $t^* = 0$. After the lift recovered from that peak it follows a profile similar to that of the lift for the standard case $\beta = 0°$. For the case $\beta = 15°$ the lift is lower throughout the drive phase, i.e. less positive and more negative than the lift for $\beta = 0°$. The drag for $\beta = 15°$ is smaller than that of $\beta = 0°$, except towards the end of the drive phase for $t_2^* < t^* < t_3^*$. During that stage the drag for $\beta = 15°$ decreases at a later moment in time than the drag for $\beta = 0°$. Although for the standard case $\beta = 0°$ significantly more drag F_D is produced during most of the drive phase, the drag contributing to propulsion F_{Dx} is very similar to

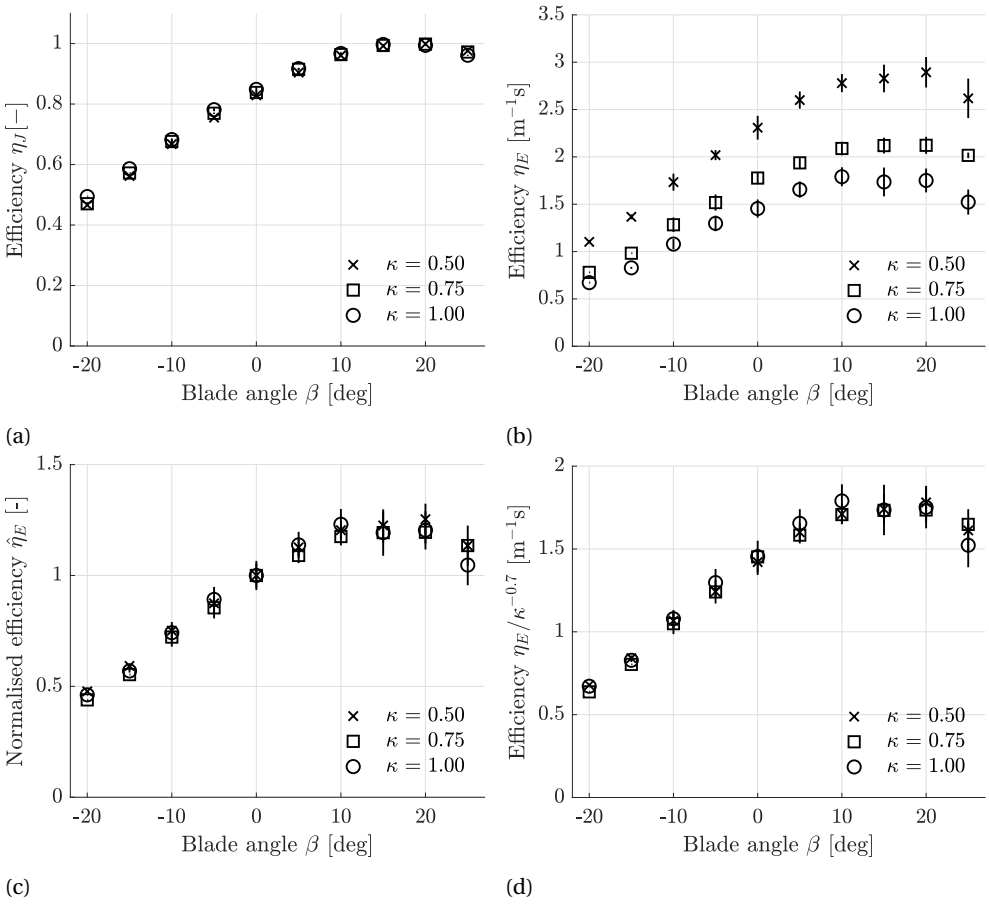

Figure 3.18: The efficiency of the drive phase as a function of the blade angle β for different velocity scaling factors κ. The markers represent the mean value of different measurements and the vertical solid lines represent the standard deviation. Both the impulse efficiency (a) and the energetic efficiency (b) show that a blade angle of $\beta \approx 15°$ is most efficient. (c) The energetic efficiency normalised by the energetic efficiency at $\beta = 0°$, i.e. $\hat{\eta}_E = \eta_E/\eta_E(\beta = 0°)$, for different velocity scaling factors κ. (d) The energetic efficiency η_E for different κ collapse when scaled with $1/\kappa^{-0.7}$.

that of $\beta = 15°$; see figure 3.19d. This implies that in the standard case a significant amount of impulse is generated that does not contribute to propulsion, which explains why the standard case $\beta = 0°$ is not most efficient. In the most efficient case $\beta = 15°$ the lift opposes propulsion (negative F_{Lx}) right after the release $t^* = 0$, while the lift in the standard case ($\beta = 0°$) does not contribute to propulsion at that stage, neither positively nor negatively. After the negative peak and up to t_2^* the lift of $\beta = 15°$ contributes less to propulsion than the standard case $\beta = 0°$, and vice versa after t_2^*.

THE FLOW FIELD FOR EFFICIENT ROWING

The flow field for the case $\beta = 15°$ was determined with PIV to explain why the measured forces for the maximum efficient blade angle $\beta = 15°$ differ from the standard case $\beta = 0°$. Figure 3.20 shows snapshots of the flow field taken at the same times as the snapshots of the flow fields for the standard case $\beta = 0°$. These times are also marked with vertical dashed lines in figure 3.19 to enable an easy comparison between the force signals and the flow field for the case $\beta = 15°$shown in figure 3.20.

Figure 3.20a shows the vorticity at time $t_1^* = 0.33$. The flow field looks quite different from that for the standard case $\beta = 0°$. Instead of a LEV at the convex side of the oar blade, a LEV is observed at the concave side of the oar blade (III). This LEV will generate lift opposite to the propulsive direction, which explains why less lift is generated than for $\beta = 0°$. This is also visible in the less pronounced vortex sheet (II). Also, a clockwise rotating vortex (I) is visible, which is absent in the flow field for the case $\beta = 0°$. This is likely to be a starting vortex of the lift event that caused the negative peak in the lift signal for $\beta = 15°$, which is possibly also related to the generation of the LEV (III). The evolution of the flow field shown in figure 3.20b is comparable to that of $\beta = 0°$. A vortex sheet is shed from the trailing edge and a LEV has formed (IV) at the convex side of the blade. Although the starting vortex (I) is still present in the field, it is too far away from the blade to significantly affect the forces on the blade. This explains why both lift and drag at this stage are very similar for the standard case $\beta = 0°$ and the most efficient case $\beta = 15°$. It appears that the trailing vortical structure (IV) for $\beta = 15°$ is less intense than for $\beta = 0°$. This means that the low pressure zone caused by the vortical structure for the standard case $\beta = 0°$ is stronger, thus explaining the slightly higher drag for the standard case at this stage. At time t_3^* the flow fields for the standard case $\beta = 0°$ and the most efficient case $\beta = 15°$ are qualitatively very similar. However, due to the increased blade angle the most efficient case $\beta = 15°$ is apparently better at generating lift, which in turn contributes to propulsion. Similar to the standard case $\beta = 0°$, upon extraction of the oar blade a second large vortex is formed (V), which together with the trailing vortical structure (IV) forms a vortex pair or a jet-like structure. Again the impulse vector $\vec{J}$ aligns with this vortex pair, in the sense that it is perpendicular to the line connecting the two vortex cores. The direction of the jet-like structure is directly related to the impulse efficiency η_J.

3.4.5. OAR DESIGN CONSIDERATIONS

This study shows that the direction of the impulse vector $\vec{J}$ must be aligned with the direction of motion for optimal propulsion. In practice this can be realised by a change of the blade angle β. Alternatively, optimal propulsion might also be realised by a change of the blade shape or blade camber or by other modifications. Since propulsion is not only

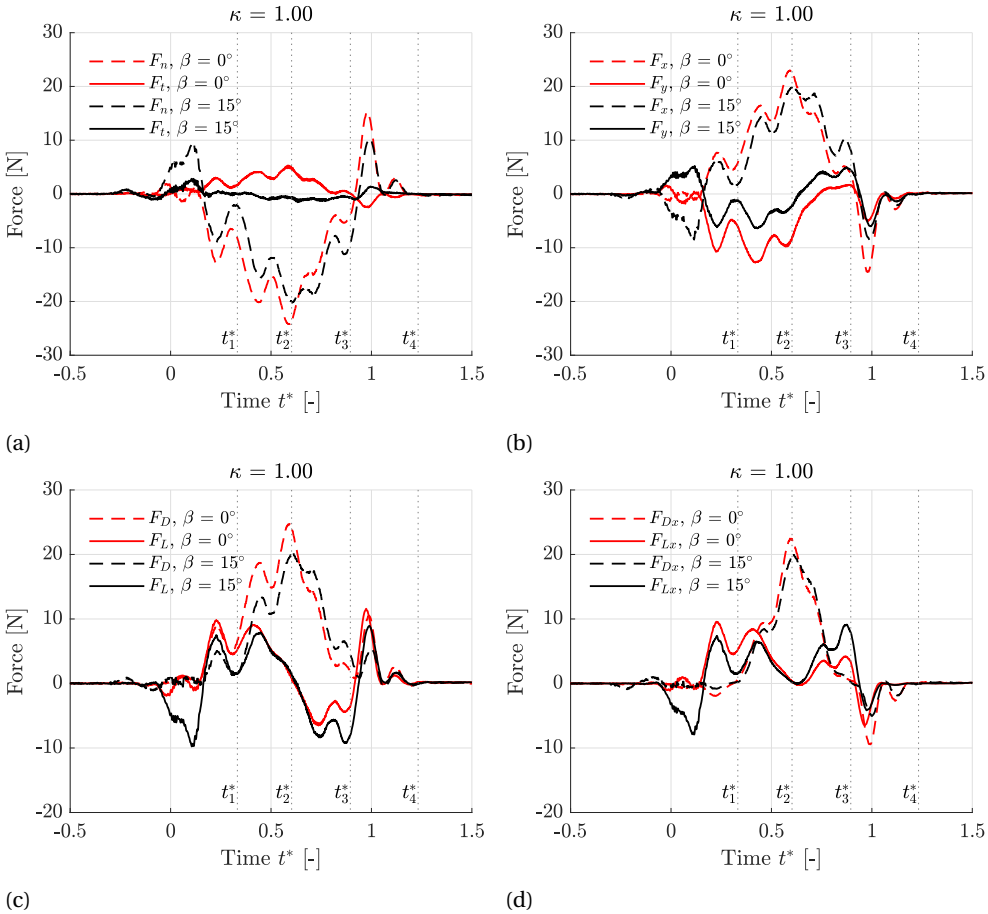

Figure 3.19: A comparison between most effective rowing, i.e. the standard case at a blade angle of $\beta = 0°$ (red), and most efficient rowing, i.e. at a blade angle of $\beta = 15°$ (black). (a) The normal and tangential force components F_n and F_t as a function of time t^*. (b) The propulsive and non-propulsive force components F_x and F_y as a function of time t^*. (c) The drag F_D and lift F_L as a function of time t^*. (d) The propulsion due to drag F_{Dx} and the propulsion due to lift F_{Lx} as a function of time t^*.

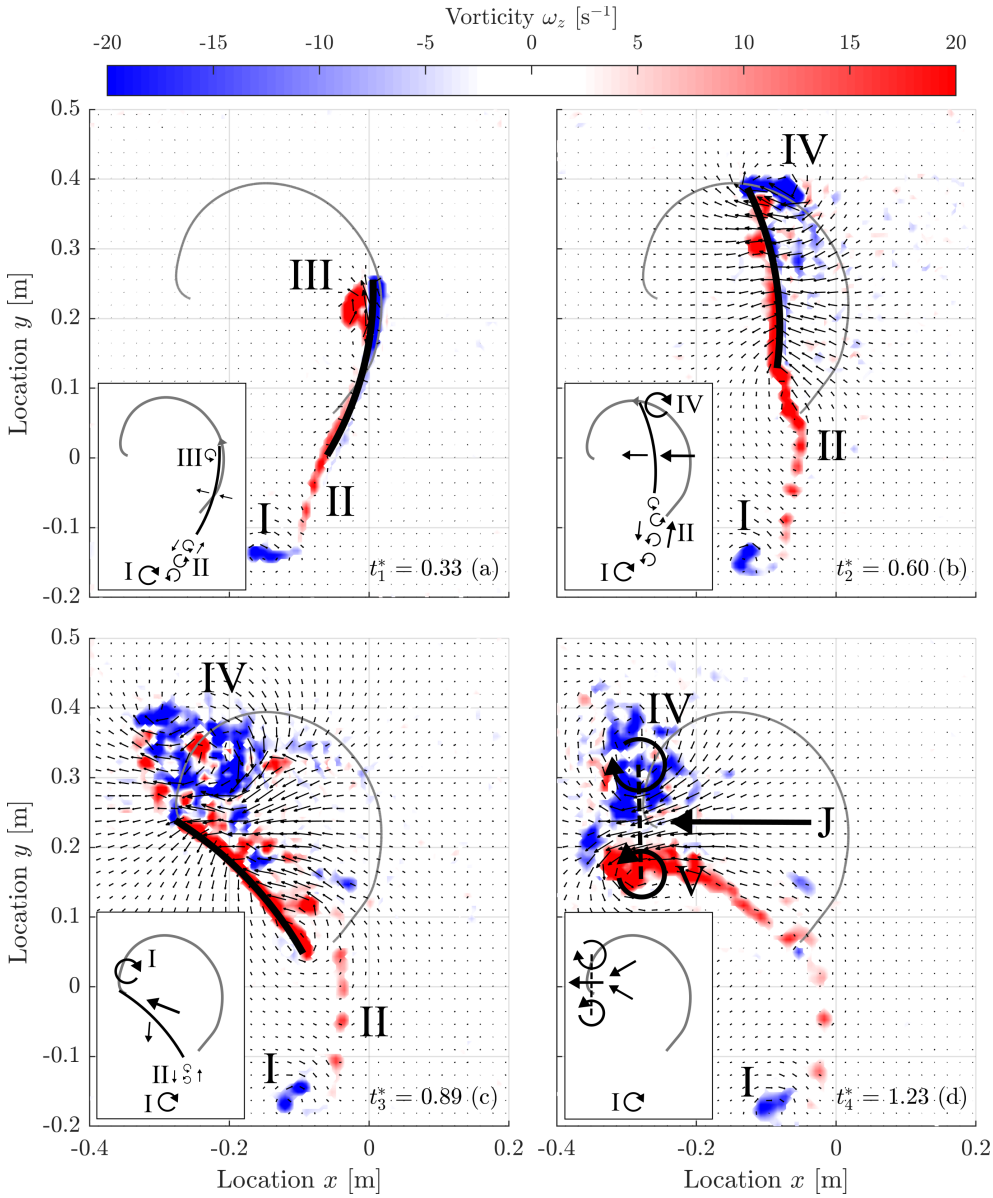

Figure 3.20: Snapshots of the velocity field (black arrows) and the vorticity (contours) for the selected times t_1^* to t_4^* as indicated in figure 3.19. The snapshots are taken at (a) the start of the drive phase $t_1^* = 0.33$, (b) in the middle of the drive phase $t_2^* = 0.60$, (c) just before the release $t_3^* = 0.89$ and (d) just after the release $t_4^* = 1.23$. The blade and blade path are shown as black and grey curve, respectively. In each snapshot an inset sketches the flow. A straight arrow indicates the flow direction and relative magnitude and the circular arrows indicate vortical structures. Roman numeral I indicates a starting vortex, II a vortex sheet, and III and IV a leading edge vortex. In (d) a vortex pair IV-V and the impulse vector $\vec{J}$ are shown. The trailing-edge vortex layer rolls up in a vortex with opposite circulation than the LEV, so that they form a vortex pair that propels itself to the left. A jet-type of flow is generated more or less in negative x-direction, an indication of propulsion.

driven by drag but for a significant part also by lift, it would be interesting to further investigate the lift generation of differently shaped oar blades. Special attention should be paid to the generation of leading edge vortices. These should be generated at the propulsion enhancing side of the blade and early in the drive phase. Since the leading edge vortex evolves into a drag-enhancing trailing vortical structure during drag phase of the drive it is important to keep the LEV close to the blade.

Negative oar blade angles $\beta < 0$ should be avoided because both effectiveness and efficiency decrease. However, oars have a finite stiffness and when loaded during the drive phase bend towards $\beta < 0°$, thus reducing the blade angle. This suggests that stiffer oars currently have a direct advantage over less-stiff oars, especially since the deformation of oars can be significant [12].

3.4.6. ROWING FASTER

In practice, the athletes that perform the rowing motion are no robots and so-far the human factor has not been touched upon in this study. Although this human factor is beyond the expertise of the authors, we make an estimate of the (theoretical) implications of our findings for actual on-water rowing. Athletes are not limited by preprogrammed kinematics such as our robot, but are limited by the work they can perform, which also formed the basis for the definition of the energetic efficiency in §3.1.5. Figure 3.18c shows that the increase in energetic efficiency η_E is 20% at optimal blade angle $\beta = 10°$. Therefore, with the same amount of work performed, an athlete could generate 20% more propulsion. To increase the energy athletes can increase the blade velocity, which in turn decreases the energetic efficiency as is evident from figure 3.18b. The work performed using a standard oar blade angle $\beta = 0°$ is 30% higher than when using the optimal oar blade angle ($\beta = 15°$). To match the work performed using the optimal configuration the blade velocity must increase with 14%, under the fair assumption that $E \sim V^2$. The scaling of the energetic efficiency with respect to κ as in $\eta_E \sim \kappa^{-0.7}$ yields a propulsion of $1.20 \times 1.14^{-0.7}$=1.095, which is a 9.5% increase over the propulsion for $\beta = 0°$. In a sport where finish times are within tenths of seconds over a race lasting several minutes this would have a tremendous effect on the outcome of a race. Even if it is assumed that $\eta_E \sim \kappa^{-1}$ an increase in propulsion of 5% is obtained. We hypothesise that alternatively, athletes could increase the blade efficiency by using a blade angle $\beta = 15°$ in combination with larger oar blades (which have a larger surface area), possibly avoiding the penalty on the energetic efficiency by increasing the blade velocity.

3.5. CONCLUSION

An experimental set-up has been built that can accurately reproduce the complex and unsteady motion of the rowing oar during the drive phase of rowing, and is able to capture the associated hydrodynamics by simultaneous PIV and force measurements. During the first and last part of the drive phase the generated lift contributes to the propulsion, and the generation of leading edge vortices can increase lift and thus propulsion. During the middle part of the drive phase the propulsion is dominated by drag, which could be increased by trailing vortical structures which are effectively evolved leading edge vortices. For the standard case ($\beta = 0°$), the propulsion generated during the drive phase due to lift

and drag is 40% and 60%, respectively. The flow appears to be independent of velocity scaling for $\kappa > 0.5$, which suggests Reynolds independent scaling, i.e. as long as the flow is 'turbulent enough' its behaviour is reproduced.

The performance of the rowing motion during the drive phase has been quantified using the effectiveness J_x, the impulse efficiency η_J and the energetic efficiency η_E. The effect of varying the rowing oar blade angle β on the efficiency and effectiveness was studied. It is found that the standard configuration with oar blade angle $\beta = 0°$ is most effective and that the configuration with an oar blade angle of β = 10°-15° is most efficient. The change in oar angle to obtain maximum efficiency is intuitively correct. Since the oar normally operates in the angular segment of $-50° \leq \theta \leq 30°$, see figure 3.4b, the average oar orientation is $-10°$. A 10° shift of the oar blade orientation thus aligns the oar blade such that on average it is perpendicular to the direction of motion of the boat. The 10° shift of the blade angle is close to the 15° blade angle which is found to be most efficient. For the most efficient case $\beta = 15°$, most propulsion is generated by means of drag (70%), contrary to popular belief that lift in rowing would be more dominant.

ACKNOWLEDGEMENTS

This work is part of the research programme 'Optimisation of propulsion in and over water' with project number 12868, which is (partly) financed by the Netherlands Organisation for Scientific Research (NWO).

DECLARATION OF INTERESTS

The authors report no conflict of interest.

REFERENCES

[1] ADRIAN, R. J. & WESTERWEEL, J. 2011 *Particle image velocimetry*. Cambridge University Press.

[2] ANDERSON, J. D. 1991 *Fundamentals of Aerodynamics (Mcgraw-Hill Series in Aeronautical and Aerospace Engineering)*. Mcgraw-Hill College.

[3] BARRÉ, S. & KOBUS, J. M. 2010 Comparison between common models of forces on oar blades and forces measured by towing tank tests. *Proceedings of the Institution of Mechanical Engineers, Part P: Journal of Sports Engineering and Technology* **224** (1), 37–50.

[4] BIRCH, J. M. & DICKINSON, M. H. 2001 Spanwise flow and the attachment of the leading-edge vortex on insect wings. *Nature* **412** (6848), 729–733.

[5] CAPLAN, N. & GARDNER, T. N. 2007 A fluid dynamic investigation of the Big Blade and Macon oar blade designs in rowing propulsion. *Journal of Sports Sciences* **25** (6), 643–650.

[6] COPPEL, A., GARDNER, T. N., CAPLAN, N. & HARGREAVES, D. M. 2010 Simulating the fluid dynamic behaviour of oar blades in competition rowing. *Proceedings of the*

Institution of Mechanical Engineers, Part P: Journal of Sports Engineering and Technology **224** (1), 25–35.

[7] DICKINSON, M. H. & GÖTZ, K. G. 1993 Unsteady Aerodynamic Performance of Model Wings at Low Reynolds Numbers. *Journal of Experimental Biology* **174** (1), 45–64.

[8] ELDREDGE, J. & WANG, C. 2010 High-fidelity simulations and low-order modeling of a rapidly pitching plate. In *40th Fluid Dynamics Conference and Exhibit*. American Institute of Aeronautics and Astronautics.

[9] ELDREDGE, J. D. & JONES, A. R. 2019 Leading-edge vortices: mechanics and modeling. *Annual Review of Fluid Mechanics* **51**, 75–104.

[10] GHARIB, M., RAMBOD, E. & SHARIFF, K. 1998 A universal time scale for vortex ring formation. *Journal of Fluid Mechanics* **360**, 121–140.

[11] GRIFT, E. J., VIJAYARAGAVAN, N. B., TUMMERS, M. J. & WESTERWEEL, J. 2019 Drag force on an accelerating submerged plate. *Journal of Fluid Mechanics* **866** (369-398).

[12] HOFMIJSTER, M., KONING, J. DE & SOEST, A. J. VAN 2010 Estimation of the energy loss at the blades in rowing: Common assumptions revisited. *Journal of Sports Sciences* **28** (10), 1093–1102.

[13] VAN HOUWELINGEN, J., ANTWERPEN, R. M., HOLTEN, A. P. C., GRIFT, E. J., WESTERWEEL, J. & CLERCX, H. J. H. 2018 Automated led tracking to measure instantaneous velocities in swimming. *Sports Engineering* **21** (4), 419–427.

[14] LABBÉ, R., BOUCHER, J.-P., CLANET, C. & BENZAQUEN, M. 2019 Physics of rowing oars. *New Journal of Physics* **21** (9), 093050.

[15] LEROYER, A., BARRÉ, S., KOBUS, J. M. & VISONNEAU, M. 2010 Influence of free surface, unsteadiness and viscous effects on oar blade hydrodynamic loads. *Journal of Sports Sciences* **28** (12), 1287–1298.

[16] LI, J. & WU, Z.-N. 2015 Unsteady lift for the Wagner problem in the presence of additional leading/trailing edge vortices. *Journal of Fluid Mechanics* **769**, 182–217.

[17] LUFF, J. D., DROUILLARD, T., ROMPAGE, A. M., LINNE, M. A. & HERTZBERG, J. R. 1999 Experimental uncertainties associated with particle image velocimetry (PIV) based vorticity algorithms. *Experiments in Fluids* **26** (1-2), 36–54.

[18] PATTON, K. T. 1965 An experimental investigation of hydrodynamic mass and mechanical impedances. PhD thesis, 1979, MS Thesis, Univ. of Rhode Island.

[19] PULLIN, D. I. & WANG, Z. JANE 2004 Unsteady forces on an accelerating plate and application to hovering insect flight. *Journal of Fluid Mechanics* **509**, 1–21.

[20] RINGUETTE, M. J., MILANO, M. & GHARIB, M. 2007 Role of the tip vortex in the force generation of low-aspect-ratio normal flat plates. *Journal of Fluid Mechanics* **581**, 453–468.

[21] ROBERT, Y., LEROYER, A., BARRÉ, S., RONGÈRE, F., QUEUTEY, P. & VISONNEAU, M. 2014 Fluid Mechanics in Rowing: The Case of the Flow Around the Blades. *Procedia Engineering* **72**, 744–749.

[22] SLIASAS, A. & TULLIS, S. 2009 Numerical modelling of rowing blade hydrodynamics. *Sports Engineering* **12** (1), 31.

[23] SOPER, C. & HUME, PATRIA A. 2004 Towards an Ideal Rowing Technique for Performance. *Sports Medicine* **34** (12), 825–848.

[24] URBAN, S., LEITLOFF, J. & HINZ, S. 2015 Improved wide-angle, fisheye and omnidirectional camera calibration. *ISPRS Journal of Photogrammetry and Remote Sensing* **108**, 72–79.

[25] WAGNER, H. 1925 Über die Entstehung des dynamischen Auftriebes von Tragflügeln. *ZAMM - Journal of Applied Mathematics and Mechanics / Zeitschrift für Angewandte Mathematik und Mechanik* **5** (1), 17–35.

[26] WEST, G. S. & APELT, C. J. 1982 The effects of tunnel blockage and aspect ratio on the mean flow past a circular cylinder with Reynolds numbers between 10^4 and 10^5. *Journal of Fluid Mechanics* **114**, 361–377.

[27] XU, L. & NITSCHE, M. 2015 Start-up vortex flow past an accelerated flat plate. *Physics of Fluids* **27** (3), 033602.

[28] YU, Y. T. 1945 Virtual masses of rectangular plates and parallelepipeds in water. *Journal of Applied Physics* **16** (11), 724–729.

4

CONCLUSION AND DISCUSSION

In this chapter an overview of the findings in this thesis is presented and the research objectives set in chapter 1 are reflected upon. It is discussed how these findings can be translated from laboratory to on-water rowing. Finally, some suggestions for future research are provided.

Parts of this conclusion and discussion are taken from chapter 2 and 3.

4.1. THE EXPERIMENTAL SET-UP - 'THE ROWBOT'

In this thesis various experiments were performed, all using an industrial robot (the 'RowBot') to generate (complex) accelerating flows around an object. While the industrial robot manipulated the object, concurrent force and PIV measurements were performed to link the hydrodynamic force acting on the object to the flow velocity field around the object.

The robot used in this thesis proves to be a valuable asset for investigating accelerating flows. Between different experiments no significant hardware changes have to be made to facilitate different motions (to a maximum of four degrees of freedom, see Appendix A). The strut and object are easily bolted to the robot head, and learning to program the robot motion takes approximately one week. The robot is therefore versatile, robust, ready-to-use for new experiments in a matter of hours, and provides the opportunity to study flows around objects that move in multiple degrees of freedom; a topic that can hardly be studied in flume tanks, towing tanks, wind tunnels, or water tunnels.

During the experiments presented in this thesis, the potential of the robot was not fully leveraged. Since the robot programs are easy to adapt, all parameter studies have been carried out by manually setting the parameters in the program of the robot and manually executing each adapted program. The industrial robot comes with a series of (digital) input and output ports that allow for automated control by a PC. By coupling the measurement PC, that also triggers the PIV measurements and logs the force measurements, a fully automated experimental set-up can be created. By doing so, human error can be minimised (manually changing programs is prone to error), and the number of runs per unit time can be increased, while decreasing the human workload. This makes the set-up very suitable to do large parameter studies, e.g. studying the drag on an accelerating flat plate for a large number of combinations of plate acceleration, plate depth, plate angle, and plate pitch, while carrying out each experiment multiple times to reduce the standard error.

4.2. THE DRAG FORCE ON AN ACCELERATING PLATE

In chapter 2, the drag on a flat plate accelerating towards a constant target velocity is presented. The force due to added mass appears to become larger over time at constant acceleration. As a consequence, the widely reported added mass coefficients for a rectangular plate should only be used for small motions, i.e. motions much less than one plate width. It is proposed to model the added mass for prolonged accelerations using the *entrainment rate*, i.e. the rate at which mass is entrained into the accelerating wake. It is found that the depth at which the plate is submerged affects the drag on the plate at its constant target velocity. A maximum drag is found for a plate that is submerged 1/5th of the plate height below the surface. When the plate is submerged at this depth, a large vortical structure continues to trail the plate, well after the plate has reached its constant target velocity. At the other tested depths a vortical structure is not observed during that stage. A non-dimensional time that is effectively the number of plate heights travelled after reaching the plate target velocity, appears to be a universal time scale for which the force profiles for different accelerations and velocities collapse.

The experiments were carried out with a plate of fixed size, with an aspect ratio of $AR = 2$. Although it is expected that for plates of comparable aspect ratios similar behaviour

is found at similar Reynolds numbers, it is unknown what effect the plate aspect ratio exactly has, or what effect the fluid properties have, such as viscosity or surface tension. For extreme cases one could expect different behaviour, e.g. a combination of motion and fluid properties that causes cavitation. The shape of the plate, e.g. its aspect ratio and symmetry, are expected to affect the formation of the trailing vortical structure during acceleration of the plate.

4.2.1. THE STARTING STROKE OF A RACE IN COMPETITIVE ROWING

The accelerating flat plate presented in chapter 2 is thought to be analogues to the starting stroke of a race in competitive rowing, because both the geometry and kinematics used in the experiments are comparable to that of a starting stroke during actual rowing.

The major dimensions of the plate used in the experiments, i.e. its height, width, and thickness, are similar to that of a rowing oar blade, although scaled with a factor of 0.5. An actual rowing oar blade has a (slightly) doubly curved surface, while the plate used in the experiment is flat. Both the oar blade during the starting stroke and the plate during the experiment move along their path perpendicular to their major dimensions; the oar is mounted on a pivot point attached to the hull, which during the first stroke has very little velocity (the boat starts from standstill). Therefore, it is expected that the observed flow phenomena are similar for a flat plate or for a plate with a (slightly) doubly curved surface, although the actual drag coefficient may vary, as is found for cupped disks (hollow semi-sphere) versus flat disks by e.g. Prandtl & Betz [1]. Lastly, the plate in the experiment and the oar blade both accelerate from standstill and move over a distance of approximately 10 times the blade/plate height. Although the exact kinematics of a starting stroke are unknown, it is reasonable to accept that the kinematics will be similar to the kinematics used in the experiment with the flat plate; at the start an oar blade starts from standstill, and since the force an athlete can exert is finite, also the velocity achieved during the first stroke is finite.

On the stated premise that the flow phenomena for both the experiment and a starting stroke during actual rowing are similar, the findings of the experiment can be used to obtain a best practice for a starting stroke during actual rowing. The most effective starting stroke is the stroke that generates maximum drag, whereas efficient rowing means reducing the slip velocity, i.e. the velocity of the oar blade with respect to the water. Based on the experiments athletes should: (1) slightly submerge their rowing oar blades (1/5th of the blade height) as was found during the experiments, to maximise drag; (2) apply full force at the start signal as to obtain maximum acceleration, and therefore maximum drag, and: (3) keep strokes relatively short as to limit the stroke length to the acceleration phase of the stroke, since in the acceleration phase the generated drag is high, and the slip velocity is low compared to the phase of constant velocity that comes after the acceleration phase. Obviously, this best practice holds from a (simplified) hydrodynamic perspective, and further research into the athlete capabilities and the use of further refined geometries and kinematics is required to validate this best practice.

4.3. THE HYDRODYNAMICS OF REALISTIC ROWING

In chapter 3, the hydrodynamics of realistic rowing are presented. The kinematics during actual on-water rowing were captured and programmed into an industrial robot (the RowBot) to replicate the kinematics on a 1:2 scale in an open-top water tank, see appendix A. Also a 1:2 scale oar blade model was fabricated (3D-printed and reinforced with carbon fibre). The motion of the oar blade in water produced by the experimental set-up looks realistic; both in the generated motion as in the resulting characteristic vortex pair visible at the surface after a stroke. For this research the recorded kinematics of a single stroke was used, which is thought to be representative enough to investigate the hydrodynamics in rowing and to determine how to optimise performance. Obviously, in reality strokes vary depending on many things, such as the boat type, the athlete (e.g. build, performance, fitness), rowing speeds, and outdoor conditions (e.g. weather, waves, water currents).

During the experiments the geometry of the oar blade model and the oar blade path was fixed at a 0.5 scale, while the velocity was varied between experimental runs. From the experiments it is found that for all tested velocities (except for very low velocity) the flow features were very similar, indicating that a Reynolds independent regime is reached. Therefore, it is assumed that the results observed during the experiments (at $Re \approx 0.82\times10^5$ to 1.64×10^5) hold for actual rowing as well, even though the geometry is larger and the velocities are higher, resulting in a higher Reynolds number ($Re \approx 6.57\times10^5$).

During the experiments the hydrodynamic forces were measured using a 6 degrees of freedom (DOF) force/ torque transducer and the flow field was measured using particle image velocimetry.

4.3.1. FLOW PHENOMENA DRIVING PROPULSION

From the force measurements and flow field measurements using particle image velocimetry it is found that both lift and drag contribute to propulsion during rowing; see figure 3.16. For the selected kinematics 60% of the generated propulsion was due to drag, while 40% was due to lift. Propulsion during the start and end of the drive phase are primarily due to lift, while during the middle of the stroke, when the oar is more or less perpendicular to the boat, the generation of propulsion is primarily due to drag. At the start of the drive phase a leading edge vortex (LEV) is generated (contributing to the lift), which develops in a trailing vortical structure (contributing to the drag) during the middle part of the drive phase. During the release, at the end of the drive phase, this trailing vortical structure evolves into a jet-like structure that shows as a vortex pair at the surface and is relatively long-lived.

4.3.2. MEASURING THE HYDRODYNAMIC PERFORMANCE OF A ROWING OAR BLADE

It was found that the hydrodynamic performance of a single stroke can be expressed in terms of both efficiency and effectiveness. Since the main purpose of competitive rowing is to row faster, effectiveness (i.e. fulfilling the purpose) is defined as the amount of propulsive impulse that is produced during a single stroke, which is derived from the force/ torque measurements.

To obtain insight in the hydrodynamic efficiency, the impulse generated in propul-

sive direction J_x is compared to the total impulse generated $|\vec{J}|$; any impulse generated in a direction other than the propulsive direction is thought to be undesirable. It was found that for the tested stroke, at all tested velocities the generated impulse efficiency $\eta_J = J_x/|\vec{J}| = 0.84$ and the total generated impulse was directed approximately 30° away from the propulsive direction, which implies that rowing propulsion could be more efficient. The jet-like structure observed in the flow field after the release appears to have a similar angle. The impulse efficiency η_J appears to be Reynolds independent, and it is conjectured that a similar efficiency would be found if these experiments would have been carried out at full scale.

Since athletes are limited in the power they can deliver, and as a consequence the energy they can spend during a single stroke, it is interesting to define a hydrodynamic efficiency as propulsive impulse per unit energy[1] $\eta_E = J_x/E$. The work performed (the energy) during the drive phase is derived from the force/ torque measurements and kinematics. For increasing velocities the energetic efficiency η_E becomes smaller as is expected from the scaling argument $J_x \sim V$ and $E \sim V^2$, ergo $\eta_E \sim V^{-1}$.

4.3.3. OPTIMISATION OF THE ROWING OAR BLADE

The angle to which the oar blade is mounted on the shaft was varied around the vertical axis from β = -20° (blade tip towards the bow) to β = 25 ° (blade tip towards the stern). The kinematics and blade path were held constant, and the maximum effectiveness η_J is found for β = 0°. However, the optimal impulse efficiency η_J and energetic efficiency η_E are found for a blade angle β = 15°. At this angle the total generated impulse is fully aligned in the propulsive direction. If it is assumed that the athlete can perform the same amount of work as for a blade angle β = 0° by increasing the oar blade velocity, the generated propulsive impulse is 5% to 9.5% larger at a blade angle of β = 15° compared to a blade angle of β = 0°.

For a blade angle of β = 15° the jet-like structure appears to be aligned with the propulsive direction suggesting that during actual rowing the vortex pair visible at the surface can be used as an indicator to determine the hydrodynamic efficiency. In practice it might prove feasible to increase the oar blade size or to increase the length of the oar shaft in order to leverage the gain in efficiency and achieve maximum effectiveness.

4.4. RECOMMENDATIONS FOR FUTURE RESEARCH

In extension of chapter 2 it would be interesting to investigate the effect of symmetry and aspect ratio on the generation of the initial vortical structure trailing the flat plate during the acceleration phase and its effect on drag. Instead of starting from standstill and constant acceleration towards a constant velocity, it is of interest to investigate the effect of different velocity profiles, e.g. what happens at a gradual transition from acceleration to constant velocity. To obtain a more robust answer to what is the best practice during the start in actual rowing the experiment could be repeated by using kinematics of a starting stroke and the oar blade model used in chapter 3.

In chapter 3 the experiments were limited to the kinematics of one single stroke. It

[1] Note that this is the mechanical energy following from equation 3.4 and is not to be confused with the energy consumed by the athlete (metabolic cost).

is recommendable to investigate strokes of various boat types, athletes, during various weather conditions and using different oar shaft lengths, since these may affect the oar blade kinematics, e.g. see figure 3.4. The blade angle can then be optimally adjusted depending on the circumstances and race strategy.

By selecting strokes spanning a well-defined parameter space the main drivers for hydrodynamic efficiency and effectiveness can be determined, aiding the optimisation process. Though it appears that the observed flow features are Reynolds independent, the generation of vortices is evidently linked to viscosity; this makes varying the viscosity an interesting experiment. To move away from solely hydrodynamic optimisation, a physiological model (perhaps personalised per athlete) can be incorporated in the optimisation process to ensure that the optimised rowing propulsion can be executed by the athlete in terms of motion, power and force. Since the parameter space is expected to be vast, it is highly recommended to further investigate the further automation of experiments; first of all to increase the number of experiments carried out per unit time, and secondly to diminish human error/ variation.

Lastly, to investigate whether the optimisation of rowing propulsion by changing the oar blade angle β is feasible, it is recommended to continue testing this in practice during actual rowing. By varying the oar blade angles over a similar range as is done in this research, and filming the vortex pairs generated during the release of each stroke that are visible at the surface, the effect can be determined.

REFERENCES

[1] PRANDTL, L. & BETZ, A., ed. 2009 *Ergebnisse der Aerodynamischen Versuchsanstalt zu Göttingen - IV. Lieferung*, *Göttinger Klassiker der Strömungsmechanik*, vol. 007. Göttingen: Universitätsverlag Göttingen.

A

THE ROWBOT

A more detailed description of the industrial robot (the 'RowBot') used in the experiments presented in chapter 2 and 3.

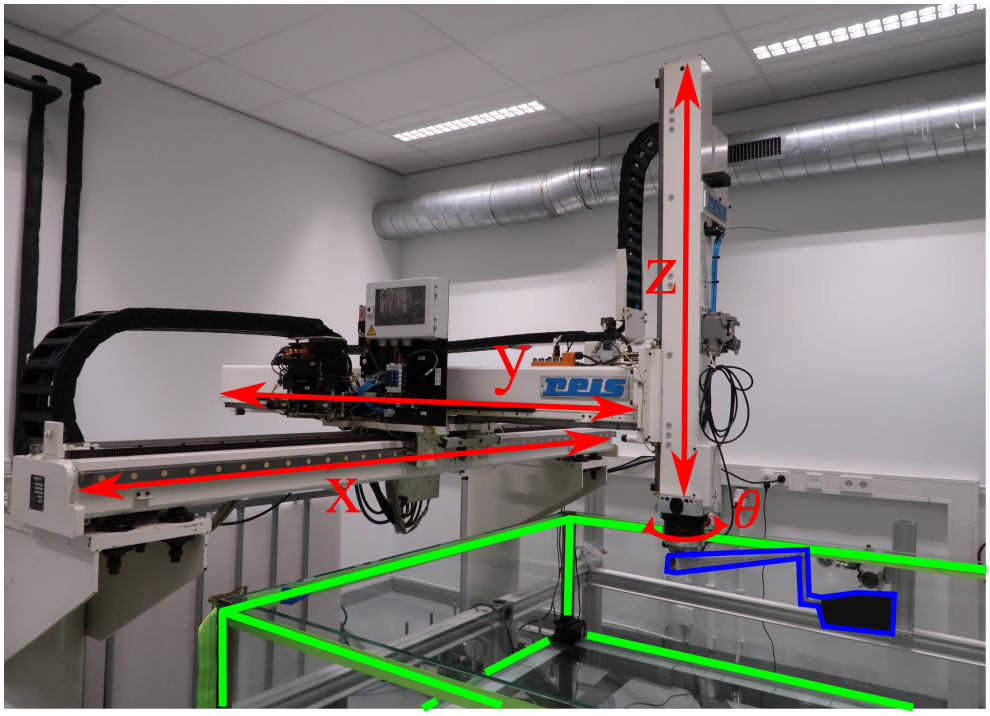

Figure A.1: The RowBot, an industrial robot with four axes of motion (red); a translating motion in X, Y, and Z and a rotational motion θ around the Z-axis. A model (blue) is attached to the robot head so that a flow can be generated in the tank (green) that is placed underneath the robot. The motion range in X, Y, and Z is 2.50 m, 1.51 m, and 0.53 m (limited by the tank depth), respectively

A.1. THE EXPERIMENTAL SET-UP - THE RO(W)BOT

The experiments discussed in chapter 2 and 3 are performed using the same experimental set-up. The experimental set-up used in each chapter consists out of three parts: (i) the robot that generates the flow by manipulating an oar blade model attached to the robot; (ii) the tank which holds the water in which the flow is generated, and (iii) the various measurement devices. The experiments are performed in a controlled environment kept at a constant temperature of 20°C.

The oar blade models are moved through the water by a four-axis industrial robot dubbed: 'The RowBot', see figure A.1. The robot head can perform a translational motion over its three axes: X, Y and Z, and can perform a rotational motion θ around the vertical axis of the robot head (aligned with Z). A combined motion over these four axes is required to replicate a realistic rowing motion.

A.1.1. MOTIVATION FOR AN INDUSTRIAL GANTRY ROBOT

The rowing motion is challenging to replicate in a laboratory environment due to its high accelerations $\mathcal{O}(1\ \mathrm{ms}^{-2})$, high velocities $\mathcal{O}(1\ \mathrm{ms}^{-1})$, and a geometric scale in the order of $\mathcal{O}(1\ \mathrm{m})$. Since the scaling behaviour of the flow was not known a priori it was desirable to

replicate the rowing motion as close to full scale as possible. To produce a realistic motion in a controlled environment three options were identified. Firstly, we could mount a rowing oar on a towing tank carriage where the towing tank simulates the hull motion and the oar pivots around an axis fixed to this carriage, similar to Barré & Kobus [1]. However, to create a realistic motion some custom-built system that replicates the catch and release is also needed. The downside of this system is the very large inertia of the towing tank carriage severely limiting a realistic replication of the deceleration and acceleration of the boat hull. Also the time between experiments, i.e. for the water to become still again, is very long. Furthermore, the towing tank at TU Delft is in high demand and available for only a limited amount of time. A second option is a custom-built device that replicates the motion of the oar blade through the water. However, it became apparent that a system able to produce the required velocities and accelerations, with the needed range, would be very costly, even when the kinematics were scaled by a factor 0.5. The third option, which is the option of choice, is an industrial robot. The advantage of an industrial robot is that it is versatile, cost-effective, well-documented, robust, and relatively easy to use. The particular type of industrial robot chosen uses linear axis perpendicular to each other and is therefore called a Cartesian coordinate robot or a gantry robot. The most well-known type of industrial robot, the articulated robots or robot arm, often provides six degrees of freedom, but they are limited to lower velocities and accelerations, because the motors in the robot carry the weight of all motors and joints further down the arm. Since only four axes of motion, i.e. X, Y, Z, and θ, are needed to replicate the rowing motion a higher velocity and acceleration were chosen instead of two more degrees of freedom; although the latter would make the RowBot more versatile.

A.1.2. THE ROWBOT IN MORE DETAIL

The robot of choice is a Reis Robotics RL50. Its range in X, Y, and Z is 2.5 m, 1.5 m, and 1.25 m, respectively. The robot head can rotate 720° and the maximum axis velocity is 2.8 ms^{-1} while the maximum axis acceleration is in excess of 1.6 ms^{-2}, depending on the combined motion of the axes. The choice for the range of the robot is limited by the size of the laboratory and in turn limits the maximum achievable velocity, since the robot needs some distance to accelerate. The robot accelerations are determined by the maximum power of the electric engines and the weight of the robot. Both the maximum acceleration and velocity were increased beyond the factory standard by a certified and specialised commercial party, sacrificing durability of the RowBot for acceleration and velocity; since the number of cycles a robot performs in the present laboratory setting is a fraction of the number of cycles in a production environment this has no negative consequences in practice. The maximum mass that can be attached to the robot head without loss of performance is 50 kg. The forces generated by the models moving through the water are very small compared to the inertia forces due to this maximum weight of approximately 500 N, and thus have no effect on the performance of the robot. The repeatability of the robot motion is 0.1 mm, which is very small relative to the rowing motion $\mathcal{O}$(1 m).

The robot is running the ROBOTstarV operating system. Via the teach pendant, i.e. a remote control attached to the robot, a routine is written in a vendor specific procedural programming language providing the movement instructions for the robot. The robot performs the motion programmed in the routine only when that specific routine is exe-

cuted by the robot operator. During the execution of the routine that contains the desired kinematics, an internal processor calculates the required power for the electric engines in real-time, based on a robot model that contains the inertia of all moving parts, and the operating system subsequently controls the motor drivers that move the robot head. The calculated position and actual position do not match exactly since model and reality never exactly match. The robot constantly checks the realised position and when the actual position differs too much from the predicted position (a few millimetres) the robot activates its emergency brake, thus ensuring that the robot does not behave in an unpredictable manner.

A.1.3. PROGRAMMING THE OAR BLADE PATH

Programming a path for the robot is not trivial. Instead of a series of positions as function of time, target positions are provided sequentially with in between the target positions the instructions on how to reach the next target location. Instructions on how to reach the next target position include the target velocity before reaching each target position, what the maximum allowed acceleration is to achieve that velocity and the movement mode that describes the shape of the path that the robot uses to reach the next position: e.g. linear (in a straight line) or via a spline (Bézier curve). Not in all movement modes the robot attempts to pass exactly through the target coordinate; to prevent the axis from slowing down too much to reach a certain position the robot uses a fly-by radius which can be set as desired. A small radius ensures the robot approximates the target positions very well, but might prevent the robot to get up to full speed. A larger radius means a coarser approximation, but enables the robot to move faster.

In this study the spline movement mode is used with a small fly-by radius ensuring a very good approximation of the programmed path while the desired velocity was still achieved. In between points only a single constant target velocity and acceleration can be set meaning that the robot will follow a trapezoidal velocity profile between points. However, to approximate an otherwise smooth velocity profile a large amount of target positions can be used. However, the robot is only able to read points ahead at a certain rate, so too many points will cause the robot to slow down such that it has enough time to read future positions. All in all, the process of programming a routine such that the desired path is followed in both space and time is an extensive process of trial and error.

The main structure of a program contains lines that either prescribe the target velocity along the path, maximum allowed acceleration along the path, or the target position in Cartesian coordinates and robot head rotation, for example:

1. Position [X = 100 mm, Y = 200 mm, Z = -50 mm, Theta = 360°]
2. Acceleration = 20%
3. Velocity = 1000 mms^{-1}
4. Position [X = 200 mm, Y = 400 mm, Z = -50 mm, Theta = 360°]
5. Acceleration = 10%
6. Velocity = 800 mms^{-1}
7. Position [X = 1200 mm, Y = 460 mm, Z = -0 mm, Theta = 360°]
8. Acceleration = 100%
9. Velocity = 800 mms^{-1}
10. Position [X = 1400 mm, Y = 420 mm, Z = -150 mm, Theta = 360°]

11. etc...

The acceleration can be set at a maximum of 200% that corresponds to 1.62 ms^{-2}, the velocity is set in mms^{-1}, the target position in Cartesian coordinates in mm, and the rotation of the robot head in degree.

REFERENCES

[1] BARRÉ, S. & KOBUS, J. M. 2010 Comparison between common models of forces on oar blades and forces measured by towing tank tests. *Proceedings of the Institution of Mechanical Engineers, Part P: Journal of Sports Engineering and Technology* **224** (1), 37–50.

B

VALIDITY OF THE FLOW FIELDS (PIV)

A short note on the validity of the flow fields obtained via PIV in chapter 3.

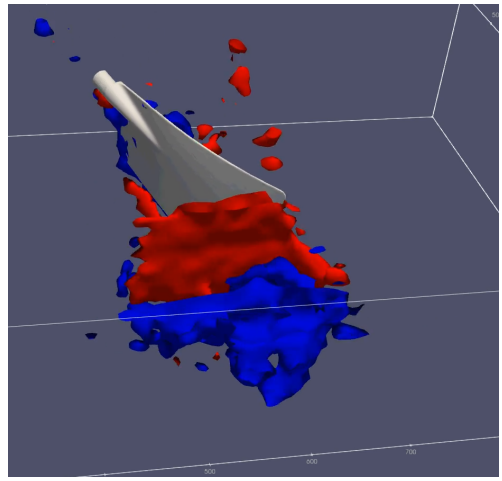

Figure B.1: The iso-surface vorticity ω_z based on a scan of the flow field towards the end of the drive phase, just before the release. The experiment was repeated three times per plane and then the plane was shifted along the vertical axis by approximately 10 mm. Red and blue iso-surfaces indicate positive and negative, respectively.

B.1. VALIDITY OF THE OBTAINED FLOW FIELDS (PIV)

The PIV measurements presented in this thesis are two-dimensional (2D) while the flow around the oar blade is three-dimensional (3D). To validate whether these two-dimensional PIV measurements are representative flow fields for understanding the hydrodynamics of rowing a (coarse) 'scan' of the flow field was created in order to create an impression of the three-dimensional flow field using PIV measurements. From the scan it is evident that the flow field varies mostly in the horizontal plane and behaves similar in different planes at varying depths. Figure B.1 shows the vorticity component ω_z iso-surfaces just before the release. The jet-like structure is clearly visible and it appears that two vertical vortex columns are generated (using the Q-criteria yields similar results).

Also the force generated by the flow acting on the oar blade can be directly derived from the PIV measurements performed in chapter 3 and can be matched with the forces measured by a force/torque transducer (which are caused by the three-dimensional flow). The vector spacing of the PIV measurements is large (6.1 mm) compared to the Kolmogorov length scale defined as

$$\eta_K = \left(\frac{\nu^3}{\varepsilon}\right)^{1/4}, \tag{B.1}$$

where the kinematic viscosity $\nu = 1.00\times10^{-6}$ m^{2}s^{-1}, and the average rate of dissipation of turbulence kinetic energy per unit mass is estimated by

$$\varepsilon \approx \frac{1}{2}\frac{V_{ref}^3}{L_{ref}}, \tag{B.2}$$

which results in $\eta_K \approx 27$ µm [1]. Although the PIV measurements do not fully resolve the smallest flow scale, they are representative for the (three-dimensional) flow around the

oar blade, since we can reproduce the force on the oar blade and power delivered by the oar blade on the water directly from the flow field.

Newton's third law states that to every action there is always opposed an equal reaction. Ergo, a force acts on the fluid $\vec{F}_f$ surrounding the oar blade that is equal in magnitude but opposite in direction to that of the oar blade force: $\vec{F} = -\vec{F}_f$. The fluid force equals a rate of change of momentum of the fluid (Newton's second law):

$$\vec{F}_f = \frac{d\vec{p}_f}{dt}. \tag{B.3}$$

The momentum of the fluid $\vec{p}_f$ at some moment in time t is estimated from the PIV measurements by integration of the velocity $\vec{V}_f$ over the field of view (FOV) multiplied by the density of water ρ and the blade height l_b. The blade height l_b is taken as characteristic length to transform the two-dimensional (2D) PIV measurement to a volume, essentially treating the flow as quasi-2D along the blade height. The derivative of the flow field momentum with respect to time is approximated from the flow field time series $\vec{V}_f(t)$ by a central difference. Combining the equations leads to the force on the blade as a function of the flow field velocity:

$$\vec{F}(t) = -\vec{F}_f(t) = -\frac{d\vec{p}_f(t)}{dt} \approx -\frac{\rho l_b}{2\Delta t}\int_{FOV}\left[\vec{V}_f(t+\Delta t) - \vec{V}_f(t-\Delta t)\right] dA, \tag{B.4}$$

where $\Delta t = 4$ ms. As is shown in figure B.2a, the forces are reproduced quantitatively very well during the first part of the drive phase. For the last part of the drive the forces are not matching quantitatively, but qualitatively do show the same behaviour as the forces measured directly. We also compare the rate of change of kinetic energy of the fluid, i.e. the power $P_f = \frac{dE_f}{dt}$, to that of the power put into the fluid motion by the oar blade P (equation 3.3). An analysis analogous to that of the force comparison yields

$$P(t) = P_f(t) = \frac{dE_f}{dt} \approx \frac{\rho l_b}{4\Delta t}\int_{FOV}\left[|\vec{V}_f|^2(t+\Delta t) - |\vec{V}_f|^2(t-\Delta t)\right] dA. \tag{B.5}$$

Here, it is assumed that the change in energy of the fluid over time Δt is fully due to the change in kinetic energy, which is a reasonable assumption because of the high Reynolds number ($Re = 1.64\times10^5$). In figure B.2b it is apparent that the power is reproduced, although it is underestimated throughout the drive phase. The discrepancy in the power comparison might be due to not fully resolving the flow, thus energy in the smaller scales is not taken into account. The same holds for the comparison of the forces. During the second part of the drive phase, $t^* > 0.6$, a very complex and highly turbulent wake is formed, as discussed in section 3.4.3, so the PIV measurement may not capture enough features to quantitatively match the measured forces. Also, we assume that the wake is quasi-2D over a (constant) blade height l_b. Although during the first part of the drive phase this assumption holds, during the second part, when the flow is more complex, the flow apparently deviates from its quasi-2D behaviour and becomes more three-dimensional. However, since we can qualitatively match both power and forces from the flow field to the directly measured signals, even quantitatively in the first part of the drive phase, we deem the selected measurement plane for the PIV measurements representative for the flow field around the oar blade.

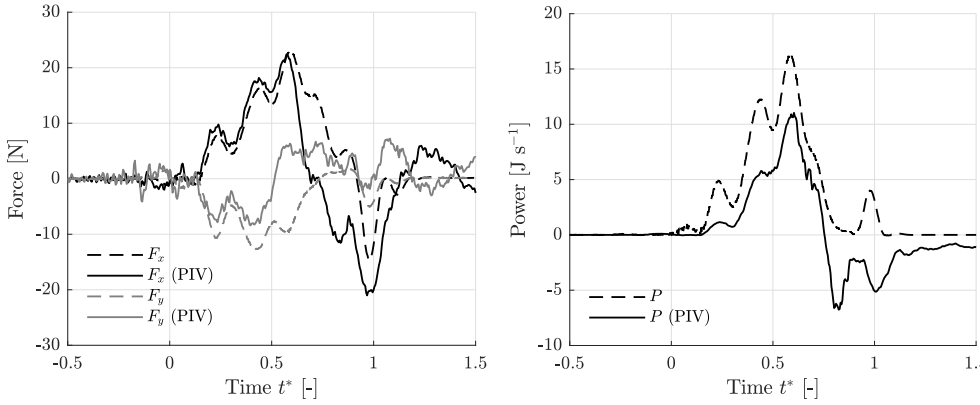

(a) (b)

Figure B.2: A comparison of directly measured quantities and quantities derived from the flow field obtained through PIV for $\kappa = 1.00$. (a) Comparison of force components F_x and F_y. (b) Comparison of power P. Note that 'negative' power in this case means that amount of kinetic energy in the fluid is reduced, primarily by the oar blade slowing down the fluid motion reducing kinetic energy, but also by e.g. fluid structures that move out of plane/ out of field of view, structures breaking up into smaller structures that are no longer captured by the PIV measurements, or by dissipation.

REFERENCES

[1] TENNEKES, H. & LUMLEY, J. L. 1972 *A First Course in Turbulence*. MIT Press.

ACKNOWLEDGEMENTS

Bijzonder veel dank aan mijn promotor Jerry Westerweel en copromotor Mark Tummers voor de ondersteuning, de hulp, soms het nodige zetje, en de gezelligheid. Bedankt voor jullie steun voor een industriële robot, ondanks dat later bleek dat er een muur uit het lab moest om het apparaat naar binnen te krijgen.

Dank aan Mathieu die altijd klaar stond om hulp te bieden bij weerbarstige simulaties en de wondere wereld van Linux, clusters, 'segmentation faults', en geregeld de reddende engel was in het geval van dataverlies.

Dank aan de technische staf; Edwin, Jan en Jasper, jullie zijn van onschatbare waarde voor iedere experimentalist. Bedankt voor de gezellige gesprekken aan de koffietafel en bedankt voor het vertalen van de theorie en het idee naar een werkbare realiteit.

Bedankt Lotte en Josje voor de projecten waaraan we hebben samengewerkt, zonder de dynamiek met de projectpartners, VU Amsterdam en TU Eindhoven was dit project nooit geworden tot wat het is.

Dank aan de Koninklijke Nederlandse Roeibond, in het bijzonder aan Hessel Evertse, voor hun bijdrage aan het project en voor hun interesse voor de resultaten.

Dank aan FlowMotion, in het bijzonder aan Ellert en Christian voor hun hulp in raad en daad.

Bijzonder veel dank aan mijn kamergenoten met wie ik veel tijd heb doorgebracht, met wie ik veel heb gelachen en bij wie ik altijd terecht kon. Arnoud, Pedro, Ankur en Wout: ontzettend veel dank voor de mooie tijd die we samen hadden en ik hoop het in de toekomst weer zo te mogen treffen qua collega's. Arnoud bedankt voor de vele momenten waarop je mij verder hebt geholpen; Wout bedankt voor het tentoonspreiden van je organisatorisch vermogen, en de enorme boom in het kleine kantoortje.

Andere collega's met wie ik goede en minder goede (maar wel vermakelijke) gesprekken heb gehad, aan wie ik goede herinneringen heb, en aan wie ik geregeld terugdenk: Andries, Maurice, Florian, Marieke, Jerke, Jasper, Gem, Sören, Amitosh, Tariq, Saad, Melika, John, Haoyu, Koen, Manu, Mike, Arati, Erik, Pepijn, Sita, Willian, Özge, Daniele, Greta, Henk, en anderen die ik ben vergeten in deze lijst te zetten, maar die er zeker op zouden moeten.

Dank aan de stafleden die altijd openstonden voor een gesprek of een discussie en altijd een hypothese konden formuleren als antwoord op een vraag. In het bijzonder dank

aan Caroline voor het zijn van een luisterend oor en alle hulp (inclusief tips voor bezoeken aan Delft).

Dank aan mijn familie voor de constante reminder: “Is het al af?” en voor een luisterend oor voor als het even tegenzat. Dank aan al mijn vrienden voor hun relativerend vermogen, afleiding en humor en bovenal dank aan Jellie die heeft mogen delen in alle hoogtepunten en heeft moeten delen in alle dieptepunten.

Alles hat ein Ende, nur die Wurst hat zwei[1] .

[1] ‘Alles hat ein Ende nur die Wurst hat zwei (Krause & Ruth)’ by Stephan Remmler (1986)

CURRICULUM VITÆ

Ernst Jan GRIFT

14-04-1989 Born in Amersfoort, The Netherlands.

EDUCATION

2001–2007 Middelbare school
Christelijk College Groevenbeek, Ermelo, The Netherlands

2007–2011 Bachelor of Science in Mechanical Engineering
University of Twente, Enschede, The Netherlands

2011–2014 Master of Science in Engineering Fluid Dynamics
University of Twente, Enschede, The Netherlands

2014–2019 PhD. Fluid Mechanics
Delft University of Technology, Delft, The Netherlands

Thesis: The Hydrodynamics of Rowing Propulsion
Promotor: Prof. dr. ir. J. Westerweel
Copromotor: Dr. ir. M.J. Tummers

EXPERIENCE

2019–... Strategy Consultant
Monitor Deloitte, Amsterdam, The Netherlands

LIST OF PUBLICATIONS

- **E. J. Grift**, M.J. Tummers, J. Westerweel, *Hydrodynamics of rowing propulsion*, Journal of Fluid Mechanics (under review, April 2020).
- **E. J. Grift**, N. B. Vijayaragavan, M. J. Tummers, J. Westerweel, *Drag force on an accelerating submerged plate*, Journal of Fluid Mechanics **866**, 369-398 (2019).
- **E. J. Grift**, M. J. Tummers, E. F. J. Overmars, J. Westerweel, *PIV applied to a moving rowing blade*, Proceedings of the 13th International Symposium on Particle Image Velocimetry (2019).
- **E. J. Grift**, N. B. Vijayaragavan, M. J. Tummers, J. Westerweel, *Optimal Drag in an Accelerating Rowing Blade*, Bulletin of the American Physical Society **63** (2018).
- L.L. Lintmeijer, J. P. T. Onneweer, M. J. Hofmijster, W. A. Wijgergangs, H. De Koning, B. Clairbois, J. Westerweel, **E. J. Grift**, M. J. Tummers, A. J. Van Soest, *Towards determination of power loss at a rowing blade: Validation of a new method to estimate blade force characteristics*, PloS one **14** (5) (2019).
- J. van Houwelingen, R. M. Antwerpen, A. P. C. Holten, **E. J. Grift**, J. Westerweel, H. J. H. Clercx, *Automated LED tracking to measure instantaneous velocities in swimming*, Sports Engineering **21** (4), 419-427 (2018).
- J. van Houwelingen, D. H. J. Willemsen, R. P. J. Kunnen, G. J. F. van Heijst, **E. J. Grift**, W. P. Breugem, R. Delfos, J. Westerweel, H. J. H. Clercx, W. van de Water, *The effect of finger spreading on drag of the hand in human swimming*, Journal of biomechanics **63**, 67-73 (2017).
- W. van de Water, J. van Houwelingen, D. H. J. Willemsen, W. P. van Breugem, J. Westerweel, R. Delfos, **E. J. Grift**, *More efficient swimming by spreading your fingers*, Bulletin of the American Physical Society **61** (2016).